

AD-A183 013

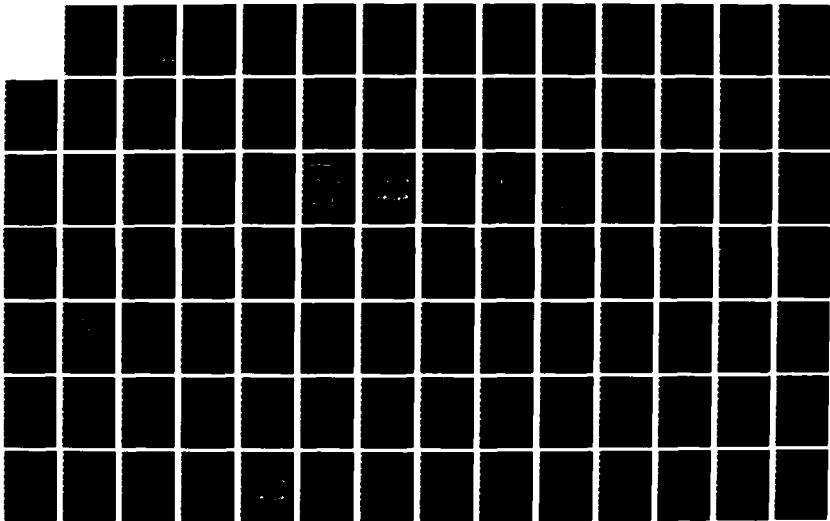
THE EFFECTS OF NEAR-SOURCE TOPOGRAPHY ON EXPLOSION  
WAVEFORMS: TELESEISMIC (U) TELEDYNE GEOTECH ALEXANDRIA  
VA ALEXANDRIA LABS K L MCLAUGHLIN ET AL JUL 86

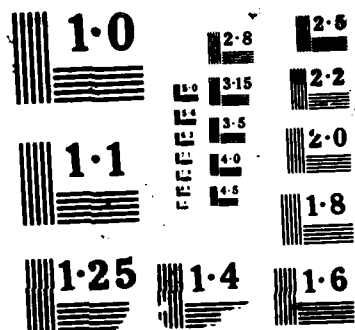
1/2

UNCLASSIFIED

TGAL-86-3 AFGL-TR-86-0159 F19228-85-C-0035 F/G 17/10

NL





AFGL-TR-86-0159

**AD-A183 013**

12  
DTIC FILE COPY

**THE EFFECTS OF NEAR-SOURCE TOPOGRAPHY ON EXPLOSION WAVEFORMS:  
TELESEISMIC OBSERVATIONS AND LINEAR FINITE DIFFERENCE CALCULATIONS**

Keith L. McLaughlin  
Rong-Song Jih  
Zoltan A. Der  
Alison C. Lees

Teledyne Geotech Alexandria Laboratories  
314 Montgomery Street  
Alexandria, VA 22314-1581

July 1986

Scientific Report No. 1

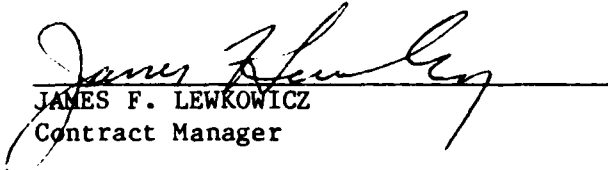
APPROVED FOR PUBLIC RELEASE; DISTRIBUTION UNLIMITED

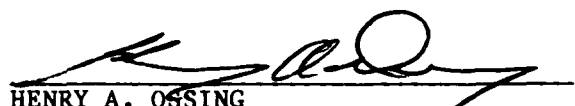
AIR FORCE GEOPHYSICS LABORATORY  
AIR FORCE SYSTEMS COMMAND  
UNITED STATES AIR FORCE  
HANSCOM AIR FORCE BASE, MASSACHUSETTS 01731

12  
S E D  
AUG 07 1987

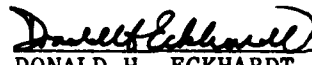
CONTRACTOR REPORTS

This technical report has been reviewed and is approved for publication.

  
JAMES F. LEWKOWICZ  
Contract Manager

  
HENRY A. OSSING  
Chief, Solid Earth Geophysics Branch

FOR THE COMMANDER

  
DONALD H. ECKHARDT  
Director  
Earth Sciences Division

This report has been reviewed by the ESD Public Affairs Office (PA) and is releasable to the National Technical Information Service (NTIS).

Qualified requesters may obtain additional copies from the Defense Technical Information Center. All others should apply to the National Technical Information Service.

If your address has changed, or if you wish to be removed from the mailing list, or if the addressee is no longer employed by your organization, please notify AFGL/DAA, Hanscom AFB, MA 01731. This will assist us in maintaining a current mailing list.

UNCLASSIFIED

SECURITY CLASSIFICATION OF THIS PAGE

REPORT DOCUMENTATION PAGE				Form Approved OMB No 0704 0188 Exp Date Jun 30, 1986	
1a REPORT SECURITY CLASSIFICATION Unclassified			1b RESTRICTIVE MARKINGS <b>A183013</b>		
2a SECURITY CLASSIFICATION AUTHORITY			3 DISTRIBUTION/AVAILABILITY OF REPORT Approved for public release; Distribution unlimited.		
2b DECLASSIFICATION/DOWNGRADING SCHEDULE					
4 PERFORMING ORGANIZATION REPORT NUMBER(S) TGAL-86-3			5 MONITORING ORGANIZATION REPORT NUMBER(S) AFGL-TR-86-0159		
6a NAME OF PERFORMING ORGANIZATION Teledyne Geotech		6b OFFICE SYMBOL (if applicable) TGAL		7a NAME OF MONITORING ORGANIZATION Air Force Geophysics Laboratory	
6c ADDRESS (City, State, and ZIP Code) 314 Montgomery Street Alexandria, Virginia 22314			7b ADDRESS (City, State, and ZIP Code) Hanscom AFB MA 01731-5000		
8a NAME OF FUNDING/SPONSORING ORGANIZATION Air Force Geophysics Laboratory		8b OFFICE SYMBOL (if applicable) DSO/GSD		9 PROCUREMENT INSTRUMENT IDENTIFICATION NUMBER F19628-85-C-0035	
8c ADDRESS (City, State, and ZIP Code) Hanscom AFB MA 01731-5000			10 SOURCE OF FUNDING NUMBERS		
			PROGRAM ELEMENT NO 62714E	PROJECT NO 5A10	TASK NO DA
			WORK UNIT ACCESSION NO AX		
11 TITLE (Include Security Classification) The Effects of Near-Source Topography on Explosion Waveforms: Teleseismic Observations and Linear Finite Difference Calculations					
12 PERSONAL AUTHOR(S) K.L. McLaughlin, R-S. Jih, Z.A. Der, and A.C. Lees					
13a TYPE OF REPORT Scientific Report #1		13b TIME COVERED FROM Feb 85 TO Feb 87		14 DATE OF REPORT (Year, Month, Day) July 1986	
15 PAGE COUNT 102					
16 SUPPLEMENTARY NOTATION					
17 COSATI CODES			18 SUBJECT TERMS (Continue on reverse if necessary and identify by block number)		
FIELD	GROUP	SUB-GROUP			
			Scatter P-Wave Ahaggar		
			Topography Deconvolution Linear finite difference		
19 ABSTRACT (Continue on reverse if necessary and identify by block number)					
<p style="text-align: center;"><b>SECTION I</b></p> <p style="text-align: center;"><b>BOUNDARY CONDITIONS FOR ARBITRARY POLYGONAL TOPOGRAPHY IN A 2-D ELASTIC FINITE-DIFFERENCE SCHEME FOR SEISMOGRAM GENERATION</b></p> <p>A simple method to implement the free-surface topography of polygonal shape in 2-D second-order finite-difference simulations of the elastic wave equation is presented that includes an empirically stable treatment of various slopes and transition points between the sloping segments. On the inclined free-surface, the vanishing stress conditions are implemented to a rotated coordinate system parallel to the inclined boundary as previous works did. While for each transition point on the topography where the slope changes, we propose to use the first-order approximation of boundary conditions in a locally rotated</p>					
20 DISTRIBUTION/AVAILABILITY OF ABSTRACT <input type="checkbox"/> UNCLASSIFIED/UNLIMITED <input type="checkbox"/> SAME AS RPT <input type="checkbox"/> DTIC USERS			21 ABSTRACT SECURITY CLASSIFICATION Unclassified		
22a NAME OF RESPONSIBLE INDIVIDUAL James F. Lewkowicz			22b TELEPHONE (Include Area Code) (617) 377-3028		22c OFFICE SYMBOL LWH

(19. Continued)

coordinate system in which the normal axis always coincides with the bisector of the corner. These extrapolation formulae are consistent with boundary conditions to first-order accuracy in spatial increment, same as the classical one-sided explicit approximation scheme widely used for flat free-surface case. Testing results indicate that the present scheme works stably for fairly complicated geometric shapes consisting of ridges and valleys with steep and gentle slopes over a range of Poisson ratios of practical interest thus enabling us to study more realistic problems for which the topography plays a significant role in shaping the wavefield and analytical solution might not be available.

## SECTION 2

### TELESEISMIC SPECTRAL AND TEMPORAL $M_0$ AND $\Psi_{\omega}$ ESTIMATION FOR FOUR FRENCH EXPLOSIONS IN SOUTHERN SAHARA

Estimates for explosion moment,  $M_0$ , and reduced displacement potential,  $\Psi_{\omega}$ , are made for four French explosions at Taourirt Tan Afella Massif in southern French Sahara using data from the LRSM network and the arrays EKA and YKA. Preparatory to determining moments,  $\tau^*$  estimates are made for each station and the source region  $\tau^*$  values of 0.30 to 0.35 seconds are found for the southern Sahara test site. This source region attenuation level is consistent with the "hot spot" hypothesis for the Ahaggar plateau in northern Africa. Consequently, the attenuation bias between Ahaggar and the Nevada Test Site should be small.

Both spectral estimation and broadband temporal deconvolution methods are used for estimation of the explosion moments. The deconvolution estimates of static moment are found to be consistent with the spectral estimation methods. Deconvolved seismograms for the explosions EMERAUDE, RUBIS, SAPHIR, and GRENAT show evidence of strong anisotropic free surface interaction that may be due to scattering from the steep topography of the Taourirt Tan Affela Massif test site.

## SECTION 3

### SCATTERING FROM NEAR-SOURCE TOPOGRAPHY: TELESEISMIC OBSERVATION AND NUMERICAL 2-D EXPLOSIVE LINE SOURCE SIMULATIONS

2-D linear elastic finite difference simulations of teleseismic P waveforms from line sources have been used to explore the variations that may be induced in event magnitude-yield determination by the emplacement of explosive sources under mountainous topographic features. The southern Sahara French test site in Algeria, at Taourirt Tan Afella Massif on the Ahaggar plateau has been used as a case study. The topography of this test site is extreme and the event locations permit a test of the hypothesis that topography influences short-period event magnitudes of contained nuclear explosions. The maximum variation that is expected is plus or minus 0.15 magnitude units from the network mean. The magnitude variations are expected to change rapidly with takeoff angle and azimuth.

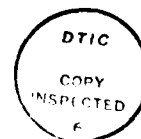
Teleseismic observations of the explosions at the southern Sahara test site are compared to predictions made from 2-D simulations. Waveform data from the arrays EKA, and YKA as well as LRSM data have been deconvolved to broadband displacement for inspection of the apparent far-field P-wave source. Qualitative comparisons are favorable that the topography above the explosions RUBIS and SAPHIR defocused teleseismic pP at certain takeoff angles and azimuths. Long-period positive-polarity pulses can be seen at several sites that may indicate Rayleigh-to-P scattering from topography near the source.

WWSSN maximum likelihood magnitude data for the "a", "ab", and "max" P phases have been used to estimate that the magnitude variation due to topographic scattering is no more than 0.15 rms magnitude units across the WWSSN.

## TABLE OF CONTENTS

	Page
1. BOUNDARY CONDITIONS FOR ARBITRARY POLYGONAL TOPOGRAPHY IN A 2-D ELASTIC FINITE-DIFFERENCE SCHEME FOR SEISMOGRAM GENERATION	1
2. TELESEISMIC SPECTRAL AND TEMPORAL $M_0$ AND $\Psi_0$ ESTIMATES FOR FOUR FRENCH EXPLOSIONS IN SOUTHERN SAHARA	33
3. SCATTERING FROM NEAR-SOURCE TOPOGRAPHY: TELESEISMIC OBSERVATIONS AND NUMERICAL 2-D EXPLOSIVE LINE SOURCE SIMULATIONS	61
DISTRIBUTION LIST	91

Accession For	
NTIS GRA&I	<input checked="" type="checkbox"/>
DTIC TAB	<input type="checkbox"/>
Unannounced	<input type="checkbox"/>
Justification	
By	
Distribution/	
Availability Codes	
Dist	Avail and/or Special
A-1	



(THIS PAGE INTENTIONALLY LEFT BLANK)



## SECTION 1

### BOUNDARY CONDITIONS FOR ARBITRARY POLYGONAL TOPOGRAPHY IN A 2-D ELASTIC FINITE-DIFFERENCE SCHEME FOR SEISMOGRAM GENERATION

R.-S. Jih, K. L. McLaughlin, Z. A. Der  
Teledyne Geotech Alexandria Laboratories  
314 Montgomery Street  
Alexandria, VA 22314

## INTRODUCTION

The 2-D linear finite-difference (LFD) method has become a popular means to generate synthetic seismograms because of the ease with which they can be applied to model the low-frequency response of complex structures for which analytical solutions can not be derived. So far most applications were limited to simple geometric shapes, however. For instance, a lot of earlier work only deal with restrictive models in which the boundaries are either parallel to the coordinates or only allowing 45 deg ramp (Alterman and Karal, 1968; Alterman and Loewenthal, 1970; Munasinghe and Farnell, 1973; Ilan et al., 1975, 1979; Fuyuki and Nakano, 1984; Hong and Bond, 1986; etc). Boore et al. (1981) simulated vertically incident body waves impinging on a 45 deg ramp by using the same formulation as in Ilan et al. (1975). Ilan (1977) utilized the LFD method to simulate the P-SV wave propagation in an elastic medium with polygonal free-surface, but the treatment of the transition points between the segments of various slopes in the polygons was not addressed. His approach also requires the use of a non-uniform grid and thus introduces some inevitable complexity in implementing the iteration procedure. We have found that the treatment of the points between the segments of the polygon is not a trivial problem, and that a simple extrapolation of the boundary conditions

from either side of the transition point as suggested in some previous works may either lead to numerical instability or yield solutions violating Huygen's principle and Snell's law.

In the present work, we propose an improved representation of boundary conditions for miscellaneous types of corner points on the topography while maintaining the simplicity of fixed mesh widths. For each point on the topography where slope changes, we use a local grid system in which the normal axis always coincides with the bisector of the corner. These extrapolation formulae are consistent with boundary conditions to first-order accuracy in spatial increment, same as the classical one-sided explicit approximation scheme for flat free-surface that has been widely used for a long time. Testing results indicate that the present scheme works stably for fairly complicated geometric shapes consisting of ridges and valleys with steep and gentle slopes over a range of Poisson ratios of practical interest.

## MODEL

Consider a half-space with an arbitrary polygonal free-surface. Define a Cartesian coordinate system with X horizontal and Z vertical, positive downward (Figure 1). Assume that the material is perfectly elastic, isotropic, and homogeneous with compressional, shear velocities  $\alpha$ ,  $\beta$  respectively. Let U, W be the horizontal and the vertical components of displacements. Then the wave propagation is governed by the following equation

$$\frac{\partial^2 U(x,z,t)}{\partial t^2} = \alpha^2 \frac{\partial^2 U(x,z,t)}{\partial x^2} + (\alpha^2 - \beta^2) \frac{\partial^2 W(x,z,t)}{\partial x \partial z} + \beta^2 \frac{\partial^2 U(x,z,t)}{\partial z^2} \quad (1a)$$

$$\frac{\partial^2 W(x,z,t)}{\partial t^2} = \alpha^2 \frac{\partial^2 W(x,z,t)}{\partial x^2} + (\alpha^2 - \beta^2) \frac{\partial^2 U(x,z,t)}{\partial x \partial z} + \beta^2 \frac{\partial^2 W(x,z,t)}{\partial z^2} \quad (1b)$$

A grid is imposed on this X-Z plane with fixed mesh size  $\Delta x$  and  $\Delta z$ . We let  $x = i\Delta x$ ,  $z = k\Delta z$  and  $t = l\Delta t$  where  $\Delta t$  is the increment step in time,  $i, k, l$  are positive integers, and denote by  $U_{i,k,l}$  and  $W_{i,k,l}$  the approximate components of displacement at grid point

( $i\Delta x, k\Delta z$ ) at time  $l\Delta t$ . By replacing the derivatives in equation (1) by central finite differences, we obtain the following explicit formulae:

$$\begin{aligned}
 U_{i,k,l+1} = & -U_{i,k,l-1} + 2U_{i,k,l} + \alpha^2 \left( \frac{\Delta t}{\Delta x} \right)^2 (U_{i+1,k,l} - 2U_{i,k,l} + U_{i-1,k,l}) \\
 & + \beta^2 \left( \frac{\Delta t}{\Delta z} \right)^2 (U_{i,k+1,l} - 2U_{i,k,l} + U_{i,k-1,l}) \\
 & + \frac{1}{4} \frac{\Delta t^2}{\Delta x \Delta z} (\alpha^2 - \beta^2) \cdot (W_{i+1,k+1,l} - W_{i+1,k-1,l} - W_{i-1,k+1,l} + W_{i-1,k-1,l}) \quad (1c) \\
 W_{i,k,l+1} = & -W_{i,k,l-1} + 2W_{i,k,l} + \beta^2 \left( \frac{\Delta t}{\Delta x} \right)^2 (W_{i+1,k,l} - 2W_{i,k,l} + W_{i-1,k,l}) \\
 & + \alpha^2 \left( \frac{\Delta t}{\Delta z} \right)^2 (W_{i,k+1,l} - 2W_{i,k,l} + W_{i,k-1,l}) \\
 & + \frac{1}{4} \frac{\Delta t^2}{\Delta x \Delta z} (\alpha^2 - \beta^2) \cdot (U_{i+1,k+1,l} - U_{i+1,k-1,l} - U_{i-1,k+1,l} + U_{i-1,k-1,l}) \quad (1d)
 \end{aligned}$$

The reader is referred to Boore (1972), Alterman et al. (1972), and Kelly et al. (1976) for a more detailed discussion of the approximation of partial derivatives by finite differences. Recently a number of techniques have been pursued in an effort to improve the computational performance of LFD solutions to wave equations. These include variable grids, higher order schemes or implicit rather than explicit methods. None of these can provide significant improvement over the traditional explicit second order centered LFD schemes described by Alterman, Boore and Kelly when complicated topographic profiles are used as free-surface. To implement arbitrary topography in the LFD scheme, it suffices to approximate the topography by polygons. Six algorithms are presented here to implement the free-surface boundary condition for the six separate cases shown in Figure 1 labeled (A) through (F). Only the formulae for increasing elevation with increasing  $x$  are given for brevity. Since the calculation of corner points always requires displacements of points nearby, it is necessary to follow a specific order in each iteration step once the displacements at flat free-surface are extrapolated. This specific order is suggested in Figure 1 and self-explanatory from the description of various algorithms

in the following sections. Also the topography must be sampled so that each segment of the polygon consists of at least 3 points (i.e. 2 sub-segments).

## ALGORITHMS

### (A) CONSTANT STEEP SLOPE

Suppose that a grid point  $\langle i, k \rangle$  lies on an inclined free-surface with slope  $m\Delta z/\Delta x$ ,  $m \geq 2$ . The boundary condition states that both the tangential and normal stress components vanish at grid point  $\langle i, k \rangle$ , i.e. if we rotate the  $X-Z$  coordinate system by angle  $\theta \equiv \tan^{-1}(m \Delta z/\Delta x)$  counterclockwise to the  $X'-Z'$  system, then

$$\frac{\partial U'}{\partial z'} + \frac{\partial W'}{\partial x'} = 0 \quad (2a)$$

$$\frac{\partial W'}{\partial z'} + (1 - 2\frac{\beta^2}{\alpha^2}) \frac{\partial U'}{\partial x'} = 0 \quad (2b)$$

where  $U'$ ,  $W'$  are the displacement in  $X'$ ,  $Z'$  direction respectively

Thus equation (2) can be used to derive the following explicit extrapolation formulae :

$$U'_{i,k} = U'_0 - \cos\theta \sin\theta (W'_{i+1,k-1} - W'_{i,k+m-1}) \quad (3a)$$

$$W'_{i,k} = W'_0 - \cos\theta \sin\theta (1 - 2\frac{\beta^2}{\alpha^2}) (U'_{i+1,k-1} - U'_{i,k+m-1}) \quad (3b)$$

where  $U_0 = \cos^2\theta U_{i,k+m} + \sin^2\theta U_{i+1,k}$ ,  $W_0 = \cos^2\theta W_{i,k+m} + \sin^2\theta W_{i+1,k}$  are the linearly interpolated displacements at the point labeled "0" (Figure 2). Rotate the displacement at points "0",  $\langle i+1, k-1 \rangle$ , and  $\langle i, k+m-1 \rangle$  to the inclined system to obtain  $U'_{i,k}$ ,  $W'_{i,k}$  by using formulae (3). The displacements at  $\langle i, k \rangle$  are then rotated back to the original system by angle  $-\theta$ .

**(B) CONSTANT GENTLE SLOPE**

For grid point  $\langle i, k \rangle$  on an inclined free-surface with slope  $\Delta z / \Delta x$  (Figure 3), let

$$U_0 = \epsilon_0 U_{i+1,k} + (1 - \epsilon_0) U_{i,k+1} \quad (4a)$$

$$W_0 = \epsilon_0 W_{i+1,k} + (1 - \epsilon_0) W_{i,k+1} \quad (4b)$$

where

$$\epsilon_0 = \sin^2 \theta,$$

$$\theta = \tan^{-1}(\Delta z / \Delta x),$$

Compute

$$U'_{i,k} = U'_0 - \sin \theta \cos \theta (W'_{i+1,k} - W'_{i,k+1}) \quad (5a)$$

$$W'_{i,k} = W'_0 - \sin \theta \cos \theta (1 - 2 \frac{\beta^2}{\alpha^2}) (U'_{i+1,k} - U'_{i,k+1}) \quad (5b)$$

Then rotate  $U'_{i,k}$ ,  $W'_{i,k}$  back to the original system. Note that this algorithm is simpler than Ilan's (1977) DuFort-Frankel type approximation (see Appendix) and the weighting factor  $\sin \theta \cos \theta$  in formulae (5) is applicable whether  $\theta \leq 45^\circ$  or not. Also note that the words 'gentle' and 'steep' have only relative meaning here since we can always adjust  $\Delta x$  and  $\Delta z$  before implementation.

**(C) CONCAVE HORIZONTAL-TO-GENTLE SLOPE TRANSITION**

For grid points at the bottom of a canyon with slope  $m \Delta z / \Delta x$ ,  $m \geq 1$  (Figure 4), assuming that  $\Delta x \geq \Delta z$ , let  $\theta = \tan^{-1}(m \Delta z / \Delta x)$ ,  $\epsilon_0 = \tan(\theta/2) \Delta z / \Delta x$ ,  $\epsilon_1 = \tan(\theta/2) \cot \theta$ , and

$$U_0 = (1 - \epsilon_0) U_{i,k+1} + \epsilon_0 U_{i+1,k+1} \quad (6a)$$

$$W_0 = (1 - \epsilon_0) W_{i,k+1} + \epsilon_0 W_{i+1,k+1} \quad (6b)$$

$$U_1 = (1 - \epsilon_1) U_{i-1,k+m+1} + \epsilon_1 U_{i-1,k+1} \quad (6c)$$

$$W_1 = (1 - \epsilon_1) W_{i-1,k+m+1} + \epsilon_1 W_{i-1,k+1} \quad (6d)$$

$$U_2 = (1-\epsilon_1)U_{i+1,k-m+1} + \epsilon_1 U_{i+1,k+1} \quad (6e)$$

$$W_2 = (1-\epsilon_1)W_{i+1,k-m+1} + \epsilon_1 W_{i+1,k+1} \quad (6f)$$

Then,

$$U'_{i,k} = U'_0 - \frac{\Delta z}{2\Delta x}(W'_2 - W'_1) \quad (7a)$$

$$W'_{i,k} = W'_0 - \frac{\Delta z}{2\Delta x}(1 - 2\frac{\beta^2}{\alpha^2})(U'_2 - U'_1) \quad (7b)$$

Note that we rotate  $U, W$  by angle  $\theta/2$  to get  $U', W'$  (instead of  $\theta$ ) so that  $Z'$  axis is consistent with the direction of the local bisector at grid point  $\langle i, k \rangle$ .

For the case  $\Delta x < \Delta z$ , substitute  $\epsilon_0 = \cot(\theta/2)\Delta x/\Delta z$ , and  $\epsilon_1 = \tan\theta \tan(\theta/2)$  in formulae (6), and replace  $\Delta z/2\Delta x$  in (7) by  $\cot(\theta/2)/2$ .

#### (D) CONCAVE GENTLE-TO-STEEP SLOPE TRANSITION

For grid points with left slope  $n\Delta z/\Delta x$  and right slope  $m\Delta z/\Delta x$ ,  $m > n$  (Figure 5), assuming that  $\Delta x \leq n\Delta z$ , let  $\theta = \tan^{-1}(n\Delta z/\Delta x)$ ,  $\phi = \tan^{-1}(m\Delta z/\Delta x)$ ,  $\eta = (\theta + \phi)/2$ ,  $\epsilon_0 = \epsilon_1 = \tan\theta \cot\eta$ ,  $\epsilon_2 = \tan\eta \cot\phi$ , and

$$U_0 = (1-\epsilon_0)U_{i+1,k} + \epsilon_0 U_{i+1,k+n} \quad (8a)$$

$$W_0 = (1-\epsilon_0)W_{i+1,k} + \epsilon_0 W_{i+1,k+n} \quad (8b)$$

$$U_1 = (1-\epsilon_1)U_{i,k+n} + \epsilon_1 U_{i-1,k+n} \quad (8c)$$

$$W_1 = (1-\epsilon_1)W_{i-1,k+n} + \epsilon_1 W_{i-1,k+n} \quad (8d)$$

$$U_2 = (1-\epsilon_1)U_{i+1,k} + \epsilon_1 U_{i+1,k-m} \quad (8e)$$

$$W_2 = (1-\epsilon_1)W_{i+1,k} + \epsilon_1 W_{i+1,k-m} \quad (8f)$$

Then,

$$U'_{i,k} = U'_0 - \frac{1}{\tan\eta + \tan\theta}(W'_2 - W'_1) \quad (9a)$$

$$W'_{i,k} = W'_0 - \frac{1}{\tan\eta + \tan\theta} \left(1 - 2\frac{\beta^2}{\alpha^2}\right)(U'_2 - U'_1) \quad (9b)$$

Note that we rotate  $U, W$  by angle  $\eta$  to get  $U', W'$  so that the  $Z'$  axis is consistent with the direction of the local bisector at grid point  $\langle i, k \rangle$ .

For the case that  $\Delta x > n\Delta z$ , substitute  $\epsilon_0 = \tan\theta\tan\eta$ ,  $\epsilon_1 = \tan\theta\cot\eta$ , and  $\epsilon_2 = \tan\eta\cot\theta$ , in formulae (8), and replace  $\tan\eta + \tan\theta$  in (9) by  $\cot\eta + \cot\theta$ .

### (E) CONVEX CHANGE IN SLOPE

For grid points with change in slope from  $m\Delta z/\Delta x$  to  $n\Delta z/\Delta x$ ,  $m > n$ , let  $\theta = \tan^{-1}(n\Delta z/\Delta x)$ ,  $\phi = \tan^{-1}(m\Delta z/\Delta x)$ ,  $\eta = (\theta + \phi)/2$ ,  $\epsilon_0 = \tan\eta\Delta z/\Delta x$ . If  $\epsilon_0$  is less than 1, then let

$$U_0 = (1 - \epsilon_0)U_{i,k+1} + \epsilon_0 U_{i+1,k+1} \quad (10a)$$

$$W_0 = (1 - \epsilon_0)W_{i,k+1} + \epsilon_0 W_{i+1,k+1}, \quad (10b)$$

otherwise let  $\epsilon_3 \equiv 1/\epsilon_0$ , and

$$U_0 = (1 - \epsilon_3)U_{i+1,k+1} + \epsilon_3 U_{i+1,k} \quad (10c)$$

$$W_0 = (1 - \epsilon_3)W_{i+1,k+1} + \epsilon_3 W_{i+1,k} \quad (10d)$$

Now depending on the value of  $m$ , we have 2 cases :

(E.1)  $m = 1$  (Figure 6A), note that  $\tan\phi < \tan\eta < \tan\theta$ , hence

$\epsilon_1 \equiv (\tan\eta\cot\phi - 1)/(n-1)$  is always between 0 and 1. Let

$$U_1 = (1 - \epsilon_1)U_{i,k+1} + \epsilon_1 U_{i,k+n} \quad (11a)$$

$$W_1 = (1 - \epsilon_1)W_{i,k+1} + \epsilon_1 W_{i,k+n} \quad (11b)$$

Then,

$$U'_{i,k} = U'_0 - \epsilon_2(W'_{i+1,k} - W'_1) \quad (12a)$$

$$W'_{i,k} = W'_0 - \epsilon_2(1 - 2\frac{\beta^2}{\alpha^2})(U'_{i+1,k} - U'_1) \quad (12b)$$

where  $\epsilon_2 = \tan\phi$  if  $\epsilon_0 \leq 1$ , or  $\cot\eta$  if  $\epsilon_0 > 1$ .

(E.2) For the case  $m > 1$  (Figure 6B), let  $\epsilon_1 \equiv (2\Delta z \cot\eta / \Delta x)$ , then  $\epsilon_1$  is always between 0 and 1.

$$U_1 = (1 - \epsilon_1)U_{i,k-1} + \epsilon_1 U_{i+1,k-1} \quad (11c)$$

$$W_1 = (1 - \epsilon_1)W_{i,k-1} + \epsilon_1 W_{i+1,k-1} \quad (11d)$$

The displacements at point  $\langle i, k-1 \rangle$  are computed by extrapolation (see algorithm (G)) since it's outside the grid. Now,

$$U'_{i,k} = U'_0 - \epsilon_2(W'_{i+1,k} - W'_{i,k+1}) \quad (12c)$$

$$W'_{i,k} = W'_0 - \epsilon_2(1 - 2\frac{\beta^2}{\alpha^2})(U'_{i+1,k} - U'_{i,k+1}) \quad (12d)$$

where  $\epsilon_2 = 0.5 \tan\eta$  if  $\epsilon_0 \leq 1$ , or  $\Delta x / (2\Delta z)$  if  $\epsilon_0 > 1$ .

Note that again we rotate  $U, W$  by angle  $\eta$  to get  $U', W'$  so that the  $Z'$  axis is consistent with the direction of the local bisector at grid point  $\langle i, k \rangle$ .

## (F) CONVEX GENTLE SLOPE-TO-HORIZONTAL TRANSITION

Without loss of generality, we may assume that the topography changes slope from  $\Delta z / \Delta x$  to 0 at the crests (Figure 7). Let  $\phi = \tan^{-1}(\Delta z / \Delta x)$ ,  $\epsilon_0 = \tan(\phi/2)\tan\phi$ , and  $\epsilon_1 = \tan(\phi/2)\cot\phi$ . Note that  $\epsilon_0 \leq 1$  provided  $\Delta y \leq \sqrt{3} \Delta x$ , i.e.  $\phi \leq 60^\circ$ . Let

$$U_0 = (1 - \epsilon_0)U_{i,k+1} + \epsilon_0 U_{i+1,k+1} \quad (13a)$$

$$W_0 = (1 - \epsilon_0)W_{i,k+1} + \epsilon_0 W_{i+1,k+1} \quad (13b)$$

$$U_1 = (1 - \epsilon_1)U_{i-1,k+1} + \epsilon_1 U_{i-1,k+2} \quad (13c)$$

$$W_1 = (1 - \epsilon_1)W_{i-1,k+1} + \epsilon_1 W_{i-1,k+2} \quad (13d)$$



$$U_2 = (1-\epsilon_1)U_{i+1,k+1} + \epsilon_1 U_{i+1,k} \quad (13e)$$

$$W_2 = (1-\epsilon_1)W_{i+1,k+1} + \epsilon_1 W_{i+1,k} \quad (13f)$$

Then,

$$U'_{i,k} = U'_0 - \frac{\tan\phi}{2}(W'_2 - W'_1) \quad (14a)$$

$$W'_{i,k} = W'_0 - \frac{\tan\phi}{2}(1 - 2\frac{\beta^2}{\alpha^2})(U'_2 - U'_1) \quad (14b)$$

Here we rotate  $U, W$  by angle  $\phi/2$  to get  $U', W'$  so that the  $Z'$  axis is again consistent with the direction of the local bisector at grid point  $\langle i, k \rangle$ .

### (G) FICTITIOUS BOUNDARY POINTS FOR STEEP SLOPE

Suppose that a grid point  $\langle i, k \rangle$  lies on the free-surface with slope  $m\Delta z/\Delta x$ ,  $m \geq 1$ . Due to the explicit scheme (equation (1c) and (1d)) we adopt for the interior points, the calculation of the displacements at inner points  $\langle i+1, k \rangle, \langle i+1, k-1 \rangle, \dots, \langle i+1, k-m+1 \rangle$  require displacement values at  $\langle i, k-1 \rangle, \langle i, k-2 \rangle, \dots, \langle i, k-m \rangle$  which are outside the topography. This difficulty can be easily removed by evaluating  $m$  fictitious layers above the topography as follows (Figure 8):

For  $1 \leq n \leq m$ , let  $\epsilon_0 = (n/m)\sin^2\theta$ , where  $\theta = \tan^{-1}m\Delta z/\Delta x$ , use  $U_0 = \epsilon_0 U_{i+1,k-m} + (1-\epsilon_0)U_{i,k}$  and  $W_0 = \epsilon_0 W_{i+1,k-m} + (1-\epsilon_0)W_{i,k}$  as the approximate displacement of the orthogonal projection of point  $\langle i, k-m+n \rangle$  on the free-surface.

Now rotate displacements at points  $\langle i+1, k-m \rangle, \langle i, k \rangle$  and "0" by angle  $\theta$  as before to extrapolate the approximate motion at point  $\langle i, k-m+n \rangle$ :

$$U'_{i,k-m+n} = U'_0 - \frac{n}{m}\sin\theta\cos\theta(W'_{i+1,k-m} - W'_{i,k})$$

$$W'_{i,k-m+n} = W'_0 - (1-2\frac{\beta^2}{\alpha^2})\frac{n}{m}\sin\theta\cos\theta(U'_{i+1,k-m} - U'_{i,k})$$

Then rotate  $U'$ ,  $W'$  back to the original system.

## EXAMPLES

### EXAMPLE 1

Figure 9 shows the propagation of a normally incident P wave through a model with a  $45^\circ$  ramp on the top of grid. Shading is proportional to displacement amplitude. The initial wave was a tapered displacement pulse of the form  $te^{-\alpha t}$  and von Neumann (i.e. 0-slope or symmetric) boundary condition was used on both sides. The appropriate P-S conversions and the reflections, diffractions satisfying Snell's law and Huygen's principle are clearly visible in these successive snapshots taken every sec.

### EXAMPLE 2

Figure 10 shows the snapshots of displacement fields generated by an upgoing P wave of velocity 5.2 km/sec in a grid of size 6.5km by 3.9km with steep topographic configuration. The successive frames separated by 0.125 sec show the initialization of the wave and locations of sensor 1 to 7 (left array), 8 to 17 (right array) which were separated 50 meters apart vertically (A), P-reflection followed by S wave starting at right (B,C), completely developed reflections from all parts of the topography (E) and complex wavefields containing reflections, diffractions and possibly excited surface waves (E,F). The initial P wave has an incident angle of  $20^\circ$  and the topography is a (due north  $344^\circ$ ) cross-section of Taourirt Tan Afella Massif in southern Algeria (Faure, 1972). This granite mountain rises from the (1100 meter elevation) Ahaggar plateau to a peak of 2100 meters in less than 1 km and has slopes that locally exceed  $53^\circ$ . Several nuclear tests were conducted here from 1962 to 1966. To cover a wide range of

slope in LFD calculation, a grid with horizontal spacing ( $\Delta x$ ) 0.05 km and vertical spacing ( $\Delta z$ ) 0.01 km was used. Figure 11 shows the dilatational strains recorded at 17 sensors buried beneath the peaks of the ridges. It can be observed that the free-surface reflection is severely altered due to scattering from the free-surface. The symmetric boundary conditions on the sides also causes some undesirable edge reflections from left side. For detailed discussion of this example and its applications in modeling teleseismic P waveforms observed at LRSM stations, see section 3 of this report.

### EXAMPLE 3

Figure 12 and 13 show a Rayleigh wave incident on an upgoing and a downgoing ramp of height  $h = 6.4 \text{ km} = 64 \Delta z$  respectively. The initial waveform is chosen so that the vertical displacement  $W$  on the flat free-surface is a Ricker wavelet. This wavelet has been adopted frequently in *finite-difference simulations* because it is well localized in both spatial and wavenumber domains (Boore, 1972; Munasinghe and Farnell, 1973; Fuyuki and Matsumoto, 1980; Fuyuki and Nakano, 1984; Levander, 1985). To avoid the grid dispersion, we chose  $3.2 \text{ km} = 32 \Delta x$  as the dominant wavelength of the incident Rayleigh wave packet in a homogeneous medium of P wave velocity 5 km/sec and Poisson ratio 0.35. Absorbing boundary conditions given by Clayton and Engquist (1977) and Emerman and Stephen (1983) were used on the sides and bottom to suppress the artificial reflections from the sides of the grid. Figures (A) through (F) correspond to displacement wavefields at distinct times with a temporal spacing of 2 sec. In both cases the corner points always act as point scatterers radiating converted body waves away in frames (C) through (F). Note that the diffracted pattern in the downgoing ramp case (Figure 13) is much more complicated than in the upgoing case (Figure 12) and that the quasi-transparent boundary conditions allow the wave to disappear into the sides and bottom of the grid. Even a moderate topography can substantially attenuate a short-period

fundamental Rayleigh wave due to body wave conversion (McLaughlin and Jih, 1986b). Such attenuation of short-period fundamental Rayleigh wave incident upon topography is usually stronger than that due to shallow heterogeneous sediment over homogeneous half space (McLaughlin and Jih, 1987).

## CONCLUSION

In this paper, we have presented a straightforward method to simulate the P-SV wave propagation in 2-D LFD models with free-surface topography. This method specifies the treatment of a polygonal boundary including the transition points between the straight line segments. Boundary conditions are implemented in a way that at transition points the normal axis always coincides with the bisector of the corner. This approach reflects the natural idea to account for the slope change along the topography. It is empirically stable for those Poisson ratios of interest even in models with quite complex topography and is suitable for the calculation of teleseismic P waves from explosive line source under realistic surfaces. The numerical scheme in the present work has truncation error of order one in spatial increment, consistent with the classical one-sided explicit extrapolation formulae widely used in the flat free-surface case. Schemes with higher order of accuracy might be harder to derive because of the asymmetrical differences and interpolations involved.

## ACKNOWLEDGEMENTS

This work was supported by DARPA contract F19628-85-C-0035 monitored by Air Force Geophysics Laboratory. The views and conclusions contained in this document are those of the authors and should not be interpreted as necessarily representing the official policies, either expressed or implied, of the Defense Advanced Research Projects Agency or the U.S. Government.

## REFERENCES

- Alterman, Z., and Karal, F. C., (1968), Propagation of elastic waves in layered media by finite difference methods: Bull. Seism. Soc. Am., **58**, 367-398.
- Alterman, Z., and Loewenthal, D., (1970), Seismic waves in a quarter and three quarter plane: Geophys. J. R. astr. Soc., **20**, 101-126.
- Alterman, Z., and Loewenthal, D., (1972), Computer generated seismograms, in *methods in computational physics*, vol. **12**, 35-164.
- Boore, D., (1972), Finite-difference methods for seismic wave propagation in heterogeneous materials, in *methods in computational physics*, vol. **11**, 1-37.
- Boore, D., Harmsen, S. C., and Harding, S., (1981), Wave scattering from a step change in surface topography: Bull. Seism. Soc. Am., **71**, 117-125.
- Clayton, R., and Engquist, B., (1977), Absorbing boundary conditions for acoustic and elastic wave equations: Bull. Seism. Soc. Am., **67**, 1529-1540.
- Emerman, S., and Stephen, R., (1983), Comment on "Absorbing boundary conditions for acoustic and elastic wave equations," by R. Clayton and B. Engquist, Bull. Seism. Soc. Am., **73**, 661-665.
- Faure, J., (1972), Recherches sur les effets geologiques d'explosions nucleaires southeraines dans un massif de granite Saharien, Centre d'Etudes de Bruyeres-le-Chatel, Commissariat a l'Energie Atomique, Rapport CEA-R-4257, Service de Documentation CEN-SACLAY B.P. no. 2, 91-GIF-sur-Yvette, France.
- Fuyuki, M., and Matsumoto, Y., (1980), Finite-difference analysis of Rayleigh wave scattering at a trench: Bull. Seism. Soc. Am., **70**, 2051-2069.
- Fuyuki, M., and Nakano, M., (1984), Finite-difference analysis of Rayleigh wave transmission past an upward step change: Bull. Seism. Soc. Am., **74**, 893-911.
- Hong, M. and L. J. Bond, (1986), Application of the finite difference method in seismic source and wave diffraction simulation: Geophys. J. R. astr. Soc., **87**, 731-752.
- Ilan, A., L. J. Bond, and M. Spivack, (1979), Interaction of a compressional impulse with a slot normal to the surface of an elastic half space: Geophys. J. R. astr. Soc., **57**, 463-477.
- Ilan, A., Ungar, A., and Alterman, Z., (1975), An improved representation of boundary conditions in finite-difference schemes for seismological problems: Geophys. J. R. astr. Soc., **43**, 727-745.
- Ilan, A., (1977), Finite-difference modeling for P-pulse propagation in elastic media with arbitrary polygonal surface: J. Geophys., **43**, 41-58.
- Kelly, K.R., Ward, R.W., Treitel, S., and Alford, M., (1976), Synthetic seismograms : a finite-

difference approach: *Geophysics*, 41, 2-27.

Levander, A., (1985), Finite-difference calculations of dispersive Rayleigh wave propagation: *Tectonophysics*, 113, 1-30.

McLaughlin, K.L., and Jih, R.-S., (1986a), Scattering from near-source topography: teleseismic observations and numerical 2-D explosive line source simulations, *AFGL-TR-86-0159, Scientific Report #1, TGAL-86-03*, Teledyne Geotech, Alexandria, Virginia (section 3 of this report, submitted for publication).

McLaughlin, K.L., and Jih, R.-S., (1986b), Finite-difference simulations of Rayleigh wave scattering by rough topography, *AFGL-TR-86-0269, Scientific Report 3, TGAL-86-09*, Teledyne Geotech, Alexandria, Virginia (submitted for publication).

McLaughlin, K.L., and Jih, R.-S., (1987), Finite-difference simulations of Rayleigh wave scattering by shallow heterogeneity, *TGAL-87-02, Scientific Report 1*, Teledyne Geotech, Alexandria, Virginia.

Munasinghe, M., and Farnell, G., (1973), Finite-difference analysis of Rayleigh wave scattering at vertical discontinuities: *J. Geophy. Res.*, 78, 2454-2466.

## FIGURE CAPTIONS

FIGURE 1. Cartesian coordinate system in 2-D finite-difference scheme and miscellaneous corner points on the topography. Wave propagation is constrained to lie in this X-Z plane. Labels of the points correspond to the specific algorithm to use. It suffices to use combination of such transition points and points on inclined surface to approximate any polygonal topography.

FIGURE 2. Ramp with slope  $2\Delta z/\Delta x$ . Same algorithm applies to any ramp with slope  $m\Delta z/\Delta x$ ,  $m \geq 2$ .

FIGURE 3. Ramp with slope  $\Delta z/\Delta x$ .

FIGURE 4. The bottom of a canyon of slope  $2\Delta z/\Delta x$ . Same algorithm applies to any horizontal-to-inclined transition of slope  $m\Delta z/\Delta x$  where  $m \geq 1$ .

FIGURE 5. Corner where slope changes from  $n\Delta z/\Delta x$  to  $m\Delta z/\Delta x$ ,  $m > n$ .

FIGURE 6A. Corner where slope changes from  $n\Delta z/\Delta x$  to  $\Delta z/\Delta x$ ,

FIGURE 6B. Corner where slope changes from  $n\Delta z/\Delta x$  to  $m\Delta z/\Delta x$ ,  $1 < m < n$ .

FIGURE 7. Inclined-to-horizontal transition.

FIGURE 8. Example of steep slope  $m\Delta z/\Delta x$ ,  $m = 4$ . The inner points  $\langle i+1, k \rangle$  to  $\langle i+1, k-4 \rangle$  require fictitious points at  $\langle i, k-1 \rangle, \dots, \langle i, k-4 \rangle$  for solution of equation (1).

FIGURE 9. Snapshots of displacement fields generated by a normally incident P wave propagating across a homogeneous medium of size 39km by 26km (390 x 260 mesh points) with a  $45^\circ$  ramp on the top. Frames are separated by 1 sec and the darkness in each frame is proportional to the displacement. Note the reflection at the inclined surface breaks up into P- and S-waves, and the lower corner radiates body waves away circularly (C).

FIGURE 10. Snapshots of displacement fields with temporal spacing 0.125 sec generated by a broadband P waves incident on a 6.5km by 3.9km (130 x 390 mesh points) cross-section of Taourirt Tan Afella Massif with P wave velocity 5.2 km/sec. The incident P wave has an incident angle of  $20^\circ$ .

FIGURE 11. Dilatational strain recorded at 17 sensors buried beneath the peaks of the topographic profile. Sensors are 50 meters apart vertically with locations shown by solid circles in Figure 10A. Number 1 through 7 (from top to bottom) are on the left array.

FIGURE 12. Rayleigh wave incident on a 6.4 km-high upgoing ramp. Snapshots show the displacement wavefields with temporal spacing 2 sec. The body waves excited by Rayleigh waves on encountering the corners are clearly seen propagating away circularly in frames (C) through (F). Note that the diffracted P and S waves propagate mainly to the right while for downgoing ramp (Figure 13) the diffracted body waves propagate more isotropically.

FIGURE 13. Same as Figure 12 except for opposite direction of the ramp. The diffracted

wavefield is more complicated as compared to the case of upgoing cliff with the same height (Figure 12). Note the constructive interference of the forward-scattered S wave by the two corners and destructive interference for the back-scattered S wave.

FIGURE 14. Ilan's approach for inclined surface. A nonuniform grid with varying  $\Delta x$  is required in order to apply this algorithm to realistic polygonal free-surface.



## APPENDIX

## ILAN'S METHOD FOR CONSTANT SLOPE RAMP

For grid point  $\langle i, k \rangle$  on an inclined free-surface with slope  $\Delta z / \Delta x$  (Figure 17), let

$$U'_{i,k} = U'_0 - \sin 2\theta (W'_{i+1,k} - W'_{i,k+1}) \quad (15a)$$

$$W'_{i,k} = W'_0 - \sin 2\theta \left(1 - 2 \frac{\beta^2}{\alpha^2}\right) (U'_{i+1,k} - U'_{i,k+1}) \quad (15b)$$

where

$$U_0 = \epsilon_0 U_{i+1,k+1} + (1 - \epsilon_0) U_{i,k+2} \quad (16a)$$

$$W_0 = \epsilon_0 W_{i+1,k+1} + (1 - \epsilon_0) W_{i,k+2} \quad (16b)$$

$$\epsilon_0 = 2 \sin^2 \theta \quad \text{if } \theta \leq 45^\circ,$$

$$\theta = \tan^{-1}(\Delta z / \Delta x),$$

if  $\theta \geq 45^\circ$ , then take  $\epsilon_0 = 2 \cos^2 \theta$ , and replace equations (16a) and (16b) by

$$U_0 = \epsilon_0 U_{i+1,k+1} + (1 - \epsilon_0) U_{i+2,k} \quad (16c)$$

$$W_0 = \epsilon_0 W_{i+1,k+1} + (1 - \epsilon_0) W_{i+2,k} \quad (16d)$$

Then rotate  $U'_{i,k}$ ,  $W'_{i,k}$  back to the original system. We have observed that without appropriate manipulation of the transition points on the topography as proposed in the present work, this algorithm alone would suffer from instabilities.

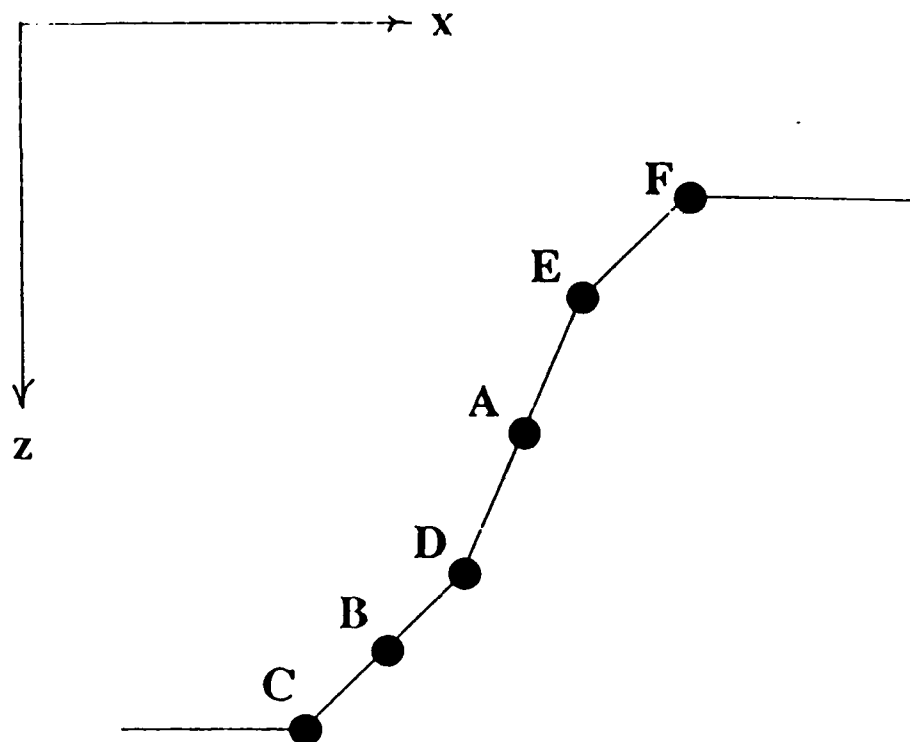


Figure 1.

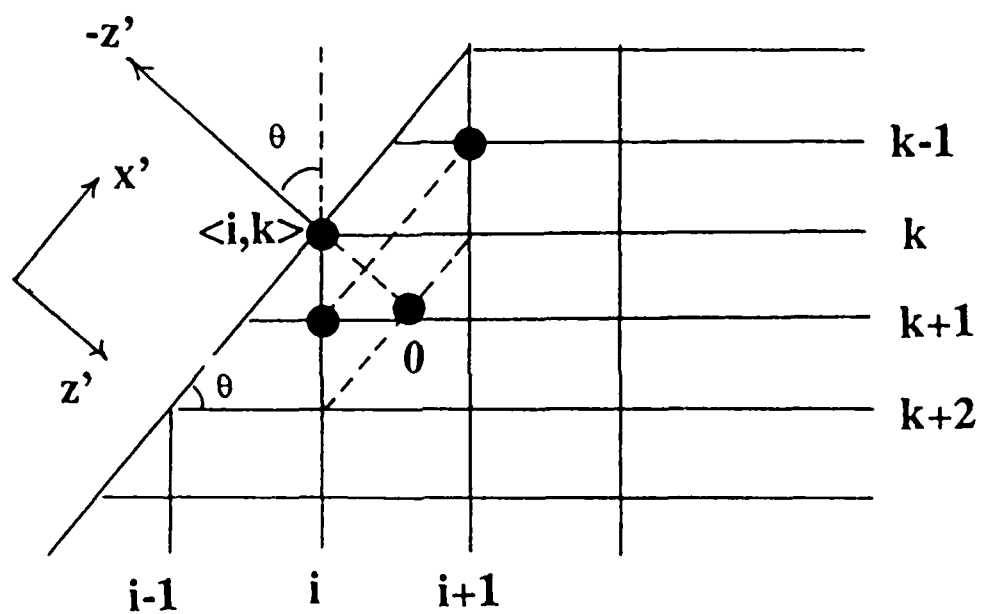


Figure 2.

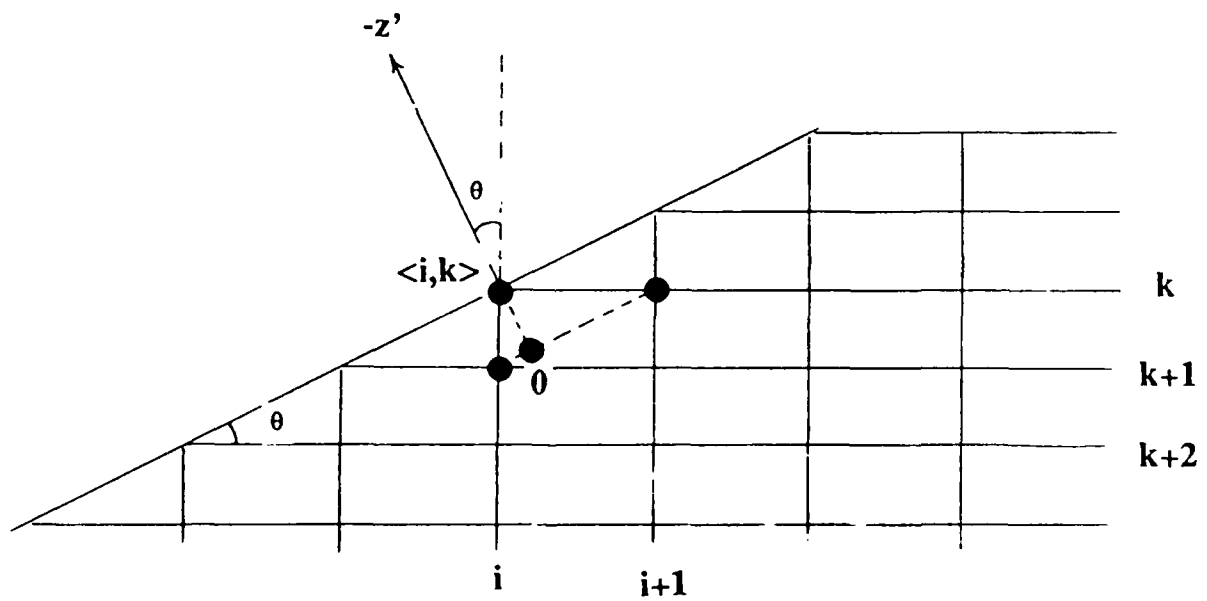


Figure 3.

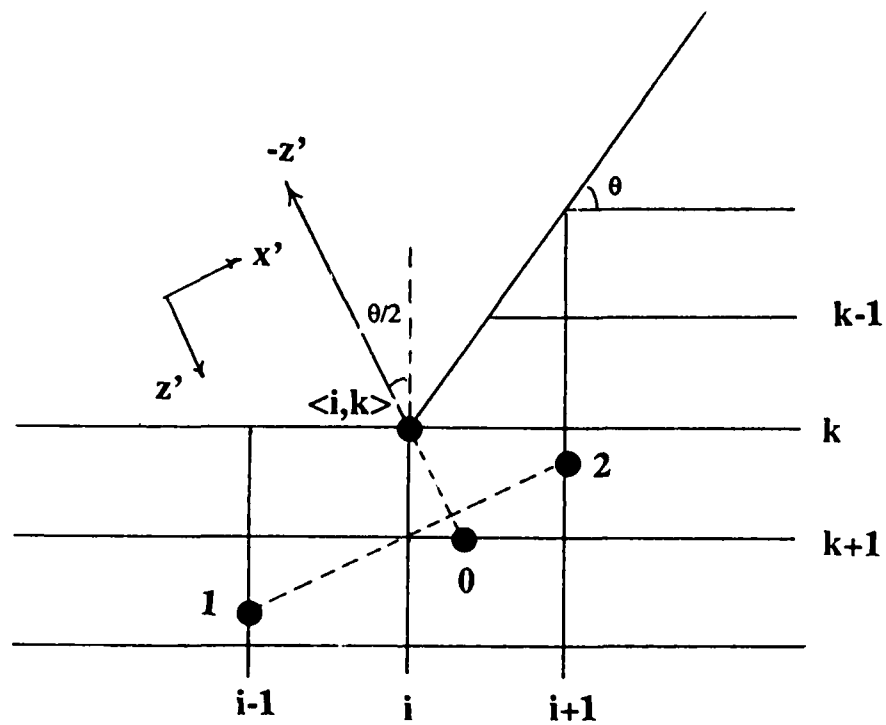
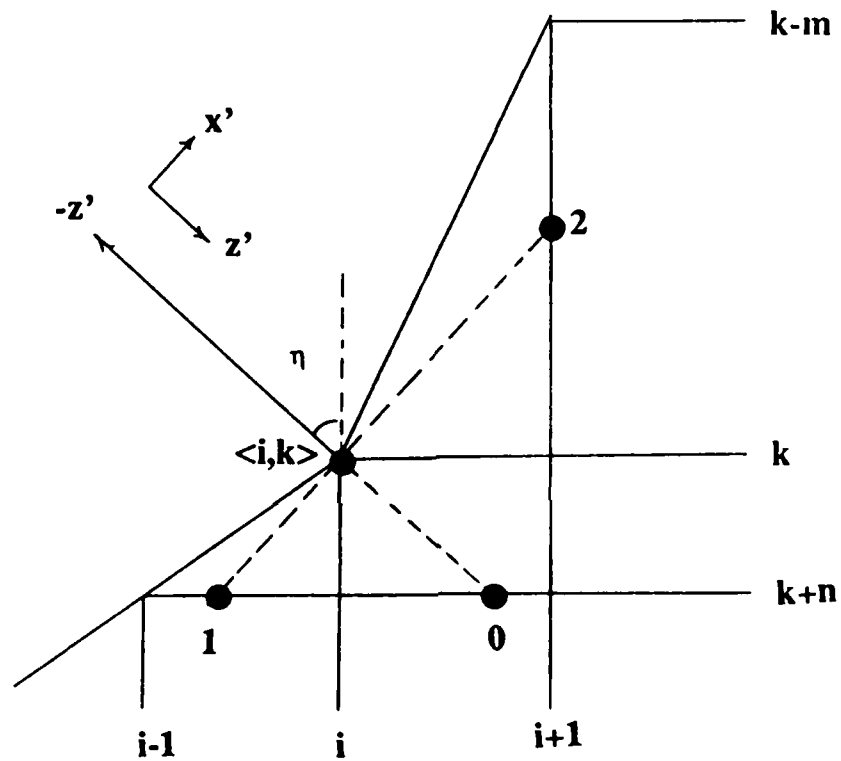
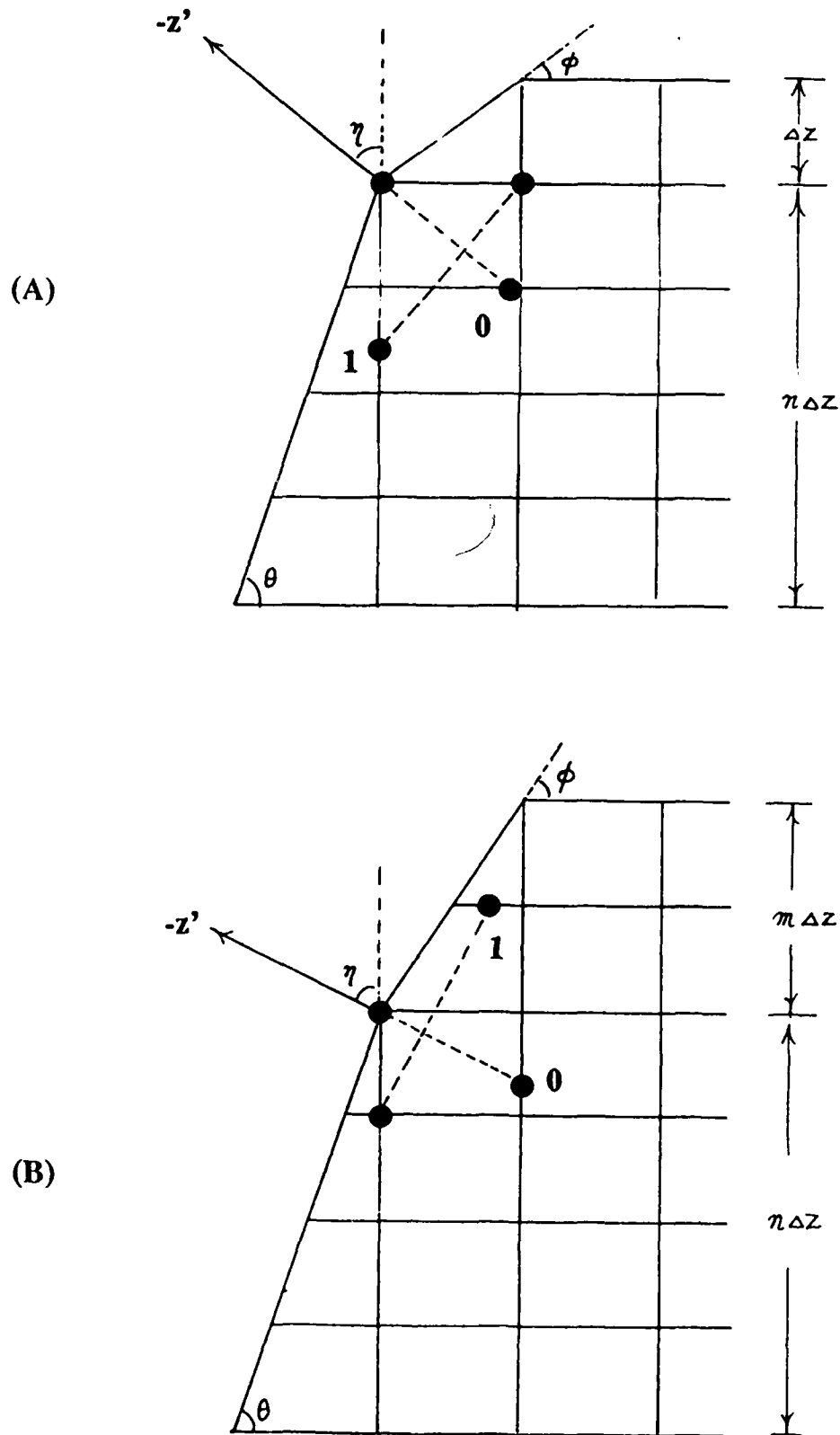


Figure 4.



**Figure 5.**



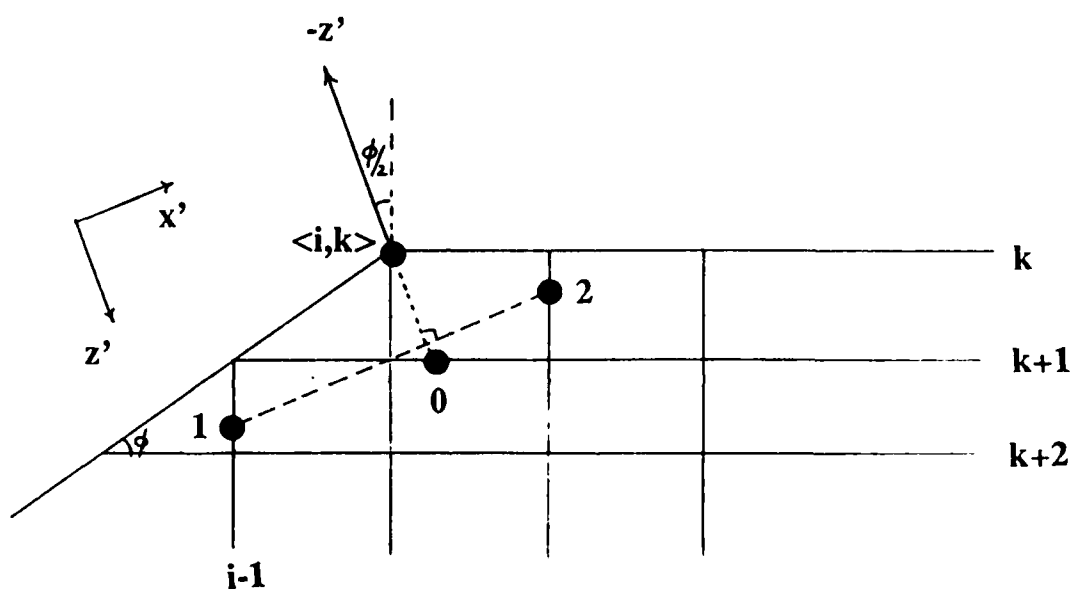


Figure 7.



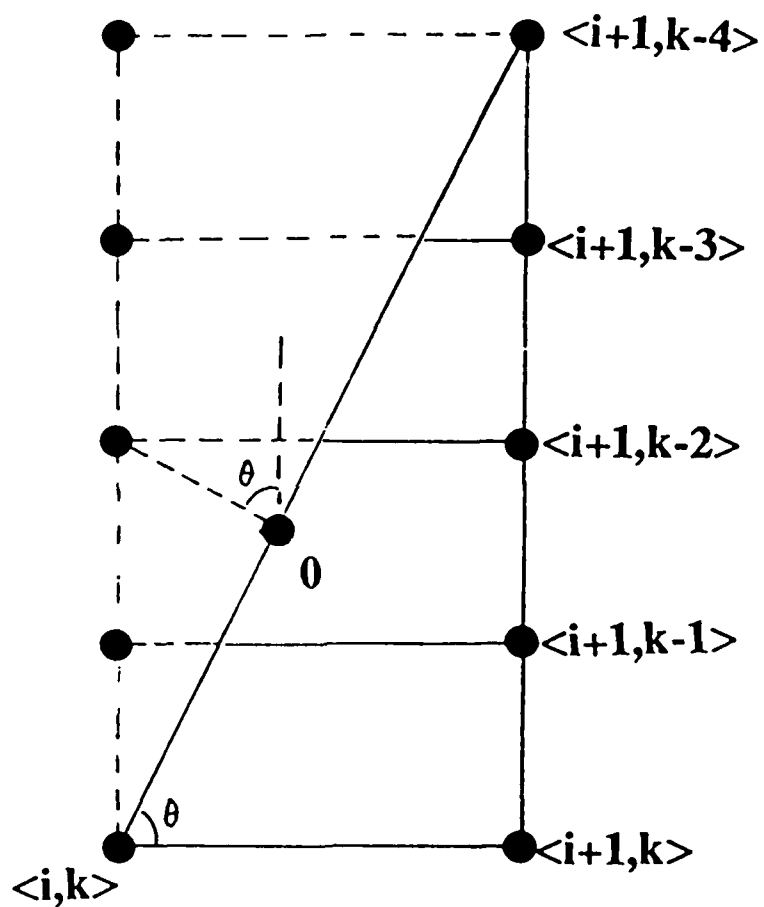


Figure 8.

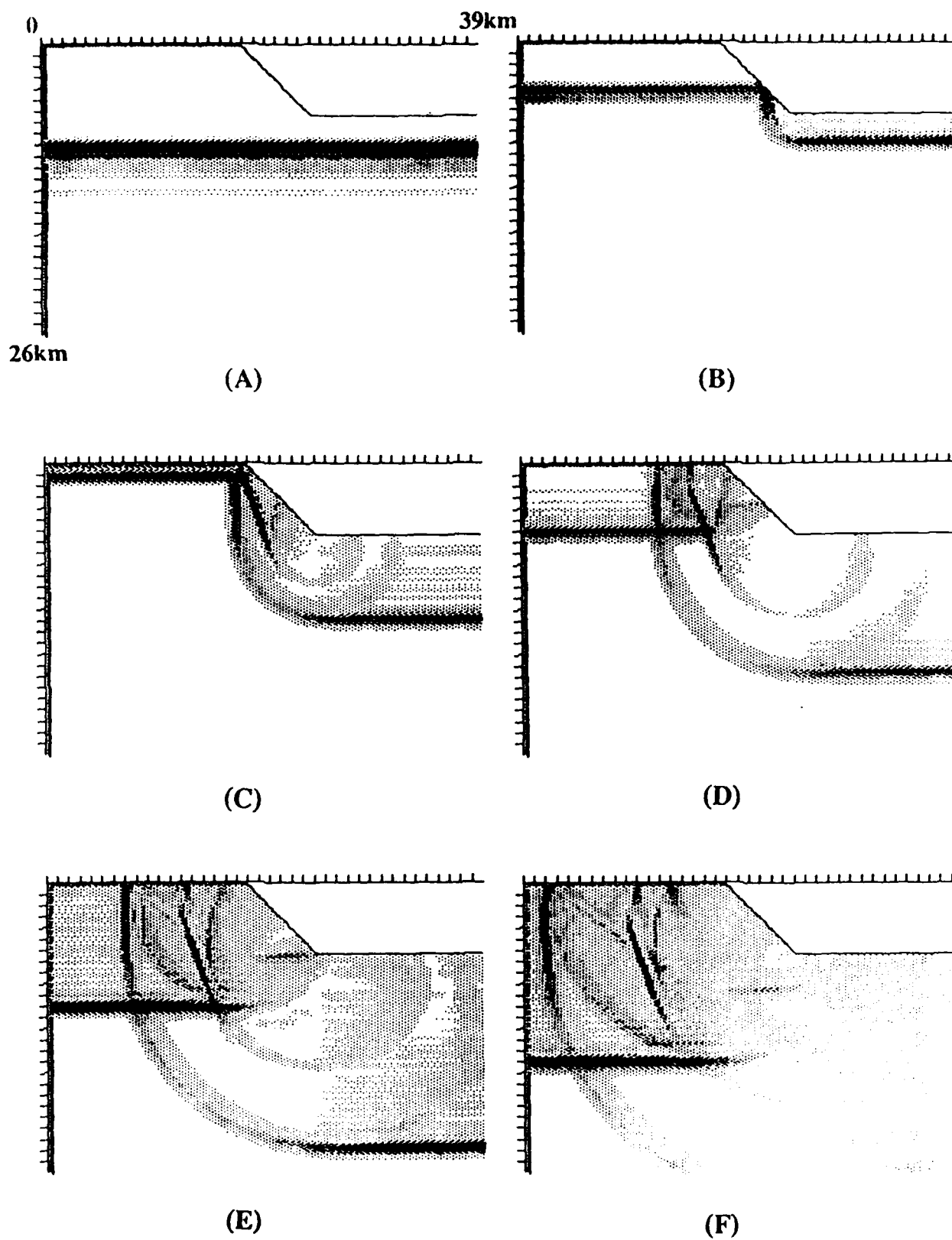


Figure 9.

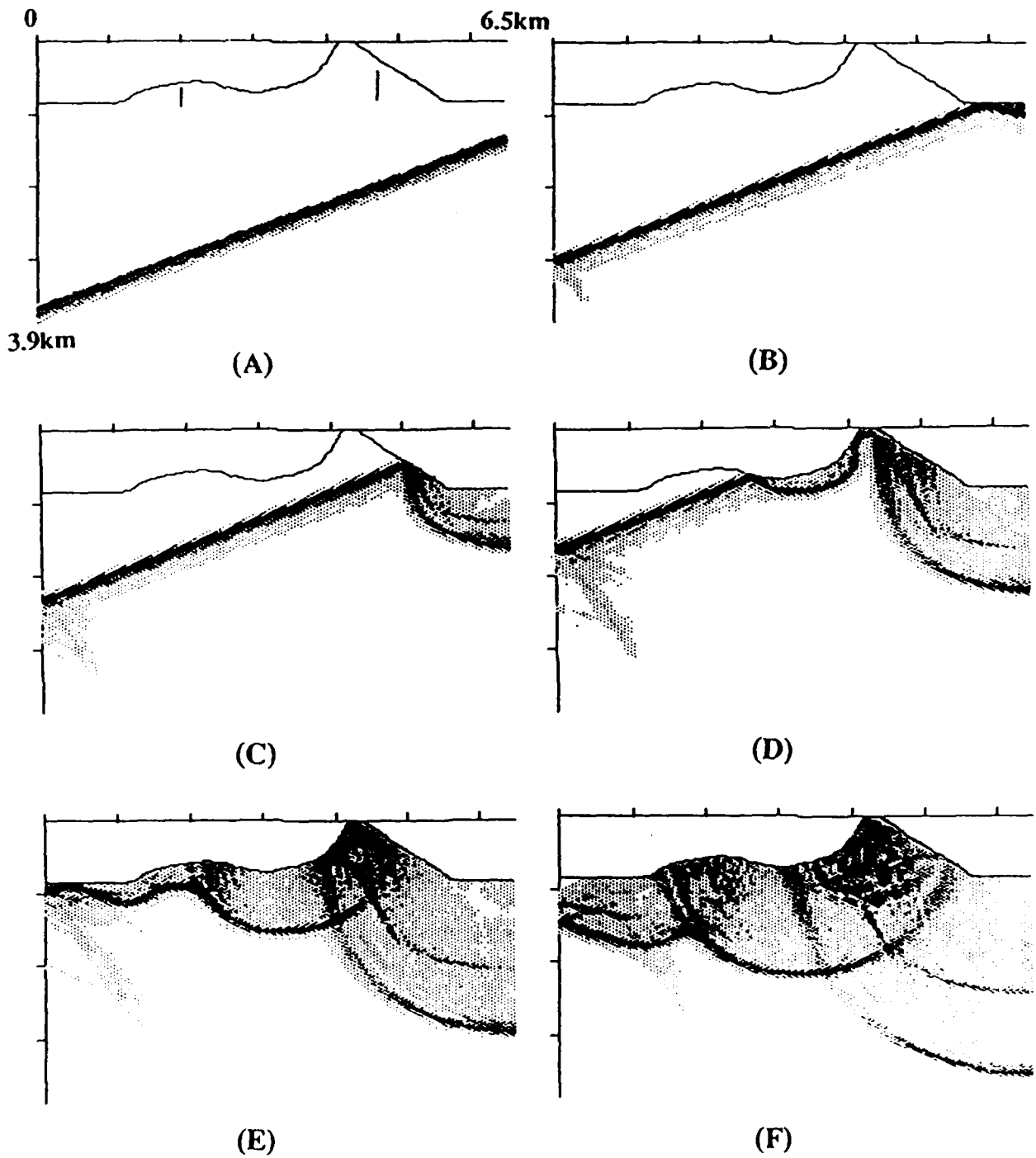


Figure 10.

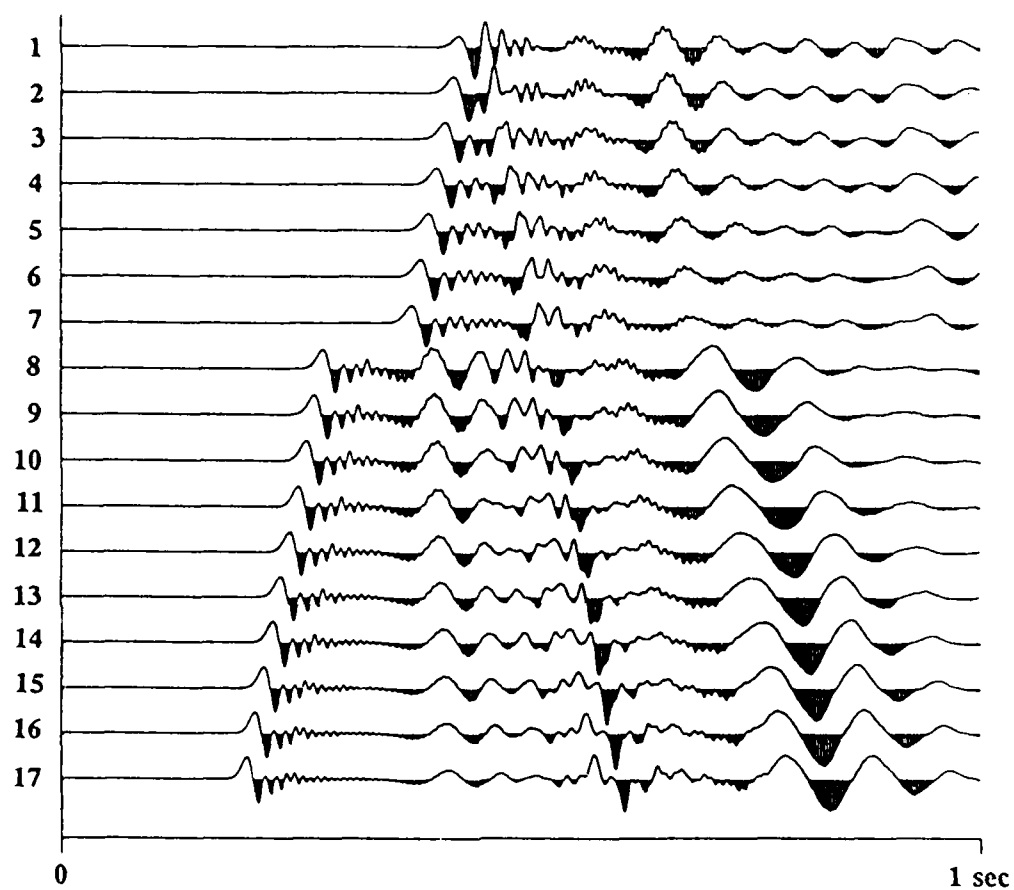
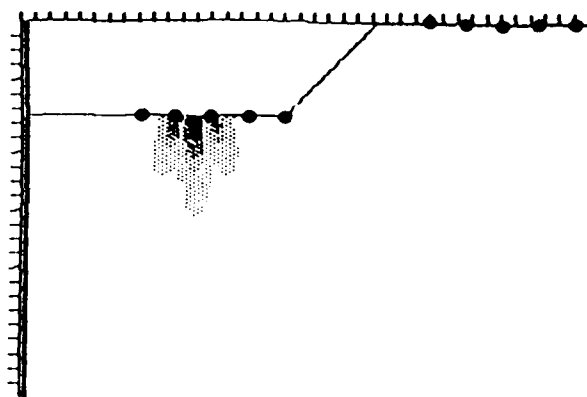
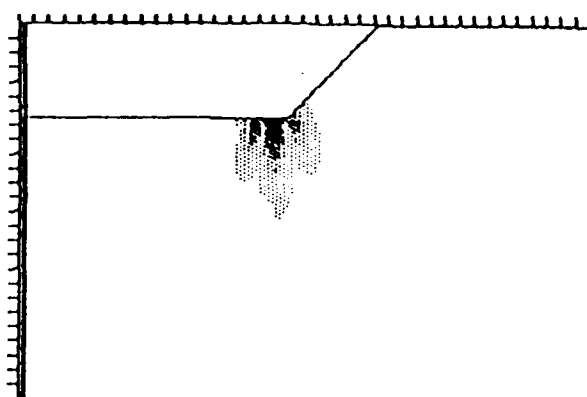


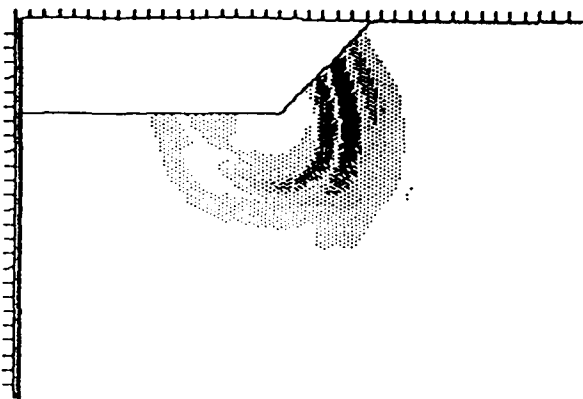
Figure 11.



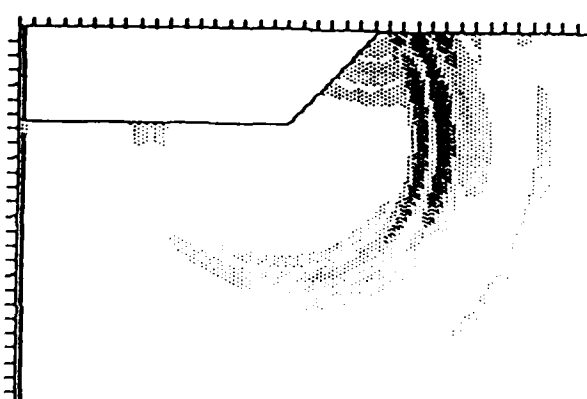
(A)



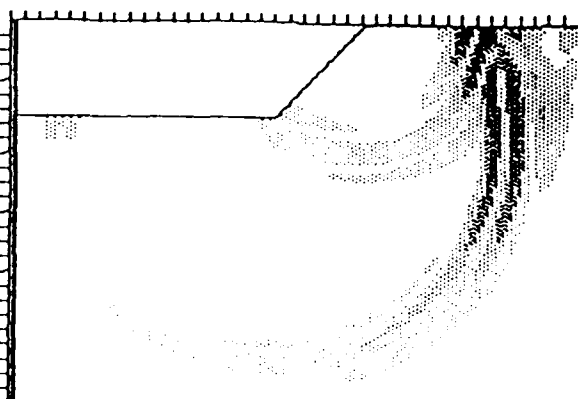
(B)



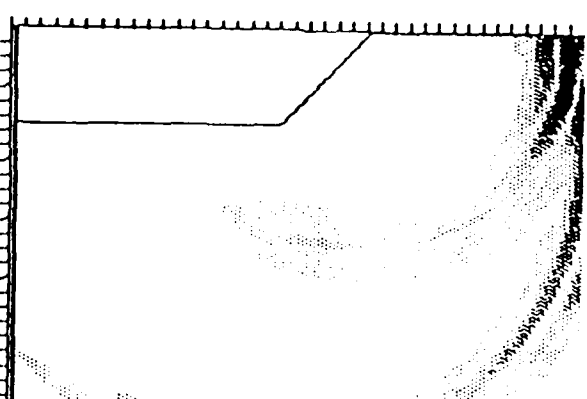
(C)



(D)

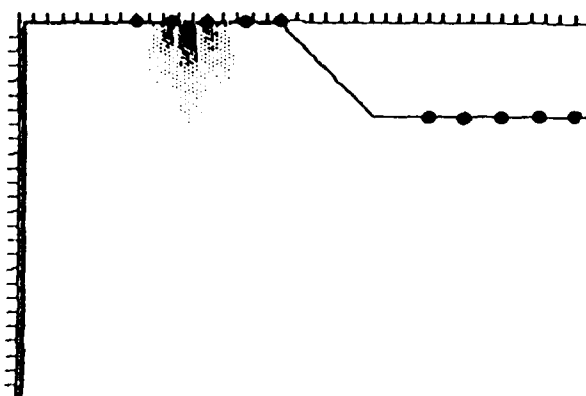


(E)

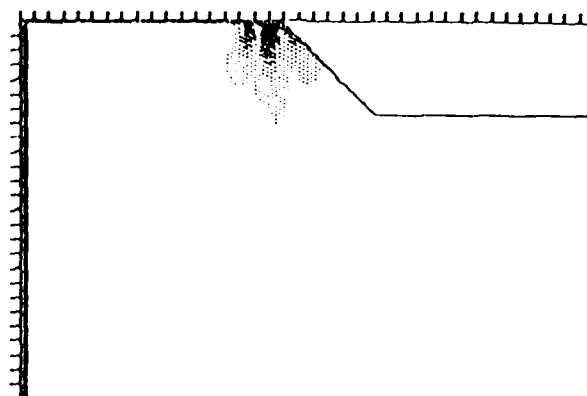


(F)

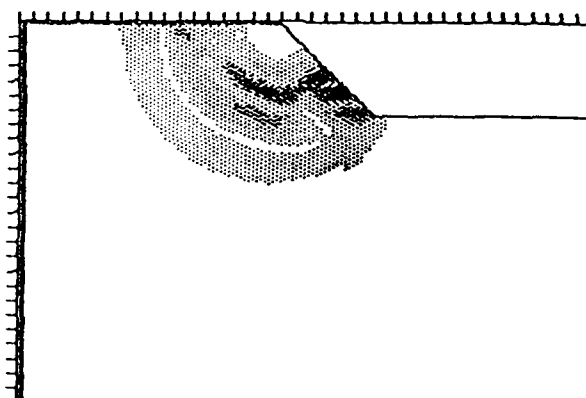
Figure 12.



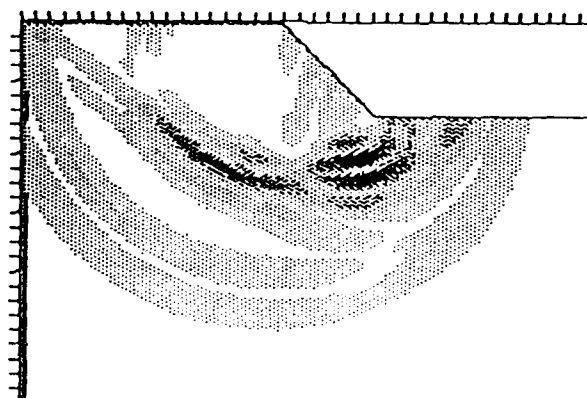
(A)



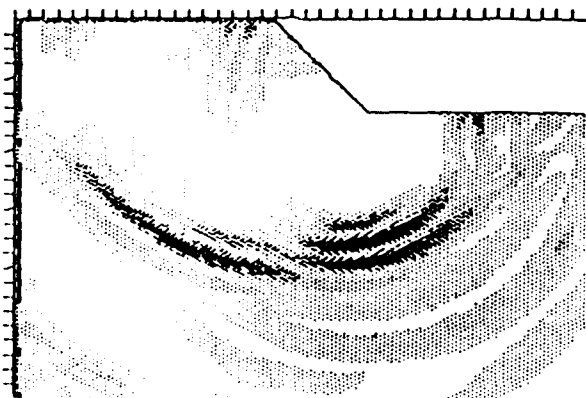
(B)



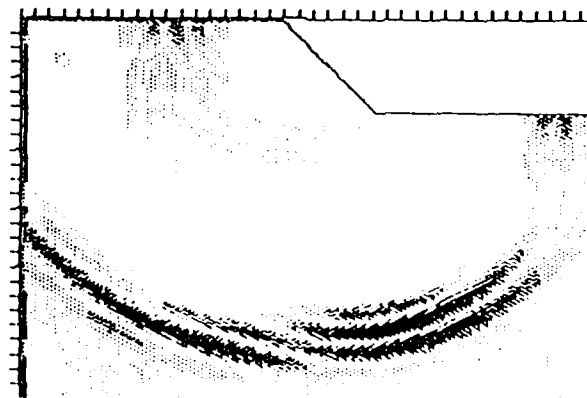
(C)



(D)



(E)



(F)

Figure 13.

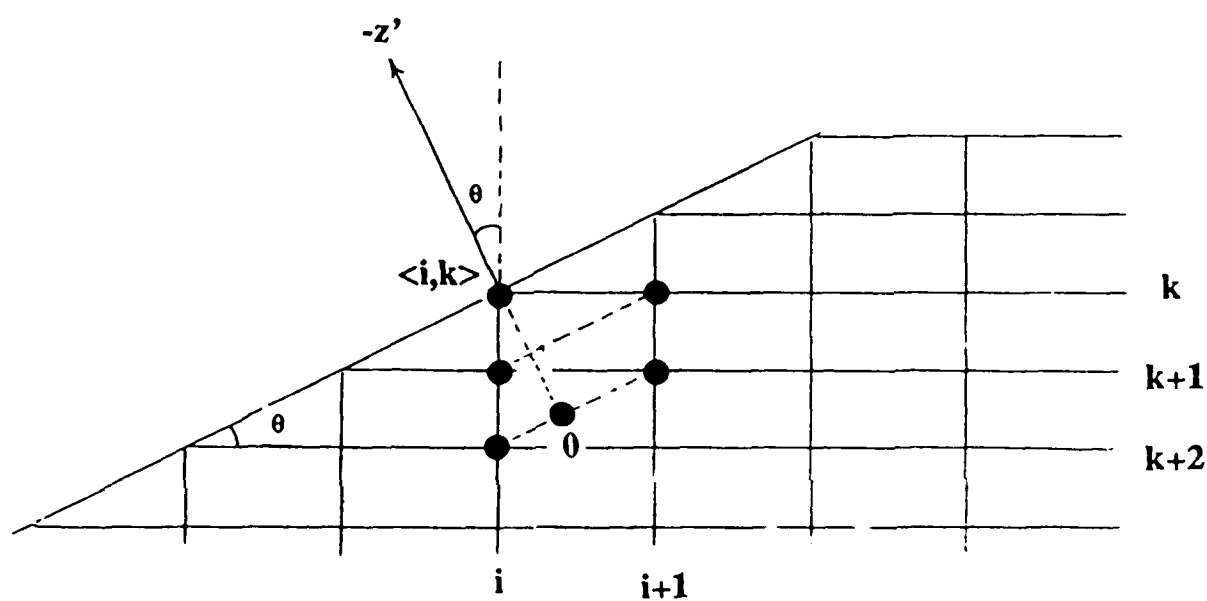


Figure 14.

(THIS PAGE INTENTIONALLY LEFT BLANK)



## SECTION 2

TELESEISMIC SPECTRAL AND TEMPORAL  
 $M_0$  AND  $\Psi_\infty$   
ESTIMATES FOR FOUR FRENCH  
EXPLOSIONS IN SOUTHERN SAHARA

K. L. McLaughlin, A. C. Lees, and Z. A. Der  
Teledyne Geotech Alexandria Laboratories  
314 Montgomery St.  
Alexandria, VA 22314

## INTRODUCTION

Several contained nuclear explosive tests were conducted in southern Sahara from 1962 to 1966. These tests are reported in Duclaux and Michaud (1970) and Faure (1972). Because U.S. testing experience in granite is limited, these tests present an opportunity to extend the U.S. knowledge of tests in granite. In this paper we report on estimates of the explosion source from short period Long Range Seismic Measurements (LRSM) stations and the AWRE U.K. arrays EKA and YKA. We estimate the explosion source strength parameterized as the low frequency limit of the seismic moment,  $M_0$ , or the low frequency limit of the reduced displacement potential (RDP),  $\Psi_\infty$ .

Schock *et al.* (1972) and Heuze (1983) report on geophysical parameters of the Taourirt Tan Afella Massif located in southern Algeria. We have adopted the values of P-wave velocity,  $\alpha = 5.8$  km/s, S-wave velocity  $\beta = 3.3$  km/s, and density  $\rho = 2.6$  gm/cc as representative of the material in the vicinity of the tests. The Taourirt Tan Afella Massif is located on the Ahaggar plateau identified by Crough (1981) as a 1000 km wide dome of continental crust uplifted by a mantle hot spot. The dome has an average elevation of 1100 meters and is capped by late Tertiary alkali basalt volcanos. The Taourirt Tan Afella Massif is a 16 km<sup>2</sup> granite mountain that rises to a 2100 meter peak in a lateral distance of less than 1 km. Given

this tectonic setting, the source region  $\bar{t}^*$  estimate of 0.35 sec given by Der *et al.* (1985a and b) is in accord with an upper mantle of high intrinsic attenuation.

Figure 1 shows the location of the test site, several LRSM stations and the arrays EKA and YKA analyzed in this paper. Table 1 gives the origin times and locations given by Duclaux and Michaud (1970) for the four explosions analyzed in this paper. Figure 2 shows these locations superimposed on a topographic map from Faure (1972).

TABLE 1.

DATE	ORIGIN TIME	LAT (N)	LONG (E)	EVENT
1963/03/18	10:02:00.351	24.0414	5.0522	EMERAUDE
1963/10/20	13:00:00.011	24.0355	5.0386	RUBIS
1965/02/27	11:30:00.039	24.0587	5.0312	SAPHIR
1966/02/16	11:00:00.035	24.0442	5.0412	GRENAT

### $\bar{t}^*$ ESTIMATES FOR THE SOUTHERN SAHARA TEST SITE

Before explosion size estimates may be made, the intrinsic attenuation for the paths must be determined. We follow a procedure much like that in Der *et al.* (1985) to partition the  $\bar{t}^*$  estimate into a source  $\bar{t}^*$  and a receiver  $\bar{t}^*$ . In order to estimate intrinsic attenuation for the available paths, a procedure was followed similar to one described in Der and Lees (1985). The seismic spectra were corrected for instrument response and approximate von Seggern and Blandford (1972) RDP. The far-field P-wave spectra is assumed to be proportional to

$$\frac{(1+A^2K^2)^{1/2}}{(1+K^2)^{3/2}}$$

where  $A=5.08$ ,  $K=\omega/k$ , and  $k=16.8(5/Y)^{1/3}$ . Marshall *et al.* (1979) give the yields for RUBIS and SAPHIR as  $Y=52$  and  $Y=120$  KT respectively. The corrected amplitude spectra in the bandwidth between 0.5 and 3.0 Hz were fit to a form of  $\Omega_0 \exp(-\pi \bar{t}^* f)$ . Signal-to-noise estimates for each frequency were estimated and only those values with an estimated

(signal+noise)-to-noise power ratio greater than 2 were used. The signal spectra were generally absent of any useful information for frequencies above 3 Hz. Whole path  $\bar{t}^*$  estimates are listed for each station in Table 2 along with estimated standard errors. Only RUBIS and SAPHIR were large enough to permit useful estimates of  $\bar{t}^*$ . Figure 3 shows examples of spectra corrected for instrument response and von Seggern and Blandford (1972) RDP.

We assume that the whole path  $\bar{t}^*$  is the sum of the station  $\bar{t}^*$  plus the test site  $\bar{t}^*$ , and we wish to estimate the test site  $\bar{t}^*$ . Der *et al.* (1985a) list  $\bar{t}^*$  contributions to be expected for RK-ON, EKA, YKA, HN-ME, NP-NT, CPO, NAO, and GRFO. The sites RK-ON, SB-GR, and OO-NW are now occupied by RSON, GRFO, and NAO respectively. Given these station estimates for  $\bar{t}^*_{\text{p}}$ , we estimate  $\bar{t}^*_{\text{p}}$  for Ahaggar as 0.31 (0.04) sec. Der *et al.* (1978) list estimates for short period S-wave  $\bar{t}^*_{\text{S}}$  for the LRSM stations BL-WV, RK-ON, RY-ND, VO-IO, DH-NY, HL-ID, KN-UT, MN-NV, FR-MA, LC-NM, RT-NM, and GI-MA. Assuming  $\bar{t}^*_{\text{S}} = 4 \bar{t}^*_{\text{p}}$ , the test site estimate for Ahaggar  $\bar{t}^*_{\text{p}}$  is 0.26 (0.05) sec. Because this value depends on more assumptions relating  $\bar{t}^*_{\text{S}}$  to  $\bar{t}^*_{\text{p}}$ , it is probably less reliable. All these data are consistent with the Der *et al.* (1985b) estimate of 0.35 sec for the southern Algeria test site.

TABLE 2.

$\bar{t}^*$ ESTIMATES FROM RUBIS AND SAPHIR		
STATION	$\bar{t}^*$ sec	$\sigma$ sec
BL-WV	0.37	0.04
BR-PA	0.53	0.06
CPO	0.53	0.06
DH-NY	0.46	0.12
EB-MT	0.62	0.04
EKA	0.52	0.10
EU-AL	0.44	0.06
FR-MA	0.50	0.06
SB-GR	0.55	0.06
GI-MA	0.48	0.07
HL-ID	0.51	0.04
HN-ME	0.34	0.04
KN-UT	0.69	0.04
LC-NM	0.59	0.03
NP-NT	0.49	0.07
OO-NW	0.46	0.06
RK-ON	0.37	0.05
RT-NM	0.70	0.04
RY-ND	0.57	0.06
VO-IO	0.49	0.07
WO-AZ	0.80	0.05
YKA	0.45	0.10

SPECTRAL ESTIMATES FOR  $\Omega_0$ ,  $M_0$ , and  $\Psi_\infty$ 

In addition to the slope of each spectra, the zero frequency limit,  $\Omega_0$ , was estimated for each spectra. These values are tabulated in Table 3 along with estimates for  $M_0$  and  $\Psi_\infty$  derived from geometrical spreading given by the J.B. travel time tables (Aki and Richards, 1980). In the calculations, surface values at each station of  $\alpha$ ,  $\beta$ , and  $\rho$  were assumed to be  $\alpha = 5.8$  km/sec,  $\beta = 3.3$  km/sec, and  $\rho = 2.6$  gm/cc, except for the stations RK-ON, EU-AL, BL-WV, KN-UT, HN-ME, DH-NY, HL-ID, NP-NT, and BR-PA where  $(\alpha, \beta, \rho)$  values were obtained from Der *et al.* (1977). These values are also listed in Table 3.

TABLE 3.

RUBIS AND SAPHIR LRSM SPECTRAL MOMENT ESTIMATES								
STATION	$\Delta$ deg	$t^*$ s	$\Omega_0$ nm-s	$\rho$ gm/cc	$\alpha$ km/s	$\beta$ km/s	$M_0$ dyne-cm	$\Psi_\infty$ m <sup>3</sup>
RUBIS								
BL-WV	72.6	0.37	50.	2.7	6.0	3.46	3.77E+22	3433.
DH-NY	66.7	0.46	28.	2.7	6.0	3.46	2.07E+22	1889.
EB-MT	78.1	0.62	102	2.6	5.8	3.3	8.04E+22	7321.
EU-AL	79.4	0.44	189.	1.9	2.7	1.4	8.93E+22	8121.
FR-MA	86.3	0.50	118.	2.6	5.8	3.3	1.00E+23	9136.
GI-MA	84.4	0.48	97.	2.6	5.8	3.3	8.14E+22	7409.
HL-ID	92.2	0.51	45.	2.5	5.2	2.96	7.82E+22	7116.
HN-ME	61.2	0.34	50.	2.7	5.9	3.36	3.14E+22	2861.
KN-UT	95.3	0.69	28.	2.0	3.15	1.81	3.73E+22	3394.
LC-NM	93.6	0.59	53.	2.2	3.0	1.6	7.28E+22	6628.
OO-NW	36.7	0.46	70.	2.6	5.8	3.3	3.86E+22	3512.
RK-ON	76.6	0.37	56.	2.7	5.64	3.47	4.37E+22	3982.
SB-GR	25.6	0.55	252.4	2.6	5.8	3.3	5.87E+22	5343.
SAPHIR								
BL-WV	72.6	0.37	178.	2.7	6.0	3.46	1.32E+23	12031.
BR-PA	70.2	0.53	206.	2.7	6.0	3.46	1.55E+23	14105.
HN-ME	61.2	0.34	77.	2.7	5.9	3.36	4.85E+22	4420.
KN-UT	95.3	0.69	52.	2.0	3.15	1.81	7.00E+22	6374.
LC-NM	93.6	0.59	176.	2.2	3.0	1.6	2.40E+23	21870.
RT-NM	89.8	0.70	334.	2.6	5.8	3.3	6.76E+23	61521.
RY-ND	82.4	0.57	237.	2.6	5.8	3.3	1.94E+23	17694.
VO-IO	78.9	0.49	196.	2.6	5.8	3.3	1.55E+23	14103.
WO-AZ	95.1	0.80	484.	2.6	5.8	3.3	9.91E+23	90171.

$M_0 = 4\pi\rho\alpha^2 \Psi_\infty$  was assumed to relate the static moment,  $M_0$ , to the RDP level,  $\Psi_\infty$ .

Several statistics, shown in Table 4, are provided for the "network" estimate of  $M_0$ , including a straight average, the rms value, and the geometric mean. Following McLaughlin (1986) we consider the rms value to be the best estimate of the absolute static moments. However, the ratio of the geometric mean (logarithmic average) should be a better estimate of the relative source size of the two events. The stations RT-NM, and WO-AZ have large amplitudes that may be due to deep soft sediment amplification. The "network"  $M_0$  estimates appear to be log-normally distributed and the variance dominated by focusing-defocusing amplitude fluctuations with a  $\sigma$  for  $\log_{10}(M_0)$  of about 0.24 magnitude units for RUBIS and 0.39 for SAPHIR. The

four sites that recorded both RUBIS and SAPHIR give source size ratios of 0.29, 0.65, 0.54, and 0.31 for BL-WV, HN-ME, KN-UT, and LC-NM, respectively. The average log-ratio of these four stations is -0.37. This is consistent with the log-ratio of the yields of the two events, -0.36.

TABLE 4.

LRSM SPECTRAL MOMENT ESTIMATES $10^{24}$ dyne-cm				
EVENT	MEAN	RMS	GEOMETRIC MEAN	MEDIAN
RUBIS	0.064(0.01)	0.072	0.056	0.059
SAPHIR	0.30(0.10)	0.42	0.19	0.16

Der *et al.* (1982) have proposed frequency dependent attenuation models,  $t^*(f)$ , for tectonic and shield regions. Since  $\bar{t}^* = t^* + f \frac{dt^*}{df}$ , the spectral correction made for frequency independent  $t^*$  may be in error by the factor  $\exp(-\pi f^2 \frac{dt^*}{df})$ . The Der *et al.* (1982) tectonic model for  $t^*(f)$  has a slope at 1 Hz of about -0.2 sec/Hz. Therefore, the estimates of  $M_0$  and  $\Psi_\infty$  could be larger by a factor of about 1.9. This factor is largely uncertain due to the uncertainty in the frequency dependence of  $Q(f)$  in the mantle on a regional basis in the 0.5 to 2.0 Hz bandwidth.

### DECONVOLUTIONS AT EKA AND YKA

The method of Shumway and Der (1985) was used to deconvolve the array data for EMERAUDE, GRENAT, RUBIS, and SAPHIR at EKA and YKA. A constant  $\bar{t}^* = 0.45$  seconds was assumed (Der *et al.*, 1985a and 1985b). Estimates for the equivalent far-field seismic source displacement time functions are shown in Figure 4 for EKA and YKA. The estimates for SAPHIR differ between EKA and YKA with the presence of a negative pulse following the positive pulse at EKA and the absence of such a pulse at YKA. RUBIS was

poorly recorded at YKA. The absence of the negative pulse (pP?) following the main SAPHIR P pulse at YKA as well as the variation between EKA and YKA for all of the events suggest that the topography in the immediate vicinity of the explosions may have influenced the later arrivals. The azimuths to EKA and YKA from SAPHIR and RUBIS are shown in Figure 2.

Estimates of the integrated area of the positive pulses are shown in Figures 5A, B, C and D and tabulated in Table 5. These measurements are similar to the measurements of pulse area made from deconvolved records used by Douglas *et al.* (1986) to estimate source size for the three Amchitka explosions. Two methods were used. In the first method, area was estimated within the pulse defined by the boxes indicated in Figure 5A and B. In the second method, the displacement far-field source time function estimate was integrated and the causal step was estimated as indicated in Figure 5C and 5D.

Also, the spectral intercept was estimated from the spectra at EKA as with the LRSM data. The spectral estimate for  $\Omega_0$  was identical to the average spectral estimate for  $\Omega_0$  made at EKA for RUBIS. The  $M_0$  estimates for RUBIS and SAPHIR fall within the population of values from the LRSM network of stations, Table 3. The network scatter far exceeds any formal error in the estimates made at any given station within the network.

TABLE 5.

EVENT	$M_0 \cdot 10^{24}$ dyne-cm		$\Psi_\infty \cdot m^3$	
	EKA	YKA		
SAPHIR	0.05	0.03	4600	2700
RUBIS	0.03	----	2700	----
GRENAT	0.008	0.004	730	360
EMERAUDE	0.01	0.002	900	730

#### LRSM TIME DOMAIN DECONVOLUTIONS

The waveform data for RUBIS and SAPHIR were deconvolved to ground displacement at several of the LRSM stations by removing the effects of the instrument and an estimated attenuation operator. The Azimi *et al.* (1968) constant  $t^*$  operator was used. In order to limit the bandwidths of the deconvolution, a filter was applied to each deconvolution that maximizes the useful signal bandwidth. The time domain response of this filter is referred to as the resolution kernel. The filter was of the form

$$F(f) = \frac{1}{1 + \frac{\theta}{|H(f)|^2}} \frac{1}{1 + \exp(-2\pi(f-f_C)t^*)}$$

where  $H(f)$  is the complex response of the LRSM instrument,  $\theta$  is a chosen signal-to-noise level and  $f_C$  is a high frequency cut-off. The filter is nearly flat for frequencies below  $f_C$  and for the bandwidth of frequencies for which  $|H(f)|^2 > \theta$ . The filter serves to limit the deconvolution of the high and low frequencies where signal-to-noise ratio is poor. Typical values of  $f_C$  were 4.0 Hz for low  $t^*$  stations like RK-ON and 3.0 Hz for high  $t^*$  stations such as WO-AZ or KN-UT.

As with the EKA and YKA data, the P wave signal moment was estimated from the time domain deconvolved pulses and used to estimate the explosion moment,  $M_0$ . The results in Table 6 are in good agreement with the spectral estimates of moment presented in Table 3. The summary statistics are given in Table 7 for the LRSM temporal moment estimates together with the EKA and YKA estimates. The principal difference between these LRSM deconvolutions and the deconvolutions of Shumway and Der (1985) which we applied to the EKA and YKA data is that the multichannel deconvolution estimates the local station site responses. The LRSM deconvolutions have not had estimates of the local station site response removed. The deconvolutions shown in Figures 6A and 6B are bandlimited estimates of the explosion source convolved with any propagation complexities and therefore only those characteristics



that are similar across the network may be reliably attributed to the source.

TABLE 6.

RUBIS AND SAPHIR LRSM TEMPORAL MOMENT ESTIMATES								
STATION	$\Delta$ deg	$\bar{r}^*$ s	$\Omega_0$ nm-s	$\rho$ gm/cc	$\alpha$ km/s	$\beta$ km/s	$M_0$ dyne-cm	$\Psi_\infty$ m <sup>3</sup>
RUBIS								
BL-WV	72.6	0.35	71.	2.7	6.0	3.46	5.26E+22	4700
DH-NY	66.7	0.45	88.	2.7	6.0	3.46	6.34E+22	5772
EB-MT	78.1	0.65	204.	2.6	5.8	3.3	1.61E+23	14643
EU-AL	79.4	0.45	185.	1.9	2.7	1.4	8.74E+22	7950
FR-MA	86.3	0.55	160.	2.6	5.8	3.3	1.26E+23	12346
GI-MA	84.4	0.45	88.	2.6	5.8	3.3	7.34E+22	6681
HL-ID	92.2	0.50	66.	2.5	5.2	2.96	1.13E+23	10300
HN-ME	61.2	0.50	92.	2.7	5.9	3.36	5.79E+22	5275
KN-UT	95.3	0.70	30.	2.0	3.15	1.81	4.01E+22	3649
LC-NM	93.6	0.60	63.	2.2	3.0	1.6	8.59E+22	7819
RK-ON	76.6	0.35	92	2.7	5.64	3.47	7.17E+22	6517
SAPHIR								
BL-WV	72.6	0.35	202.	2.7	6.0	3.46	1.50E+23	13653
BR-PA	70.2	0.50	225.	2.7	6.0	3.46	1.69E+23	15391
HN-ME	61.2	0.50	240.	2.7	5.9	3.36	1.51E+23	13761
HN-ME	61.2	0.50	(511.)	2.7	5.9	3.36	(3.23E+23)	(29300)
KN-UT	95.3	0.70	47.	2.0	3.15	1.81	6.28E+22	5717
LC-NM	93.6	0.60	170.	2.2	3.0	1.6	2.32E+23	21100
RT-NM	89.8	0.70	286.	2.6	5.8	3.3	5.78E+23	52554
RY-ND	82.4	0.60	334.	2.6	5.8	3.3	2.74E+23	24936
VO-IO	78.9	0.50	241.2	2.6	5.8	3.3	1.90E+23	17324
WO-AZ	95.1	0.80	412.	2.6	5.8	3.3	8.44E+23	76757

TABLE 7.

TEMPORAL MOMENT ESTIMATES 10 <sup>24</sup> dyne-cm				
EVENT	MEAN	RMS	GEOMETRIC MEAN	MEDIAN
RUBIS	0.081(0.01)	0.089	0.073	0.073
SAPHIR	0.25(0.07)	0.34	0.16	0.17

The temporal estimates are statistically better (smaller dispersion) than the spectral estimates and the ratio of the size of the two events is closer to the ratio of the yields as given by

Marshall *et al.* (1979). The average log-ratio of RUBIS to SAPHIR at the five sites, BL-WV, HN-ME, KN-UT, LC-NM, and EKA is -0.34. This is in excellent agreement with the log-ratio of the yields. If we assume that the moment of SAPHIR is 2.3 times the moment of RUBIS then we arrive at the summary statistics of Table 8.

TABLE 8.

TEMPORAL MOMENT ESTIMATES $10^{24}$ dyne-cm -CONSTRAINED-				
EVENT	MEAN	RMS	GEOMETRIC MEAN	MEDIAN
RUBIS	0.094(0.02)	0.12	0.072	0.073
SAPHIR	0.22(0.04)	0.28	0.17	0.17

The deconvolved waveforms are shown in Figures 6A and 6B. The waveforms are shown in order of decreasing azimuth from the source. Several interesting features in the later arrivals can be correlated between stations and are probably due to near source scattering. The RUBIS records at HL-ID and FR-MA show a positive late pulse (labeled "A") that is remarkably similar between the two stations. A similar late secondary phase can be seen on other station records (labeled "(A)"). The RUBIS records at KN-UT, HN-ME, and LC-NM are also similar in appearance (azimuths of 315, 311, and 308 degrees, respectively). These similarities are probably not due to common station effects and therefore, may be attributed to near source complexity.

SAPHIR at HN-ME shows a broad P pulse and therefore a large time domain moment estimate in contrast to the spectral estimate (in parentheses in TABLE 6). A better estimate at HN-ME may be to ignore this broadening since the initial P wave is simple at all the other stations. This may be due to a secondary arrival prolonging the SAPHIR P-wave pulse at HN-ME. Since this is isolated to HN-ME it may be a station effect, although the RUBIS record may not show the same feature.

## DISCUSSION

It is of interest to compare these teleseismic RDP values with free-field measurements of RDP for the three US granite explosions, PILEDRIVER, SHOAL, and HARDHAT. Werth and Herbst (1963) present data for HARDHAT (5KT,  $\rho=2.69\text{gm/cc}$ ,  $\alpha=4.8\text{km/s}$ ,  $h=286\text{m}$ ) with peak values of RDP near  $4700\text{ m}^3$  and a static level of about  $2500\text{ m}^3$ . Murphy (1978) presents data for PILEDRIVER (62KT,  $\rho=2.67\text{gm/cc}$ ,  $\alpha=5.8\text{km/s}$ ,  $\beta=3.45\text{km/s}$ ,  $h=457\text{m}$ ) with peak levels of 30000 to 50000  $\text{m}^3$  and static levels of about 20000  $\text{m}^3$ , for SHOAL (13KT,  $\rho=2.55\text{gm/cc}$ ,  $\alpha=5.5\text{km/s}$ ,  $\beta=3.0\text{km/s}$ ,  $h=367\text{m}$ ) with peak RDP levels of 7000  $\text{m}^3$  and static levels of about 4000  $\text{m}^3$ , and for HARDHAT (5.9KT,  $\rho=2.67\text{gm/cc}$ ,  $\alpha=5.5\text{km/s}$ ,  $\beta=3.25\text{km/s}$ ,  $h=290\text{m}$ ) with peak RDP levels of 3000 to 5000  $\text{m}^3$  and static levels of about 2300  $\text{m}^3$ .

The static PILEDRIVER moment of  $0.22 \cdot 10^{24}$  dyne-cm (Murphy, 1978) when scaled to the RUBIS yield is  $0.18 \cdot 10^{24}$  dyne-cm. This is 1.5 times the RUBIS rms moment estimate of Table 8. The discrepancy is significantly larger if the mean or geometric mean of the RUBIS moment is used for comparison, or if the peak PILEDRIVER RDP levels are used for comparison. Comparison of the teleseismic moment estimates with the scaled free-field RDP levels from SHOAL or HARDHAT give much the same result. The French Sahara teleseismic rms moment estimates are between 30 and 50% too low when compared to the measured free-field RDP levels of US granite explosions. The measured free-field granite RDP levels are roughly consistent with each other, while Heuze (1983) and Schock *et al* (1972) find no significant difference between the granites of Climax Stock, NTS, and Taourirt Tam Afella Massif, Algeria. However, the free-field RDP levels are clearly inconsistent with the teleseismic observations of the equivalent moments for RUBIS and SAPHIR unless additional attenuation is introduced into either the near-field or along the teleseismic path.

Several hypotheses may be presented to explain the discrepancy between the two data sets. First of all, the free-field RDP data were all collected within the non-linear zone of ground motion and may over estimate the far-field equivalent explosion moment. Only attenuation measurements at high strain rates in granite, can directly test this hypothesis. Some additional broadband attenuation is introduced by reflections and conversions at crustal and mantle interfaces, but it is unlikely that this amounts to between 30 and 50% broadband reduction in amplitude. Similarly, McLaughlin and Anderson (1984) suggest that crustal scattering may contribute to pulse attenuation but may not be detectable by spectral  $\bar{t}^*$  measurements. However, their evidence suggests that the mechanism is not significant at frequencies below 1 Hz. Finally, if  $f \frac{dt^*}{df} \approx -0.2$  sec in the 0.5 to 2 Hz bandwidth, then the teleseismic moment estimates presented are too low and a factor of 2 correction would be consistent with the static free-field granite RDP measurements made for PILEDRIIVER, SHOAL, and HARDHAT. Several such frequency dependent  $t^*(f)$  models have been proposed (Der *et al.*, 1982; Bache *et al.*, 1985; Taylor *et al.*, 1986; Choy and Cormier, 1986; and Der *et al.*, 1986).

## CONCLUSIONS

We have estimated the far-field equivalent seismic sources for four French Sahara explosions contained in granite from short period seismic recordings, using two time domain deconvolution methods and one spectral estimation method. Uncertainties in source size are largely due to the uncertainties in the frequency dependence of  $Q$  in the mantle, and the amplitude fluctuations due to focusing-defocusing along the teleseismic path. The uncertainties in  $t^*(f)$  near 1 Hz are systematic errors while the focusing-defocusing errors are more likely random in nature. The most serious of these two errors is probably the uncertainty in the value of  $\frac{dt^*}{df}$

near 1 Hz. A value of  $\frac{dt^*}{df}$  of about -0.2 sec/Hz at 1 Hz would roughly double the moment estimates. The focusing-defocusing introduces random error into the network but may be overcome by the averaging over many stations. Focusing-defocusing patterns can be discerned and corrected from  $m_b$  measurements from WWSSN stations or the ISC reported magnitudes.

P wave teleseismic  $\bar{t}^*$  estimates for the test site are in agreement with classification of the Ahaggar region as a "hot spot". The values of  $\bar{t}^*$  estimated from LRSM, EKA, and YKA data are in agreement with the Der *et al.* (1985b) estimate of 0.35 sec but favor a slightly lower value near 0.31 sec. The Der *et al.* (1985b)  $\bar{t}^*$  estimate for NTS is 0.34 sec, therefore there is no evidence for significant attenuation bias between Ahaggar and NTS.

The deconvolution technique of Shumway and Der (1985) has been shown to yield explosion size,  $M_0$  or  $\Psi_\infty$  values, consistent with spectral estimates. SAPHIR recorded at YKA may show evidence of destructive interference of pP due to topographic effects.

Deconvolutions of the LRSM records reveal similar variability of the radiated P waveforms from SAPHIR and RUBIS. Particularly interesting are the late arrivals correlated between stations some distance apart but of similar takeoff angle. The topography at the French southern Sahara test site could be responsible for these large variations.

Comparison of the various methods used in this work reveals that the spectral and deconvolution methods make consistent estimates of explosion size. While the spectral slope and intercept method may be used to estimate the  $\bar{t}^*$  and  $\Omega_0$  for the pulse, the method relies on a rough estimate of the source spectral shape. The deconvolution methods do not assume anything about the source time function but require an estimate of the attenuation parameters. Therefore it is not surprising that the deconvolution methods that use the spectral  $\bar{t}^*$  estimates give results consistent with the low frequency spectral intercept method. However, the deconvolutions reveal a great deal of complexity in the early P-wave coda while the initial P wave

remains very simple. Spectral methods average the P waveform and may be susceptible to the interference of positive and negative polarity pulses to decrease the low frequency level of the P waveform. The presence of these interfering negative and positive pulses can then be sorted out using the deconvolution methods. By this token the time domain moment estimates are the better estimates and justify the extra computation and care that must be made in deconvolution of bandlimited signals.

### ACKNOWLEDGEMENTS

This work was supported by the Defense Advanced Research Projects Agency and monitored by the Air Force Geophysics Laboratory under contract F19628-85C-0035. The views and conclusions contained in this report are those of the authors and should not be interpreted as necessarily representing the official policies, either expressed or implied, of the Defense Advanced Research Projects Agency or the U.S. Government. KLM would like to thank R.-S. Jih, T. W. McElfresh and R. Wagner for their programming efforts and calculations, and Alan Douglas for a stimulating conversation on explosion source estimation.

## REFERENCES

- Aki, K. and P. G. Richards (1980), *Quantitative Seismology Theory and Methods, Vol. I.*, Freeman.
- Azimi, S. A., A. V. Kalinin, V. V. Kalinin, and B. L. Pivovarov (1968), Impulse and transient characteristics of media with linear and geometric absorption laws, *Izvestiya, Physics of the Earth*, 88-93.
- Choy, G. L., V. F. Cormier (1986), Direct measurement of the mantle attenuation operator from broadband P and S waveforms, *J. Geophys. Res.*, 91, 7326-7342.
- Crough, S. T., (1981), Free-air gravity over the Hoggar massif, northwest Africa: evidence for alteration of the lithosphere, *Tectonophysics*, 77, 189-202.
- Der, Z. A., T. W. McElfresh, and C. P. Mrazek (1977), The effect of crustal structure on station magnitude anomalies (magnitude bias), SDAC-TR-77-1, Teledyne Geotech, Alexandria, Va.
- Der, Z. A., E. Smart, A. H. Chaplin (1978), Short period S wave attenuation under the United States, SDAC-TR-78-6, Teledyne Geotech, Alexandria, Va.
- Der, Z. A., T. W. McElfresh, and A. O'Donnell (1982), An investigation of the regional variations and frequency dependence of anelastic attenuation in the mantle under the United States in the 0.5-4 Hz band, *Geophys. J. R. astr. Soc.* 69, 67-100.
- Der, Z.A. T. W. McElfresh, R. Wagner, and J. Burnetti (1985a) Spectral Characteristics of P Waves from Nuclear Explosions and Yield Estimation, *Bull. Seism. Soc. Am.*, 75, 379-390.
- Der, Z.A. T. W. McElfresh, R. Wagner, and J. Burnetti (1985b) ERRATA: Spectral Characteristics of P Waves from Nuclear Explosions and Yield Estimation, *Bull. Seism. Soc. Am.*, 75, 1222.
- Der, Z. A. and A. C. Lees (1985), Methodologies for estimating  $t^*(f)$  from short-period body waves and regional variations of  $t^*(f)$  in the United States, *Geophys. J. R. astr. Soc.*, 82, 125-140.
- Der, Z. A., A. C. Lees, and V. F. Cormier (1986), Frequency dependence of Q in the mantle underlying the shield areas of Eurasia, Part III, The Q model, *Geophys. J. R. astr. Soc. (in press)*.
- Douglas, A., P. D. Marshall, and J. B. Young (1985), The P waves from the Amchitka Island explosions, (submitted for publication).
- Duclaux, F. and M. L. Michaud (1970), Conditions experimentales des tirs nucleaires souterrains francais au Sahara, R. Acad. Sc. Paris, t. 270 (12 Janvier 1970) Serie B 189-192.

Faure, J. (1972) Recherches sur les effets geologiques d'explosions nucleaires southeraines dans un massif de granite saharien, Centre d'Etudes de Bruyeres-le-Chatel, Commissariat a l'Energie Atomic Report CEA-R-4257 Service de Documentation CEN-SACLAY B.P. no. 2, 91-GIF-sur-Yvette, France.

Heuze, F. E. (1983), A review of geomechanics data from French nuclear explosions in the Hoggar granite, with some comparisons to tests in U. S. granite. *Lawrence Livermore Laboratory Report, UCID-19812, May 1983.*

Marshall, P. D., D. L. Springer, and H. C. Rodean (1979), Magnitude corrections for attenuation in the upper mantle, *Geophys. J. R. astr. Soc.* 57, 609-638.

McLaughlin, K. L. and L. M. Anderson (1984), Stochastic dispersion of seismic P waves due to scattering and multipathing, *Semi-Annual Tech. Report., TGAL-84-5*, Teledyne Geotech, Alexandria, Va.

McLaughlin, K. L. (1986), Network magnitude variation and magnitude bias, *Bull. Seism. Soc. Am.*, 76, 1813-1816.

Murphy, J. R. (1978), A review of available free-field seismic data from underground nuclear explosions in salt and granite, *Computer Sciences Corporation, CSC-TR-78-0003*, Falls Church, Va.

Schock, R. N., A. E. Abey, H. C. Heard, and H. Louis (1972), Mechanical properties of granite from the Taourirt Tan Afella Massif, Algeria, *Lawrence Livermore Laboratory Report, UCRL-51296, November 1972.*

Shumway, R. H. and Z. A. Der (1985), Deconvolution of multiple time series, *Technometrics*, 27, 385-393.

Taylor, S. R., B. R. Bonner, and G. Zandt (1986), Attenuation and scattering of broadband P and S waves across North America, *J. Geophys. Res.*, 91, 7309-7325.

von Seggern, D. H. and R. R. Blandford (1972), Source time functions and spectra for underground explosions, *Geophys. J. R. astr. Soc.*, 31, 83-87.

Werth, G. C. and R. F. Herbst (1963), Comparison of amplitudes of seismic waves from four explosions in four mediums, *J. Geophys. Res.*, 68, 1463-1475.



## FIGURE CAPTIONS

FIGURE 1. Locations of LRSM stations, the EKA, and YKA arrays centered on the southern Algerian test site. The two arrays, EKA (Eskdalemuir, Scotland, U.K.) and YKA (Yellowknife, Northwest Territories, Canada) are indicated with solid symbols.

FIGURE 2. Contour map of Taourirt Tan Afella from Faure (1972) and locations for several events from Duclaux and Michaud (1970) are indicated. The contours are at 100 meter intervals and the dotted line shows the granite outcrop. The elevation of the plateau around the mountain is about 1100 meters. Locations for SAPHIR (S), RUBIS (R), EMERAUDE (Em), and GRENAT (G) are indicated. The azimuths to several stations are shown above with labeled arrows.

FIGURE 3. Spectra corrected for instrument and RDP. Slopes between 0.5 and 3.0 Hz are estimates of  $t^*$ , intercepts are estimates of  $\Omega_0$ . Only spectral levels with an estimated signal-to-noise power ratio greater than 2 were used.

FIGURE 4. Deconvolved source time functions at the EKA and YKA arrays for SAPHIR, RUBIS, GRENAT and EMERAUDE. RUBIS was poorly recorded across YKA.

FIGURE 5A. Equivalent seismic sources,  $\dot{M}(t)$  for SAPHIR, RUBIS, GRENAT and EMERAUDE at the EKA array. The explosion moment inferred from the P-pulse area is indicated.

FIGURE 5B. Equivalent seismic sources,  $M(t)$ , for SAPHIR, RUBIS, GRENAT and EMERAUDE at the YKA array. The explosion moment inferred from the P-pulse area is indicated.

FIGURE 5C. Equivalent seismic sources,  $\dot{M}(t)$ , for SAPHIR, RUBIS, GRENAT and EMERAUDE at the EKA array. The explosion moment inferred from the P-pulse area is indicated.

FIGURE 5D. Equivalent seismic sources,  $M(t)$ , for SAPHIR, RUBIS, GRENAT and EMERAUDE at the YKA array. The explosion moment inferred from the P-pulse area is indicated.

FIGURE 6A. Deconvolved waveforms for RUBIS at LRSM stations. The causal P-wave pulse area is indicated for each trace. Traces are ordered in decreasing azimuth from the top. Late positive arrivals that may be correlated between stations are indicated by labels "A" and "(A)".

FIGURE 6B. Deconvolved waveforms for SAPHIR at LRSM stations. The causal P-wave pulse area is indicated for each trace. Traces are ordered in decreasing azimuth from the top. The HN-ME waveform shows considerable broadening that may be due to a positive secondary arrival unique to the HN-ME station.



Figure 1.

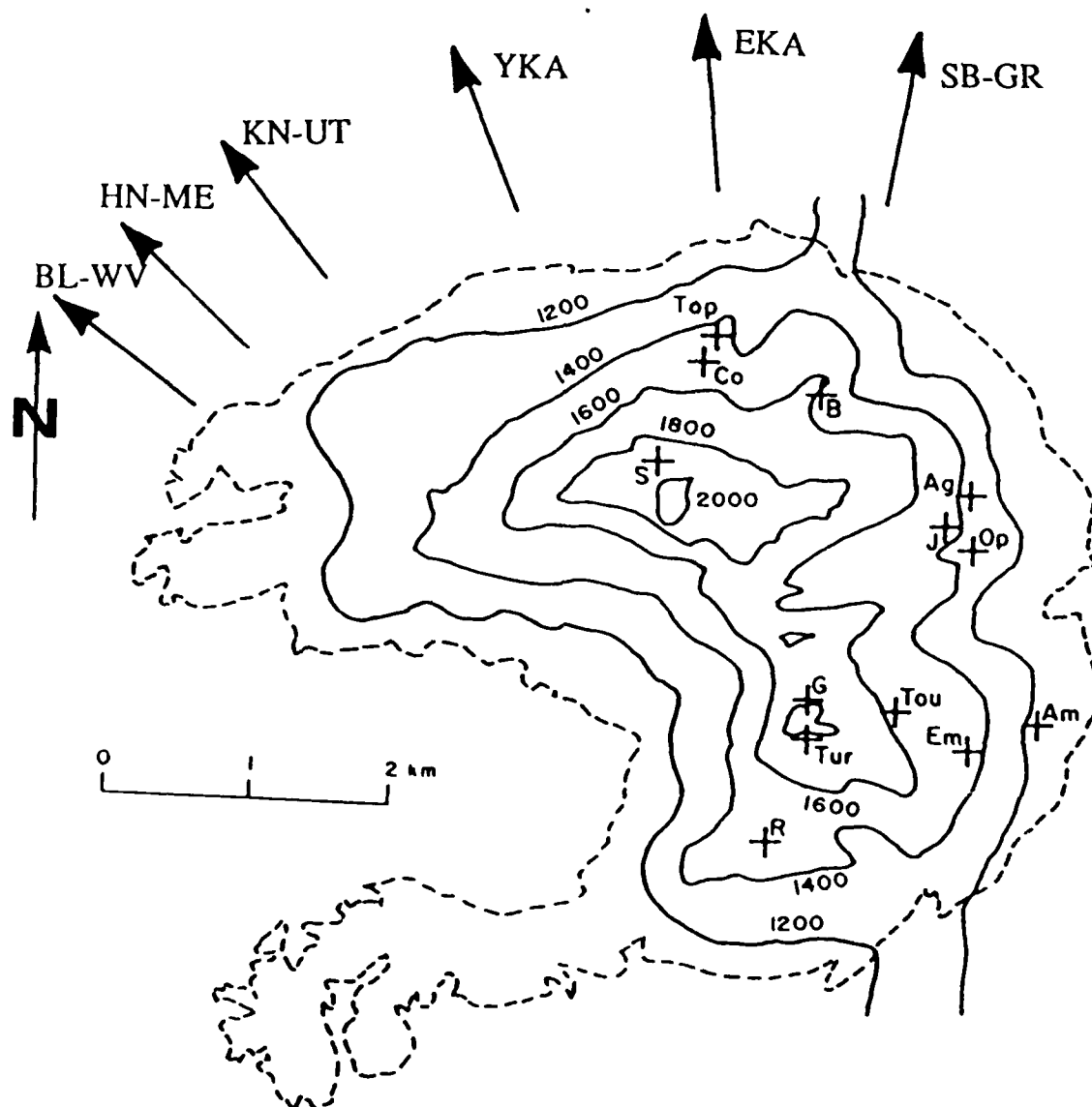


Figure 2.

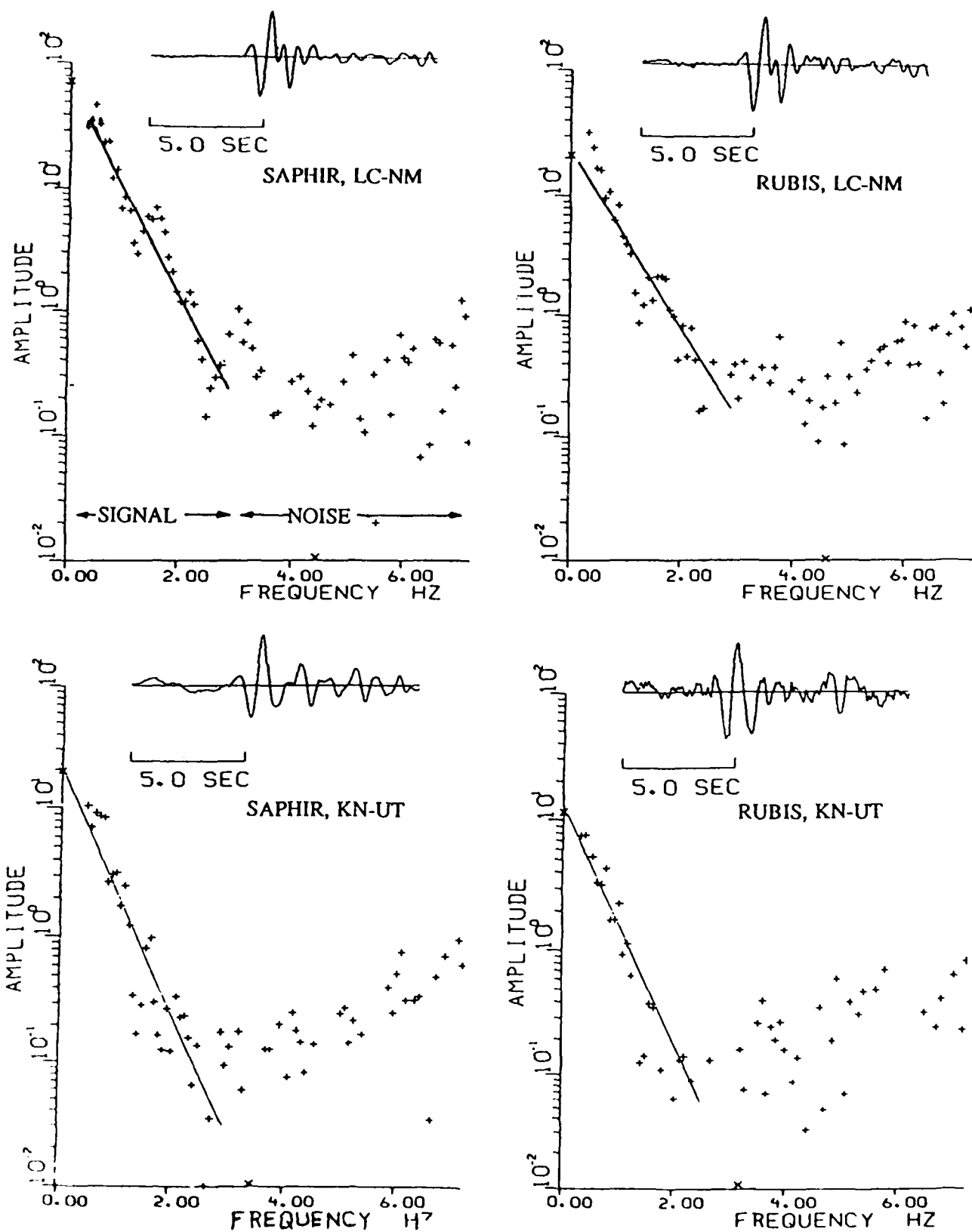


Figure 3A.

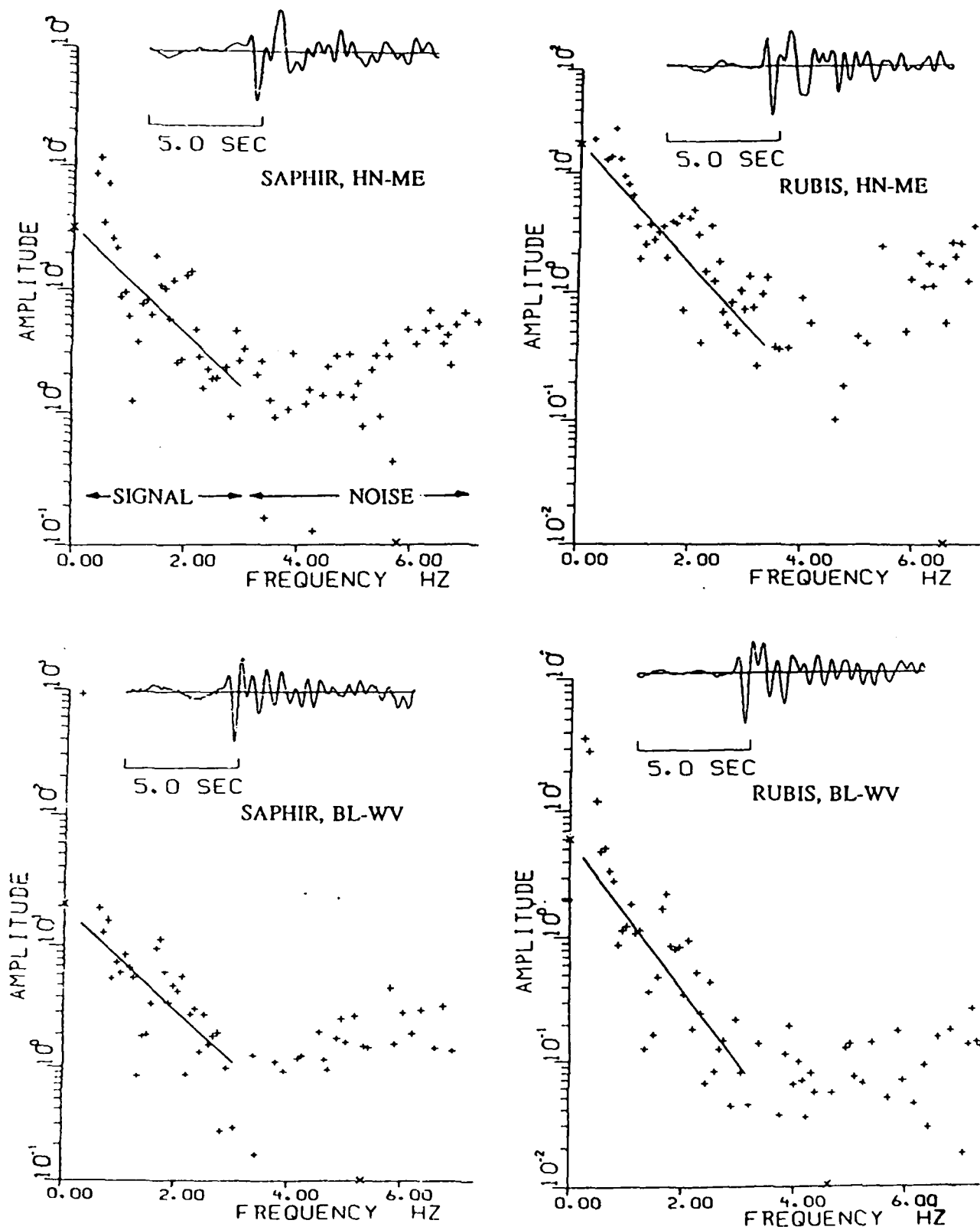


Figure 3B.

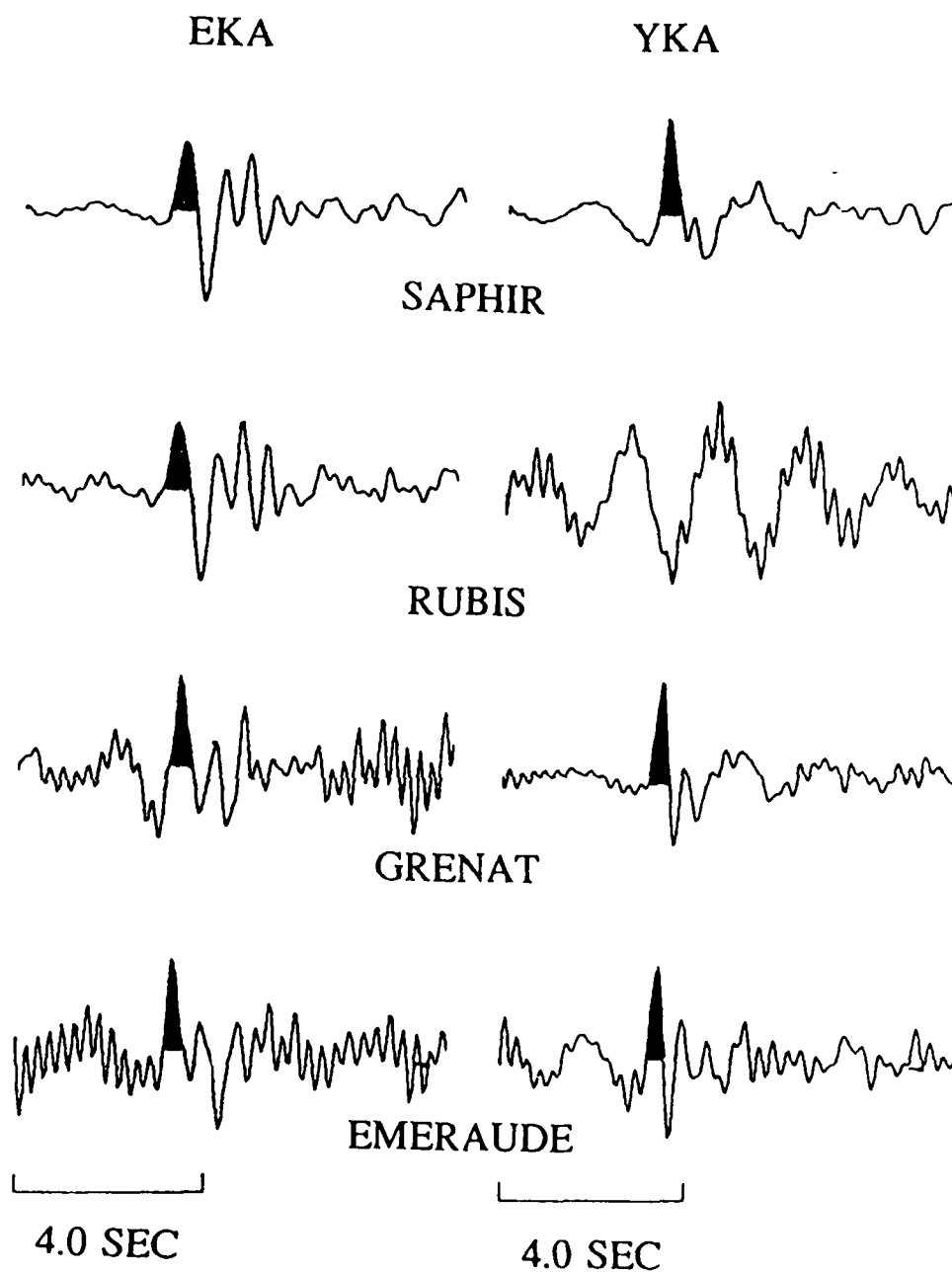


Figure 4.

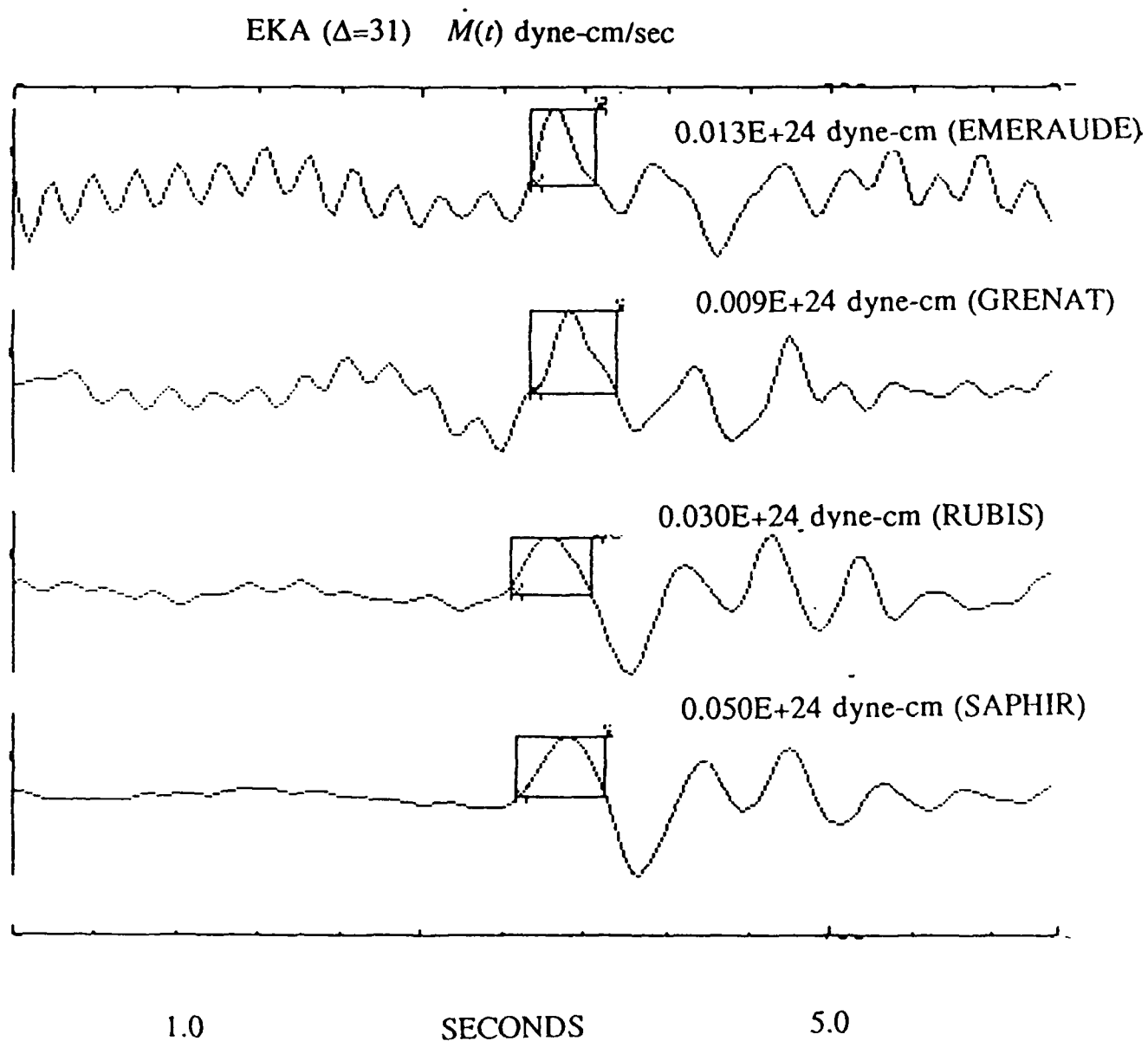


Figure 5A.

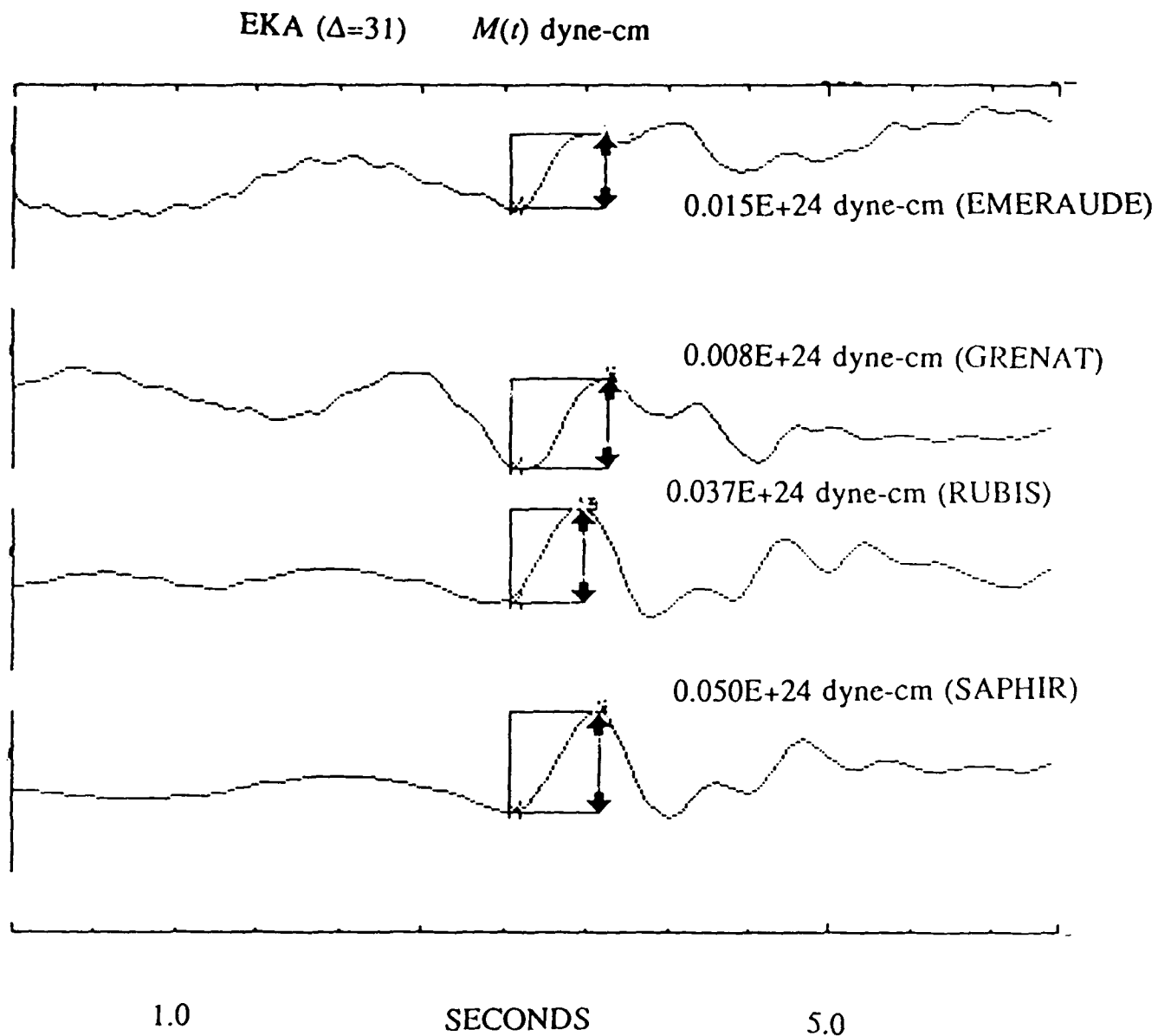


Figure 5B.



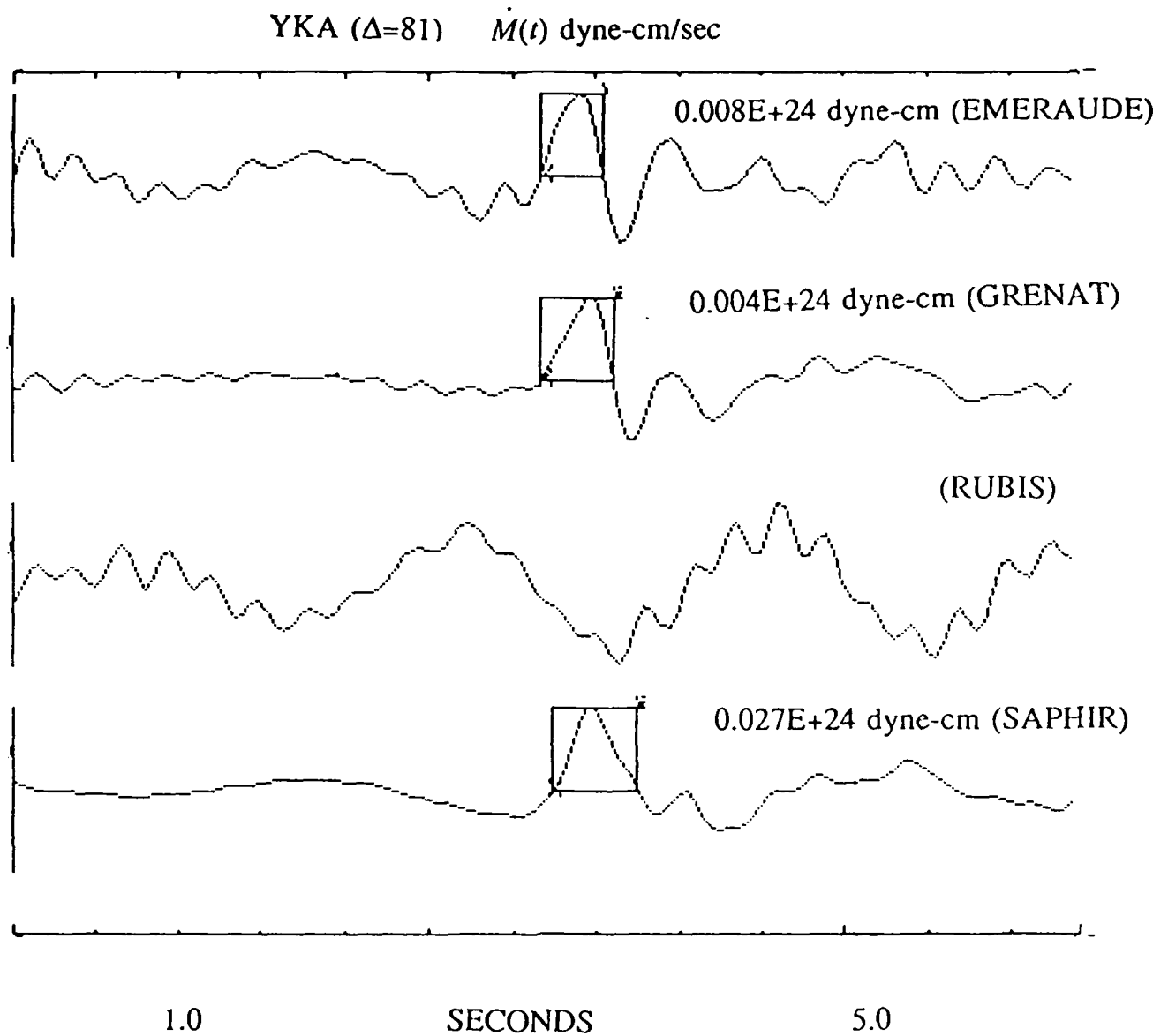


Figure 5C.

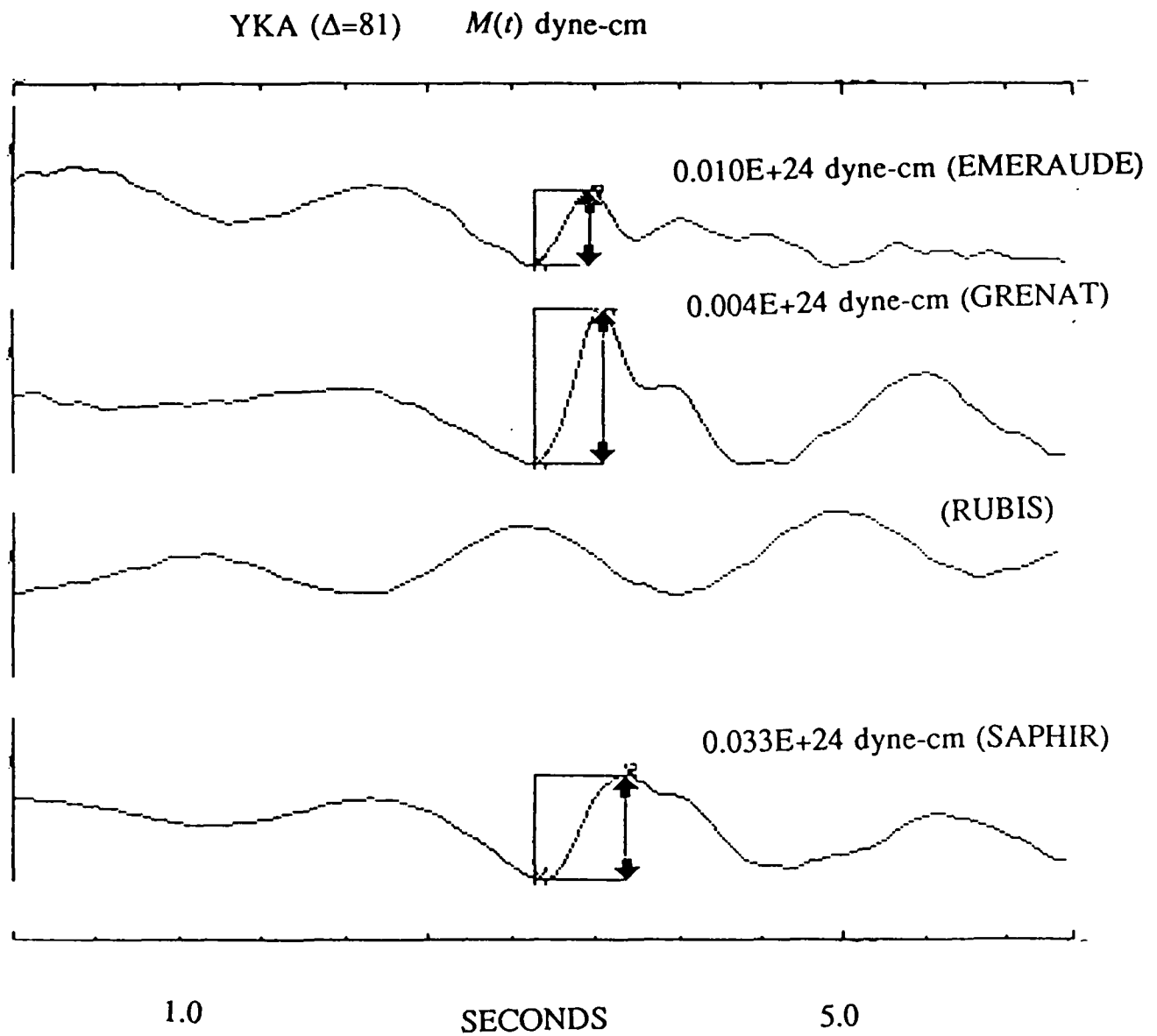


Figure 5D.

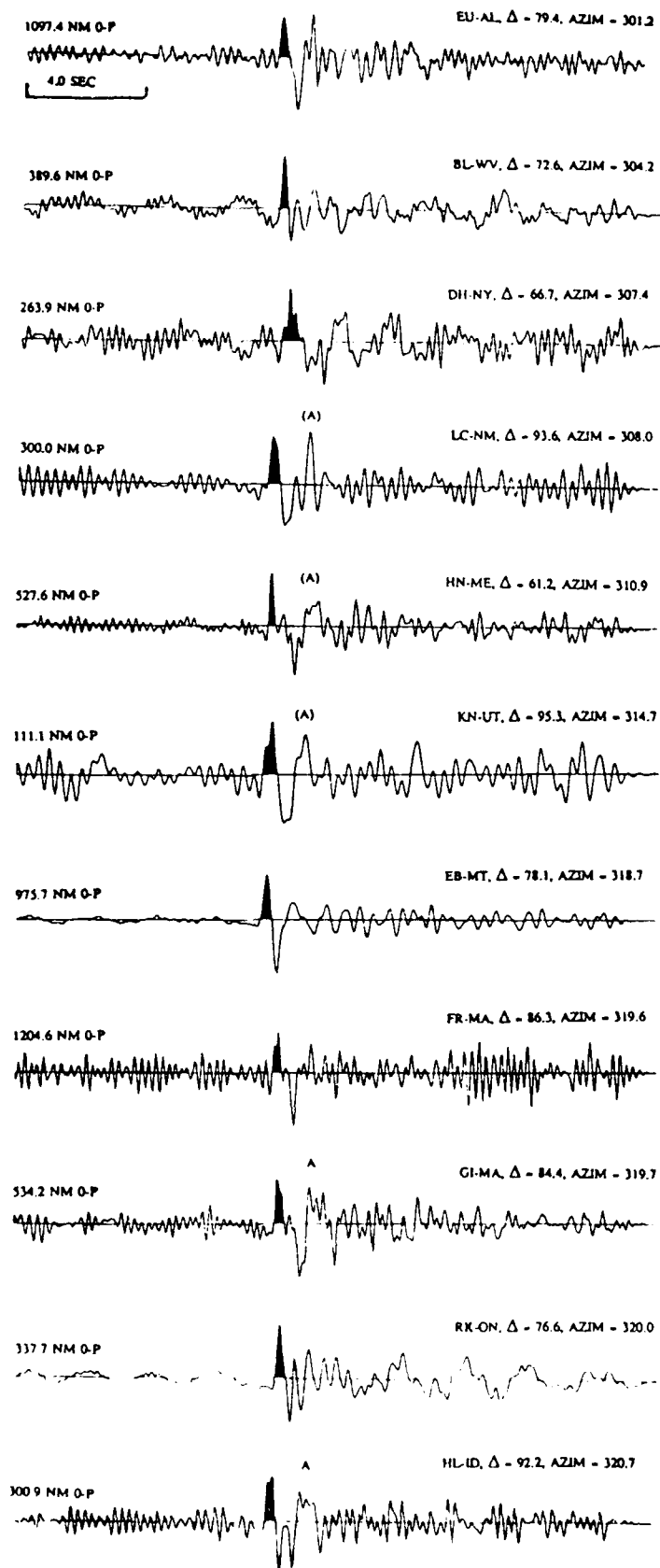


Figure 6A.

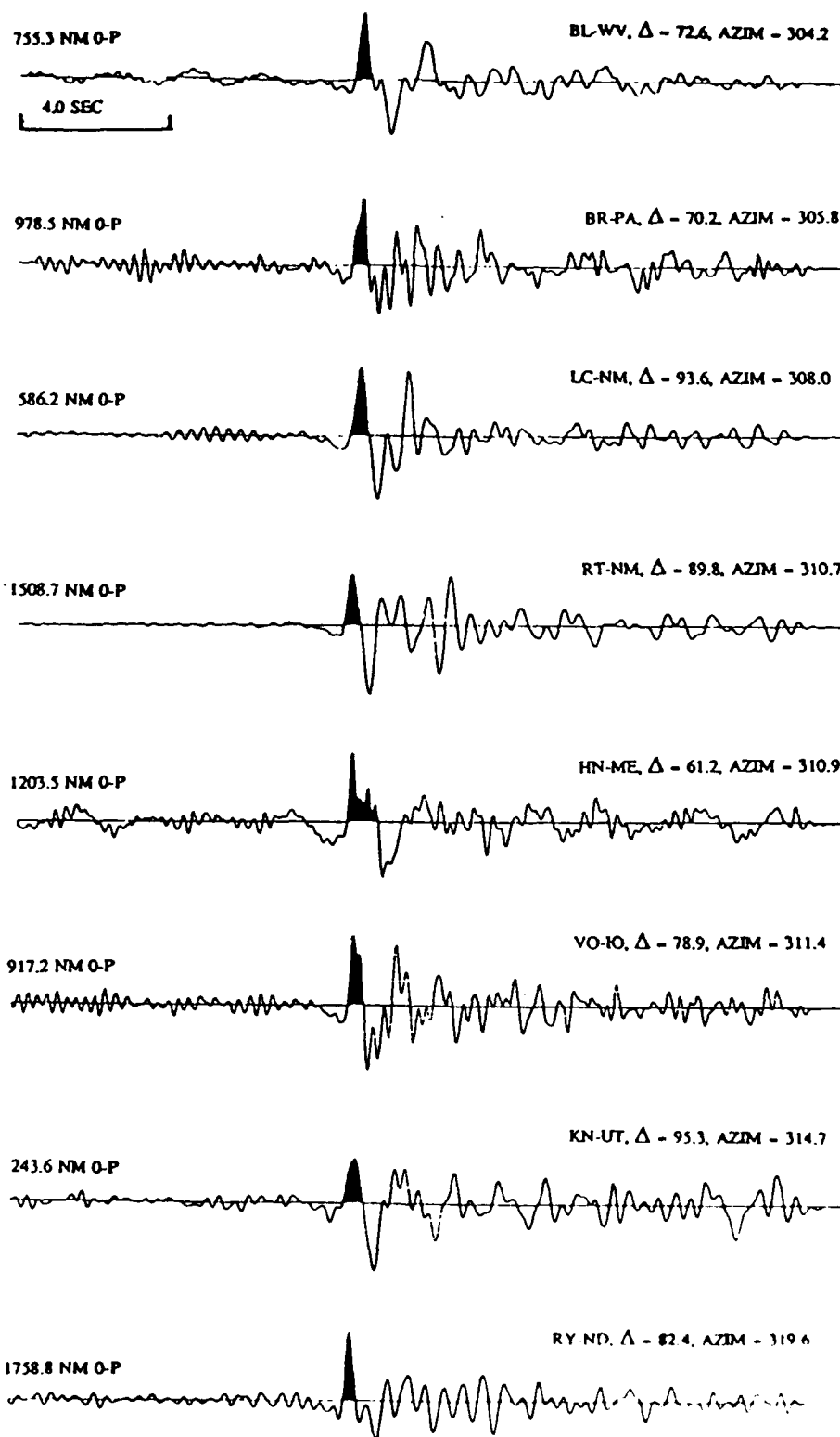


Figure 8B

## SECTION 3

SCATTERING FROM NEAR-SOURCE TOPOGRAPHY:  
TELESEISMIC OBSERVATIONS AND  
NUMERICAL 2-D EXPLOSIVE LINE SOURCE SIMULATIONS

K. L. McLaughlin, and R.-S. Jih  
Teledyne Geotech Alexandria Laboratories  
314 Montgomery Street  
Alexandria, VA 22314

## INTRODUCTION

Jih et al (1986) propose methods for introduction of free surface topography in heterogeneous elastodynamic two dimensional (2-D) linear finite difference (LFD) calculations. We have applied these methods to explosive line sources for simulation of far-field "teleseismic" P waves. The motivation for these numerical experiments is to examine the extent of scattering from near-source topography on short-period seismograms used for explosion yield estimation. Several important test sites have substantial topography within a few (1 Hz P wave) wavelengths of the source. These test sites include the French southern Sahara test site, the Novaya Zemlya test site (Greenfield, 1971), and the Degelen, Eastern Kazakh test site (Rodean, 1979).

To explore the variability that may be introduced by near-source topography, several simple test cases have been investigated. These test cases indicate that the presence of topography of the far-field teleseismic P waves is not significant. The results of the numerical experiments indicate that the presence of topography near the source is significant. The results of the numerical experiments indicate that the presence of topography near the source is significant. The results of the numerical experiments indicate that the presence of topography near the source is significant.

As a worst case, the southern Algeria test site located within Taourirt Tan Afella Massif will serve as a model for some more specific calculations. This granite mountain rises from the (1100 meter elevation) Ahaggar plateau to a peak of 2100 meters in less than 1 km. The mountain is only 16 km<sup>2</sup> and has slopes that locally exceed 45°. Several tests were conducted at this site in southern Algeria from 1962 to 1966. A topographic map from Duclaux and Michaud (1970) is shown in Figure 1, with locations from Faure (1972) (see Table 1). Contours are at 100 meter intervals and the granite outcrop is indicated by the dashed line. In recent years Blandford and Shumway (1982), Blandford et al (1984) and McLaughlin et al (1986a) have conducted investigations of the  $m_b$  observed from these explosions at WWSSN stations. Furthermore, available Long Range Seismic Measurements (LRSM) data and the Eskdalemuir, Scotland (EKA) and Yellow Knife, Northwest Territories (YKA) arrays have been analyzed (see McLaughlin et al 1986b) for estimates of the explosion spectra, moments, and source time functions.

TABLE 1. EVENT DATA FROM FAURE (1972)				
DATE	ORIGIN TIME	LAT (N)	LONG (E)	EVENT
1963/03/18	10:02:00.351	24.0414	5.0522	EMERAUDE
1963/10/20	13:00:00.011	24.0355	5.0386	RUBIS
1965/02/27	11:30:00.039	24.0587	5.0312	SAPHIR
1965/12/01	10:30:00.088	24.0437	5.0469	TOURMALINE
1966/02/16	11:00:00.035	24.0442	5.0412	GRENAT

### AN EXAMPLE TOPOGRAPHIC CALCULATION

Figure 2A shows a simple topographic profile. The elastic medium has a P-wave velocity of 5 km/s, and the line source locations are indicated by triangles in the Figure. The calculations are performed by use of reciprocity. A broadband plane wave (source at infinity) is incident upon the model and the dilatation time history is measured at a location within the

grid. By reciprocity, this time history is the far-field broadband displacement pulse at infinity for a broadband dilatational source within the model. We may simulate any far-field seismogram by the removal of the known bandlimited incident P-wave pulse, and convolution of a teleseismic transfer function that includes attenuation, receiver crustal structure, instrument response, and model source time function (c.f. Robinson, 1983). A single run with an incident planar P wave then yields the teleseismic response for a suite of source locations within the model. A run must be performed for each takeoff angle (teleseismic slowness) desired by introduction of a planar P wave with the desired incidence angle.

Figure 3 shows teleseismic synthetic seismograms for the the topographic profile in Figure 2A for a takeoff angle of  $0^\circ$ . The synthetic has been convolved with a von Seggern and Blandford (1972) granite explosion source time function (100 KT), an attenuation operator ( $t^* = 0.45$  sec), and an LRSM instrument response. All of the seismograms are plotted at the same scale and show the variability of the P-waveforms due to the constructive and destructive interference of the linear reflection from the surface. The "bc" phase of the P wave shows the greatest variability due to the elastic P+pP interference. The log-amplitudes of the P wave "a", "ab", and "max" phases in Figure 3 are plotted in Figure 2B. The log(a) variation is slight as expected while the log(ab) and log(max) variations reflect considerable variation in the linear elastic P+pP interference.

### TAOURIRT TAN AFELLA MASSIF

A north-to-south cross section of Taourirt Tan Afella Massif (P wave velocity of 5.2 km/s) is shown in Figure 4A with a  $15^\circ$  incident planar P wave. A planar, band-limited P wave is incident upon the medium from below and the dilatational strain is measured at the source locations. The far-field displacement P waveform due to an explosion line source at

these locations is then inferred from this transfer function by reciprocity. Figures 4B through 4E illustrate the dilatational field at intervals of 0.2 second as the P wave reflects from the free surface. Note that at time interval 0.4 second, the strong constructive and destructive interference that results from the reflections directly beneath the peaks of the ridge (2-D mountain). The linear pP contribution from this location would be large and variable for a receivers at a takeoff angles near  $15^\circ$ . At time intervals 0.6 and 0.8 seconds we see what appear to be Rayleigh waves trapped at the surface as well as dilatational coda behind the specularly reflected P wave.

Source locations indicated by triangles in Figure 4A were used to infer far-field P waveforms from 2-D explosive line sources shown in Figure 5A and 5B. The waveforms have been convolved with von Seggern and Blandford (1972) explosive source time functions (50 and 120 KT), an attenuation operator ( $t^* = 0.45$  sec), and an LRSM instrument response. Waveforms are shown for takeoff angles of 0, 5, 10, 15, and 20 degrees. These two source locations are labeled "RUBIS" and "SAPHIR" analogous to the two locations (R and S) of Figure 1. Several interesting features are evident in these 2-D numerical simulations.

For the location "SAPHIR", the maximum amplitude decreases with increasing takeoff angle (see Figure 5A). The elastic pP contribution increases in such a way as to reduce the "b-c" amplitude with increasing takeoff angle. The coda amplitude increases with increasing takeoff angle as the free-surface interaction becomes more complicated and the conversions of P-SV energy increase at the free surface. The "SAPHIR" location is roughly coincident with the focal point of the topographic profile and the pP reflection may be amplified at this source location for some narrow range of takeoff angles.

The "RUBIS" location also shows an increase of coda amplitude with increasing takeoff angle (See Figure 5B). For the shallowest takeoff angle of  $20^\circ$ , there is a secondary arrival



larger than the main P wave. The "RUBIS" "b-c" amplitude does not show as strong a variation with takeoff angle. The topography directly above the "RUBIS" location is less steep and the pP free surface interaction is only distorted. However, the topography to the north of the "RUBIS" location introduces scattered arrivals responsible for the strong coda. The "RUBIS" location is above the "focal point" of the topographic profile and the pP reflection may be defocused at this source location.

Spectral ratios of the "RUBIS"-to-"SAPHIR" 2-D synthetics showed that as the takeoff angle increases, "RUBIS" becomes enriched in high frequencies with respect to "SAPHIR". The modulation of the spectra makes this comparison difficult if the bandwidth is limited as it is in real data to frequencies below 4.0 Hz. However, the spectral ratio of the two events at a common station may give clues as to which event received the largest contribution of scattered energy in the coda due to the topography above the source.

YKA, EKA, KN-UT, HN-ME, BL-WV, and LC-NM recorded both RUBIS and SAPHIR. The spectral ratios of RUBIS-to-SAPHIR are shown in Figure 6. The results from the spectral ratios indicate that the "average" slope between the two events over the stations is near zero, and that some of the stations show positive slopes while others show negative slopes. The bandwidths are in most cases limited to between 0.5 and 3.0 Hz. The azimuths of these stations span about 45° (due north, EKA, to northwest, BL-WV, see Figure 1). The data indicate that RUBIS and SAPHIR have similar average frequency content and that the effect of scattering may vary rapidly with azimuth in the real 3-D world.

### COMPARISONS WITH DECONVOLVED DATA

Four events EMERAUDE, GRENAT, RUBIS, and SAPHIR were deconvolved at the EKA and YKA arrays using the method of Shumway and Der (1985). The results are shown

in Figure 7. The equivalent seismic sources for the events are shown side-by-side for the two arrays and a comparison can be made for EMERAUDE, GRENAT, and SAPHIR (RUBIS was poorly recorded at YKA). The initial P waveform is similar for each event at the two arrays while the differences are greatest beginning about 0.5 sec after the initial P wave. SAPHIR shows the clearest differences between the two arrays; the negative pulse following the positive pulse is strong at EKA but absent at YKA. EMERAUDE and GRENAT show differences in timing of the negative (and small positive) pulses following the initial P wave. These differences argue in favor of a scattering model for the variations in the free surface interaction for these events.

Deconvolutions of available LRSM data for SAPHIR and RUBIS are presented in Figures 8A, and 8B. The waveforms show bandlimited estimates of the ground displacement at each station for the two events. The instrument response and a constant  $t^*$  attenuation operator (Futterman, 1962; Azimi et al., 1968) have been removed from the digital waveforms and a bandlimiting filter has been applied to maximize the broadband signal-to-noise ratio of the data. The data is generally limited to frequencies between 0.25 and 4.0 Hz. Lower Q stations are limited to frequencies below 3.0 Hz. Details of the deconvolution procedure are presented in McLaughlin et al (1986b).

The displacement waveforms of Figures 8A and 8B are arranged with increasing source-to-receiver azimuth from top to bottom. The area under the initial causal P waveform is shaded. There are several characteristics of the waveforms that are readily apparent.

First, the initial displacement P wave is rather simple with a few exceptions. Because of the bandlimited nature of the deconvolutions, features with time constants shorter than 0.3 seconds are probably not resolvable. In fact the variability of the initial P waveform with few exceptions could be attributed to variations in the resolution kernels of the deconvolutions.

Second, there are several positive pulses (labeled "A" and "(A)") that can be correlated from station-to-station with similar takeoff angles and azimuths. For example, the two stations GI-MA (Montana) and HL-ID (Idaho) show a similar positive arrival labeled "A" from the explosion RUBIS. Although RK-ON is at nearly the same azimuth as these two stations, RK-ON is at a greater distance on the focal sphere from either of the two stations because of dependence of takeoff angles on epicentral distance. If these arrivals are generated near the source, they would indicate significant direction properties of the P coda generation process.

Third, there is little or no consistent simple "pP" at the majority of stations for either SAPHIR or RUBIS. Those stations that do show negative excursions have generally longer period and possibly multiple negative arrivals following the first positive polarity P pulse by 0.5 to 1.0 seconds. Given the high P-wave velocity (about 5.8 km/s) of the granite mountain, Taourirt Tan Affela, the "linear elastic" pP-P times should be considerably less than 0.5 seconds for both explosions.

Several fundamental differences exist between 2-D and 3-D wave propagation that prevent quantitative comparison of observations and synthetics. The most significant of these differences may be that 2-D Rayleigh waves from line sources do not have geometrical spreading and that 2-D P-waves attenuate proportional to  $\frac{1}{\sqrt{r}}$  rather than  $\frac{1}{r}$ . Therefore we should expect that the teleseismic P-coda from line sources in a 2-D structure will over estimate the effects of 3-D scattering. Because of this we can make only qualitative comparisons of the observations with the synthetic calculations. Given this caveat, we can draw some parallels between the synthetics and the deconvolved LRSM records.

P coda elements common to different stations with similar takeoff angle and azimuth may be attributed to the source region. The longer period pulses that follow the RUBIS P wave by about 1 second are seen at GI-MA, KN-UT, HN-ME, and LC-NM. Similar long-period

positive polarity secondary pulses may be seen on the synthetics of Figures 9A and 9B. The synthetic positive polarity secondary arrivals appear to be scattered Rayleigh-to-P from the topography as Rayleigh waves excited on the free surface are scattered at topographic slope changes and contribute to P coda.

Another characteristic of the observed data is the variability of any pP arrivals. The linear elastic pP pulse is expected to follow the P wave much earlier than observed. No such negative polarity pulse is consistently observed within 0.5 seconds on the majority of the waveforms. Some displacement waveforms suggest greatly delayed or multipathed pP pulses (SAPHIR at BL-WV, BR-PA, HN-ME, and VO-IO, and RUBIS at EU-AL, BL-WV, DH-NY, HN-ME, KN-UT, FR-MA, GI-MA, RK-ON, and HL-ID). This same characteristic may be seen in the synthetics at various azimuths and takeoff angles. The 2-D linear elastic pP reflection can be focused (or defocused) by constructive (or destructive) reflections from the topography. This linear elastic P+pP interference introduces fluctuations in the "bc" swing of the teleseismic P-wave seismograms.

Non-linear spall could also produce these same two characteristics seen in the data and the 2-D synthetics. Non-linear spall could produce multiple, lengthened and delayed "pP" arrivals as well as other secondary phases. However, the elastic 2-D linear finite difference calculations indicate that at least some of these effects may be due to steep topographic scattering. The spall mechanisms may not be required to explain the lack of clear pP arrivals for the RUBIS and SAPHIR teleseismic displacement waveforms.

### WWSSN MAGNITUDE VARIATIONS

In order to address the question as to whether the short-period  $m_b$  magnitude distribution has any evidence of scattering, we have examined the measurements of  $m_b(\text{Pa})$ ,  $m_b(\text{Pb})$ , and

$m_b(P_{max})$  made at WWSSN stations for RUBIS, SAPHIR, GRENAT, and TOURMALINE. The "Pa" measurement is the zero-to-peak amplitude of the first motion of the short period seismogram, "Pb" is 1/2 of the a-to-b peak-to-peak measurement. "Pmax" is 1/2 the maximum peak-to-peak measurement in the first 5 seconds of the P arrival.

The magnitudes were estimated in a maximum likelihood sense (Ringdal, 1976) and are listed in Table 2. The data is corrected for the biasing effects of non-detection and/or clipping. In the case of non-detection, the noise level is measured at the expected arrival time for the P wave and used as the detection threshold. In the case of clipping, a conservative estimate was made of the maximum visible peak-to-peak deflection on the seismogram and used as the clipping level. The station corrections of Ringdal (1986) and the distance corrections of Veith and Clawson (1972) were applied to the individual station magnitudes. Uncertainties in the event magnitude were estimated by use of a bootstrap procedure (Efron, 1981). PILEDRIVER and SHOAL are included for comparison; these are the only US granite explosions for which WWSSN data is available.

TABLE 2 MAXIMUM LIKELIHOOD MAGNITUDE ESTIMATES			
EVENT	$m_b(P_a)$	$m_b(P_b)$	$m_b(P_{max})$
RUBIS	4.76(.08)	5.14(.06)	5.42(.06)
SAPHIR	5.18(.06)	5.49(.07)	5.75(.06)
GRENAT	4.04(.12)	4.41(.07)	4.69(.07)
TOURMALINE	3.99(.20)	4.31(.10)	4.60(.07)
PILEDRIVER	4.93(.05)	5.21(.04)	5.46(.05)
SHOAL	4.09(.10)	4.32(.08)	4.63(.08)

As expected, the smallest events are the most uncertain. The French Sahara magnitude distributions have standard deviations of a single observation of 0.40(0.05) magnitude units.

The  $m_b(P_a)$ ,  $m_b(P_b)$ , and  $m_b(P_{max})$  are correlated across the network such that the logarithmic ratios,  $\log(P_{max}/P_a)$ ,  $\log(P_b/P_a)$ , and  $\log(P_{max}/P_b)$  are well defined. These ratios are estimated in a maximum likelihood sense and listed in Table 3. The standard deviation of the log-ratio distributions,  $\sigma$ , are also listed. The estimates of  $\log(P_{max}/P_a)$  and  $\log(P_b/P_a)$  for GRENAT and TOURMALINE may not be as well determined as those for SAPHIR and RUBIS.

TABLE 3 MAXIMUM LIKELIHOOD LOG-RATIO ESTIMATES						
EVENT	$\log(P_{max}/P_a)$		$\log(P_b/P_a)$		$\log(P_{max}/P_b)$	
	$\sigma$		$\sigma$		$\sigma$	
RUBIS	0.55	0.27	0.26	0.18	0.23	0.17
SAPHIR	0.53	0.28	0.25	0.19	0.21	0.19
GRENAT	0.67	0.45	0.36	0.42	0.24	0.16
TOURMALINE	0.70	0.45	0.32	0.34	0.25	0.17
PILEDRIIVER	0.52	0.28	0.25	0.19	0.22	0.18
SHOAL	0.49	0.22	0.31	0.16	0.31	0.16

Comparison of the  $\sigma$  values listed in Table 3 with the  $\sigma = 0.4$  value found for the  $m_b(P_a)$ ,  $m_b(P_b)$ , and  $m_b(P_{max})$  distributions give estimates of the normalized correlations of  $\log(P_a)$ ,  $\log(P_b)$ , and  $\log(P_{max})$ .  $\log(P_{max})$  and  $\log(P_b)$  are 80% correlated across the network for all of the explosions,  $\log(P_b)$  and  $\log(P_a)$  are 70% correlated across the network, but  $\log(P_a)$  and  $\log(P_{max})$  are only 40% correlated across the network for RUBIS and SAPHIR. Since the  $\log(P_a)$  measurement is the least disturbed by topographic scattering we may expect that at least 40% of the network magnitude variance shared by  $\log(P_{max})$  and  $\log(P_a)$  has little or nothing to do with topographic scattering. That is to say that we can attribute at most 60% of the  $\log(P_{max})$  variance to topographic scattering and that at least 40% of the variance must be due to other perturbations. This would place an upper bound on the rms magnitude variation due to topographic scattering of about 0.3 magnitude units.

Additional evidence comes from the correlation of event magnitude residual patterns and the "average" residual pattern. The  $m_b(P_{max})$  average residual pattern for the Ahaggar test site is shown in Figure 10. This residual pattern has an rms variation of 0.30 magnitude units and accounts for 40% of the variance of  $m_b(P_a)$ ,  $m_b(P_b)$ , and  $m_b(P_{max})$  for any of the French Sahara shots. This would place an upper limit of 0.3 rms magnitude units on the topographic effect since the events were located at different places within the mountain. The residual pattern of Figure 10 is consistent with focusing-defocusing of seismic energy across the network. Clusters of large positive and negative residuals can be seen in the network with rapid variation in takeoff angle.

The station residuals for both  $m_b(P_a)$  and  $m_b(P_b)$  are 50% correlated between RUBIS and SAPHIR indicating an upper limit of 0.2 magnitude units for the topographic scattering effect. Since RUBIS and SAPHIR are expected to show uncorrelated variations due to topographic scattering, we can place an upper bound of 0.2 magnitude units on the rms magnitude variation due to topographic scattering. Finally, the  $m_b(P_{max})$  station residuals are 80% correlated between SAPHIR and RUBIS and this would suggest an upper bound of 0.15 rms magnitude units due to topographic scattering.

We are left with a maximum  $\log(P_{max})$  rms variation of 0.15 magnitude units across the WWSSN network due to topographic scattering. This is in line with what could be expected due to the vagaries of P+P interference variations due to topographic scattering. However, it is clear that the dominant contribution to the  $m_b$  variance is due to event-station perturbations that are common between events for the test site and therefore are either deep seated beneath the test site, or are associated with the stations.

### CONCLUSIONS

We have made qualitative comparisons of 2-D LFD calculations for line sources under a topographic feature with observations of explosions at the French southern Sahara Test Site. The 2-D simulations suggest that the linear elastic free surface (pP) reflections could be strongly affected by topography for RUBIS and SAPHIR. The presence or absence of a pP may produce a 0.3 magnitude variation in the network  $m_b$ . The topography could also produce variations of 0.3 magnitude units in the P-wave teleseismic magnitudes by scattering of Rayleigh-to-P at the free surface. However, since the 2-D calculations probably over estimate the P coda, this should be considered an upper bound on the magnitude variations that would be introduced by such topography. Near-source topographic scattering is expected to be a strong function of azimuth and takeoff angle. These variations of 0.3 magnitude units would be manifested in a plus or minus 0.15 magnitude variation about an average and therefore be responsible for at most a 0.15 magnitude variation about the mean.

2-D numerical experiments suggest that spectral ratios may be diagnostic of scattering from topography, however simple spectral ratio measures do not show convincing evidence for scattering from the topography at Taourirt Tan Afella Massif. This could be due to limitations of the 2-D simulations or it could be that the bandwidths of the teleseismic P waves are too narrow.

2-D numerical experiments suggest that explosion line source generated pP may be focused or defocused by topography at Taourirt Tan Afella Massif. The deconvolved displacement P waveforms at the arrays EKA and YKA and across the network of LRSM stations do show evidence for significant variation in the free surface interaction with takeoff angle and azimuth. No simple pP is reliably observed and several long-period positive pulses are observed following the the initial P wave by 1 to 2 seconds. These positive pulses may be scattered Rayleigh-to-P contributions to the P coda. The pP may be defocused at some



azimuths and takeoff angles by the mountain topography. However, non-linear interaction with the free surface, such as spall, may also be responsible for these observations.

Magnitude statistics for the French Sahara explosions demonstrate that there is considerable variation in the P waveforms observed at WWSSN stations. The strong correlations between  $\log(P_a)$ ,  $\log(P_b)$  and  $\log(P_{\max})$  and the near source contribution to the variance of the logarithmic ratios of  $\log(P_{\max}/P_a)$ ,  $\log(P_{\max}/P_b)$ , and  $\log(P_b/P_a)$  indicate that the contribution of path-receiver variation to the magnitude scatter is nearly 80% of the magnitude variance regardless of the portion of the P waveform that is measured. An upper bound of 0.15 rms magnitude variation may be attributed to the topographic scattering from the magnitude statistics. This is in rough agreement with what may be expected from focusing-defocusing of pP by topography or the Rayleigh-to-P scattering by the topography at Taourirt Tan Afella Massif.

#### ACKNOWLEDGEMENTS

This work was supported by the Defense Advanced Projects Agency and monitored by the Air Force Geophysics Laboratory under contract F19628-85C-0035. The views and conclusions contained in this report are those of the authors and should not be interpreted as necessarily representing the official policies, either expressed or implied, of the Defense Advanced Research Projects Agency or the U.S. Government.

## REFERENCES

- Azimi, S. A., A. V. Kalinin, V. V. Kalinin, and B. L. Pivovarov (1968), Impulse and transient characteristics of media with linear and geometric absorption laws, *Izvestiya, Physics of the Earth*, 88-93.
- Blandford, R. R. and R. H. Shumway (1982), Magnitude-yield for nuclear explosions in granite at the Nevada test site and Algeria: joint determination with station effects with data containing clipped and low-amplitude signals, *VSC-TR-82-12*, Teledyne Geotech, Alexandria, Va.
- Blandford, R. R., R. H. Shumway, R. Wagner, and K. L. McLaughlin (1984), Magnitude yield for nuclear explosions at several test sites with allowance for station effects, truncated data, amplitude correlation between events within test sites, absorption, and pP, *TGAL-TR-83-6*, Teledyne Geotech, Alexandria, Va.
- Crough, S. T., (1981), Free-air gravity over the Hoggar massif, northwest africa: evidence for alteration of the lithosphere, *Tectonophysics*, 77, 189-202.
- Duclaux, F. and M. L. Michaud (1970), Conditions experimentales des tirs nucleaires souterrains francais au Sahara, *R. Acad. Sc. Paris*, t. 270 (12 Janvier 1970) Serie B 189-192.
- Efron, B. (1981), Censored data and the bootstrap, *J. Am. Statist. Assoc.*, 76, 312-319.
- Faure, J. (1972) Recherches sur les effets geologiques d'explosions nucleaires southeraines dans un massif de granite saharien, Centre d'Etudes de Bruyeres-le-Chatel, Commissariat a l'Energie Atomic Report CEA-R-4257 Service de Documentation CEN-SACLAY B.P. no. 2, 91-GIF-sur-Yvette, France.
- Futterman, W. I. (1962), Dispersive body waves, *J. Geophys. Res.*, 67, 5279-5291.
- Greenfield, R. J. (1971), Short-Period P-wave generation by Rayleigh-wave scattering at Novaya Zemlya, *J. Geophys. Res.*, 76, 7988-8002.
- Jih, R.-S., K. L. McLaughlin, and Z. A. Der (1986), Boundary conditions of arbitrary polygonal topography in elastic finite difference scheme for seismogram generation, *TGAL-TR-86-03*, Teledyne Geotech, Alexandria, VA. (Section 1 of this report, submitted for publication).
- Key, F. A. (1967), Signal-generated noise recorded at the Eskdalemuir seismometer array station, *Bull. Seism. Soc. Am.*, 57, 27-38.
- McLaughlin, K. L., R. H. Shumway, R. O. Ahner, M. Marshall, T. W. McElfresh, and R. Wagner (1986a), Determination of event magnitudes with correlated data and censoring: a maximum likelihood approach, *TGAL-86-01*, Teledyne Geotech, Alexandria, Va.

McLaughlin, K. L., A. C. Lees, and Z. A. Der (1986b), Teleseismic spectral estimates of  $M_0$  and  $\Psi_{\infty}$  estimates for four French Explosions in southern Sahara, *TGAL-86-03*, Teledyne Geotech, Alexandria, Va. (section 2 of this report, submitted for publication).

Robinson, E. A. (1983), *Multichannel time series analysis with digital computer programs*, 2nd Edition, Goose Pond Press, Houston, Tx.

Ringdal, F. (1976), Maximum likelihood estimation of seismic magnitude, *Bull. Seism. Soc. Am.*, 66, 789-802.

Ringdal, F. (1986). Study of magnitudes, seismicity and earthquake detectability using a global network, manuscript.

Rodean, H. C. (1979), ISC events from 1964 to 1976 at and near the nuclear testing ground in eastern Kazakhstan, *UCRL-52856, Lawrence Livermore Laboratory*, Livermore, Calif., 94550.

Shumway, R. H. and Z. A. Der (1985), Deconvolution of multiple time series, *Technometrics*, 27, 385-393.

Veith, K. F., and G. E. Clawson (1972), Magnitude from short period P-wave data, *Bull. Seism. Soc. Am.*, 62, 435-452.

von Seggern D. H. and R. R. Blandford (1972), Source time functions and spectra for underground explosions, *Geophys. J. Roy. astr. Soc.*, 31, 83-87.

## FIGURE CAPTIONS

FIGURE 1. Topographic map Taourirt Tan Afella Massif from Duclaux and Michaud (1970) with event locations from Faure (1972) for SAPHIR (S), RUBIS (R), EMERAUDE (E), and GRENAT (G). Contours are 100 meters. The dashed line is the outcrop of the Taourirt Tan Afella Massif granite. Azimuths to several stations and arrays are indicated.

FIGURE 2A. (ABOVE) Topographic profile with line source locations indicated by triangles. FIGURE 2B. (BELOW) Logarithmic amplitude variations for "a", "b", and "max" P waves radiated by the line sources shown above. A 0.3 extreme magnitude variation is produced in the "max" phase due to constructive and/or destructive interference of the P+P phase.

FIGURE 3. Waveforms for the sources indicated in 2A. Left to right and top to bottom correspond each waveform to the grid of source locations indicated in 2A. A 0.3 maximum magnitude variation in the "max" P phase is predicted from left to right corresponding to a constant elevation.

FIGURE 4A. North-to-south topographic profile for Taourirt Tan Afella with an incident 20° plane dilatational wave, time = 0.0 sec. Line source locations are indicated by "S" and "R". 4B, C, D, E and F show the amplitude wave field at time = 0.125, 0.25, 0.375, 0.5 and 0.675 sec.

FIGURE 5A. Synthetic far-field P-wave seismograms for takeoff angles of 0, 5, 10, 15, and 20 degrees for the line source location indicated by "S" in Figure 4A. 100 KT source with  $t^* = 0.45$  sec, and LRSM instrument response.

FIGURE 5B. Synthetic far-field P-wave seismograms for takeoff angles of 0, 5, 10, 15, and 20 degrees for the line source location indicated by "R" in Figure 4A. 100 kT source with  $t^* = 0.45$  sec, and LRSM instrument response.

FIGURE 6. Spectral ratios of RUBIS-to-SAPHIR at YKA, HN-ME, BL-WV, LC-NM and EKA. The spectral ratios are on average flat with respect to frequency but show variation between stations. Spectra were corrected for noise, and only spectral estimates with a signal-to-noise power ratio greater than 2 are plotted.

FIGURE 7. Equivalent seismic sources from the multichannel deconvolution of SAPHIR, RUBIS, GRENAT, and EMERAUDE data at the arrays EKA and YKA using the method of Shumway and Der (1985). RUBIS was poorly recorded at YKA. Note the variation between EKA and YKA for the events EMERAUDE, GRENAT, and SAPHIR. The variation is the greatest for SAPHIR where a negative pulse that follows the positive pulse at EKA is absent at YKA. The area under the initial causal P-wave arrival is shaded.

FIGURE 8A. Deconvolved seismic traces for RUBIS at several LRSM stations arranged in order of increasing azimuth from top to bottom. The area of the initial causal P waveform is indicated in each case. Secondary phases following the initial P wave can be correlated over several stations with similar azimuth, labeled A and (A).

FIGURE 8B. Deconvolved seismic traces for SAPHIR at several LRSM stations arranged in order of increasing azimuth from top to bottom. The area of the initial P waveform is indicated in each case.

FIGURE 9A. Synthetic teleseismic P waves (takeoff angle of 20 degrees) for the 2-D "SAPHIR" models at azimuths of 310, 344, and 0 degrees. Synthetics have only been convolved with an explosion source time function. No distinct well defined elastic pP is apparent although, several long-period complicated negative pulses can be seen to follow the initial P wave. Large positive secondary arrivals can be seen 0.5 sec following the initial P wave at 0 degrees azimuth.

FIGURE 9B. Synthetic teleseismic P waves (takeoff angle of 20 degrees) for the 2-D "RUBIS" models at azimuths of 310, 344, and 0 degrees. Synthetics have only been convolved with an explosion source time function. A distinct well defined elastic pP is only apparent for the azimuth of 0 degrees. Large positive pulses can be seen about 1 second after the P wave for the azimuth of 344 degrees.

FIGURE 10. French southern Sahara test site  $m_b$  residuals across the WWSSN network at epicentral distances between 20 and 95 degrees. Equidistant polar projection with coast lines (TOP), and without coast line (BOTTOM). Positive residuals are octagons, negative residuals are triangles. The size of the symbol is proportional to the absolute value of the station residual.

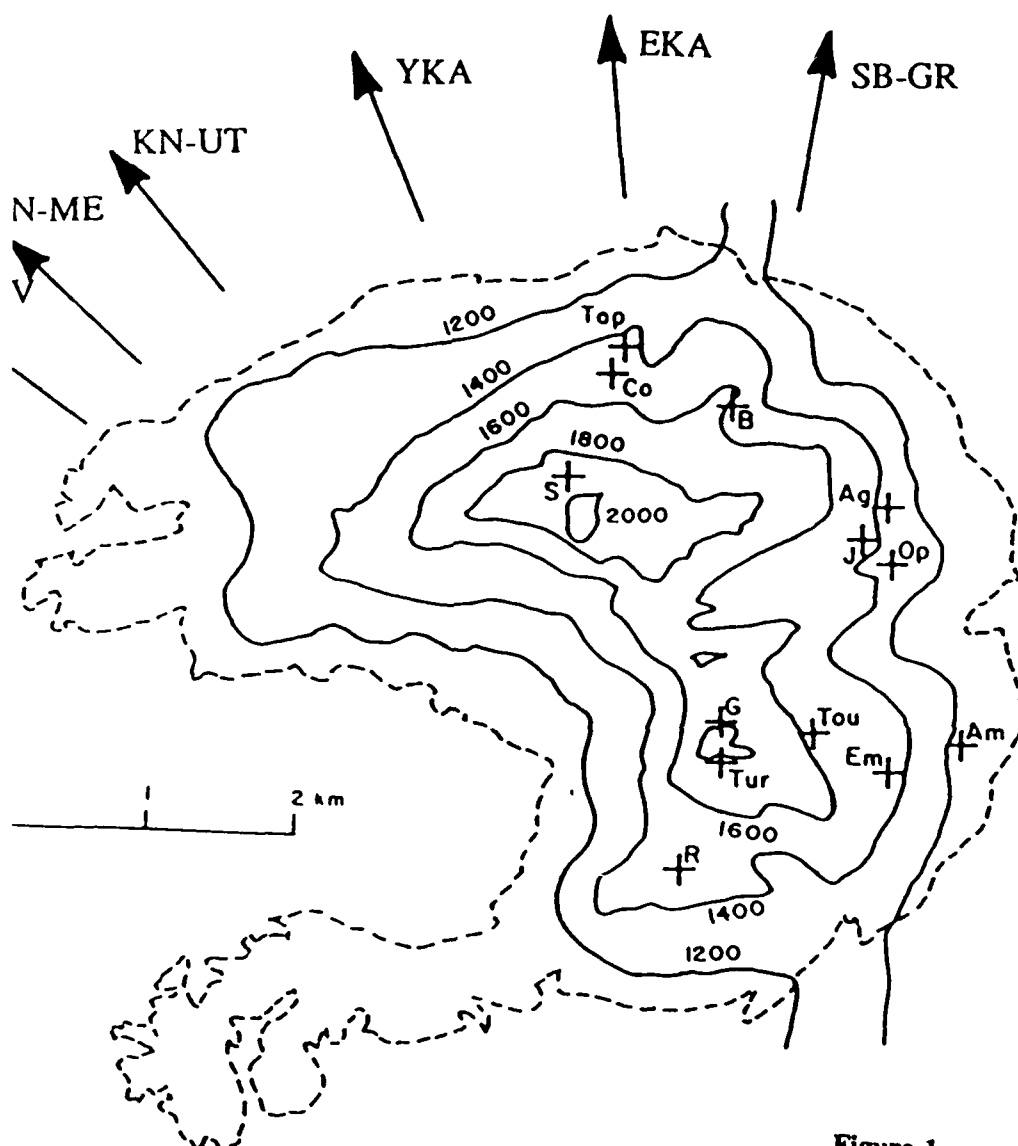


Figure 1.

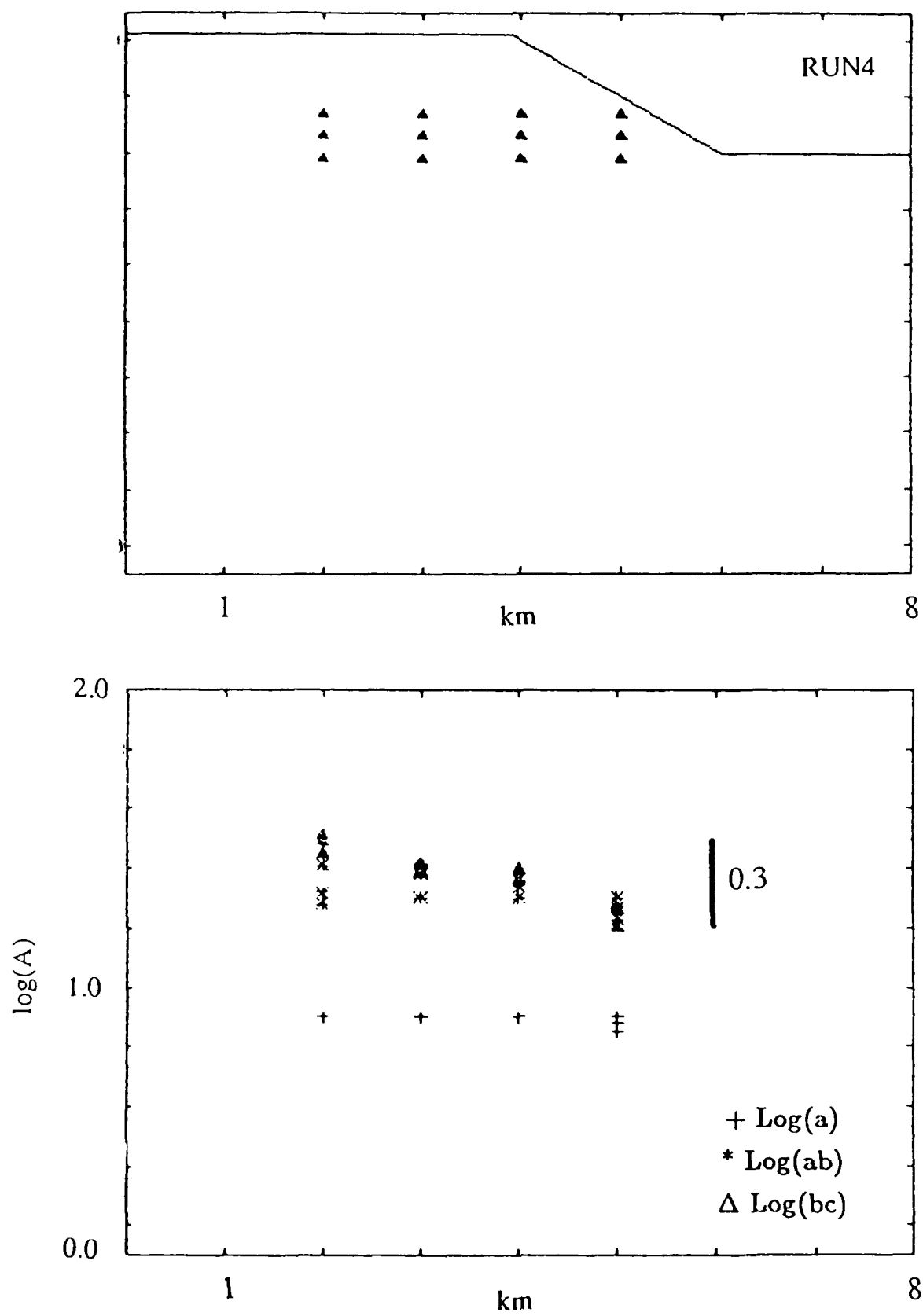


Figure 2.

RUN4

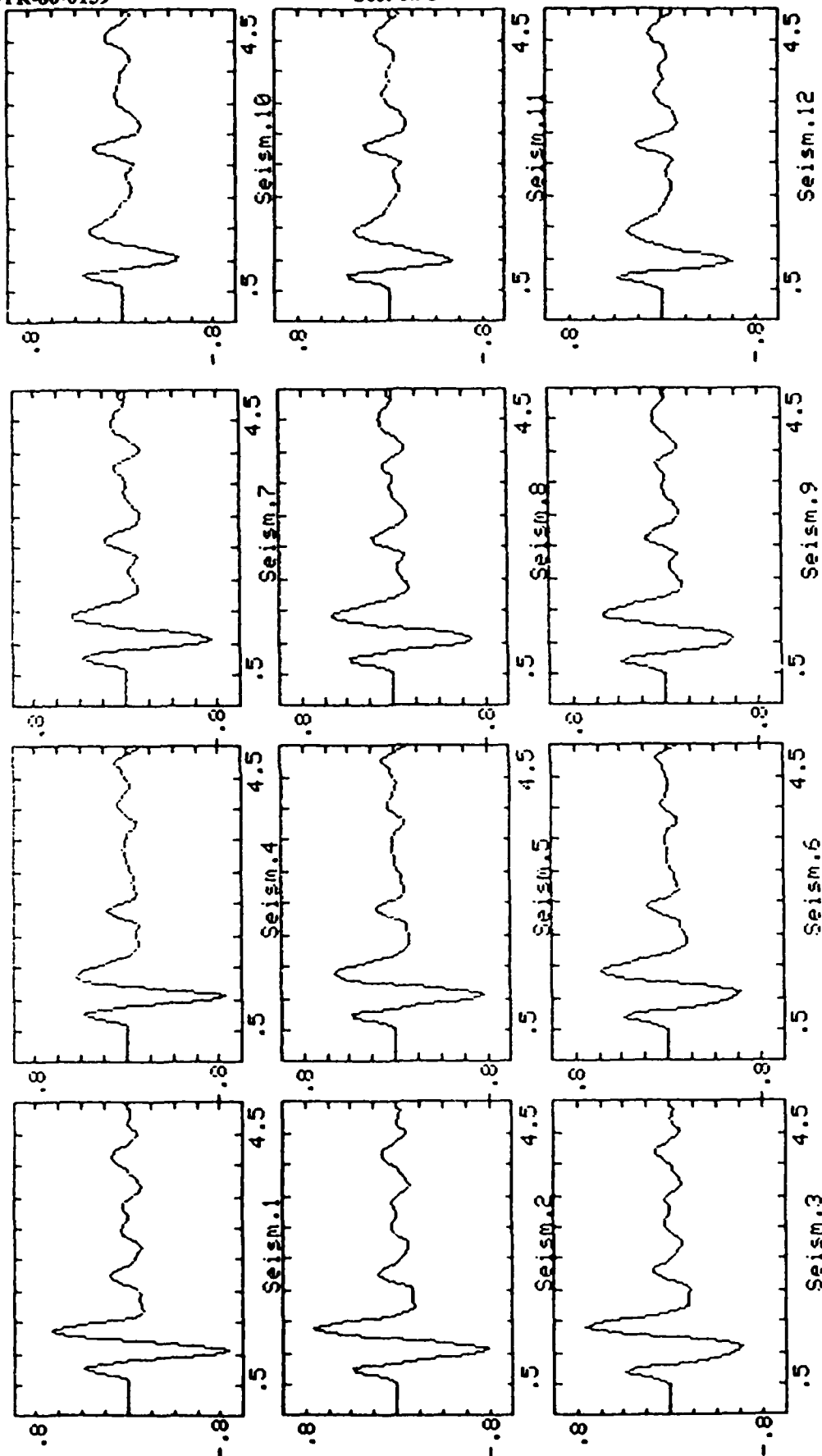


Figure 3.



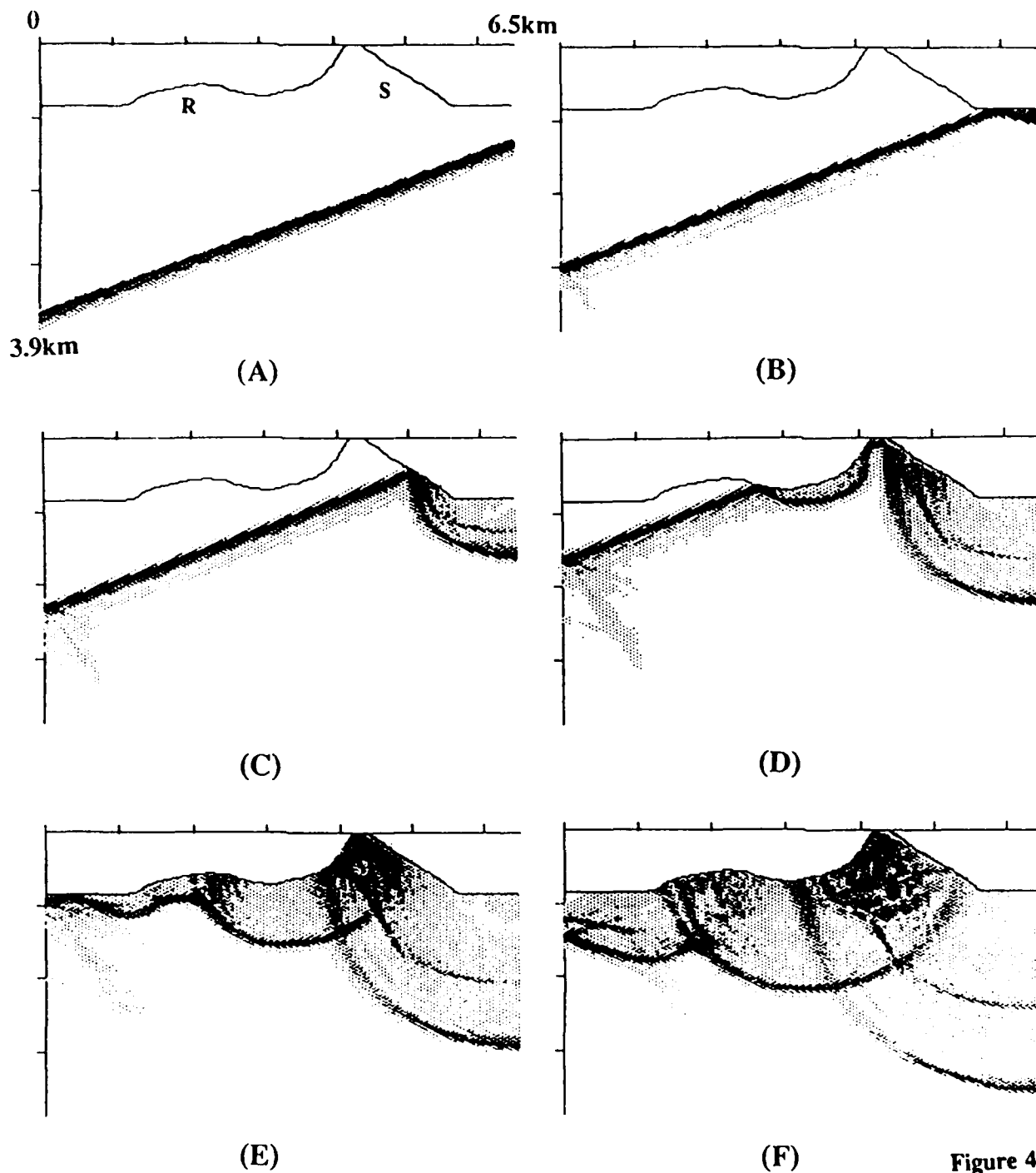
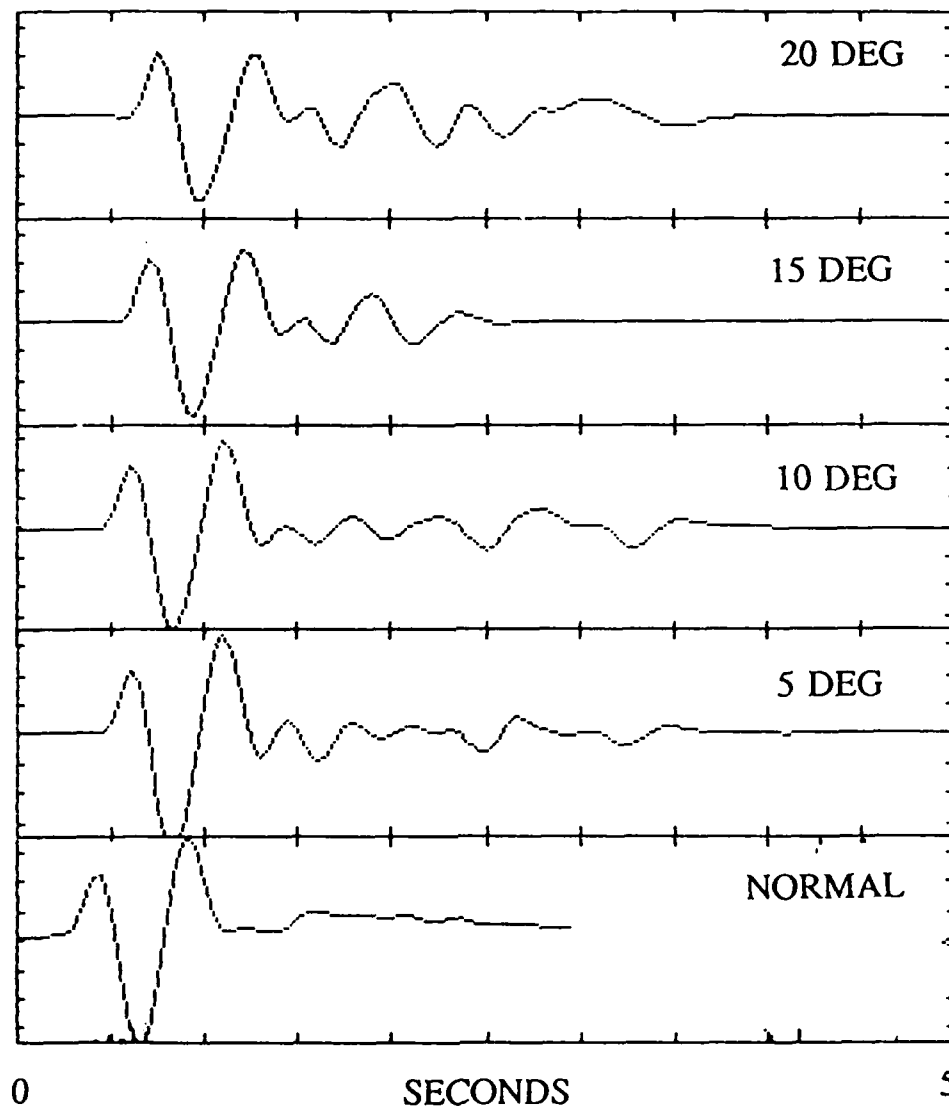


Figure 4.

**SAPHIR**



**Figure 5A.**

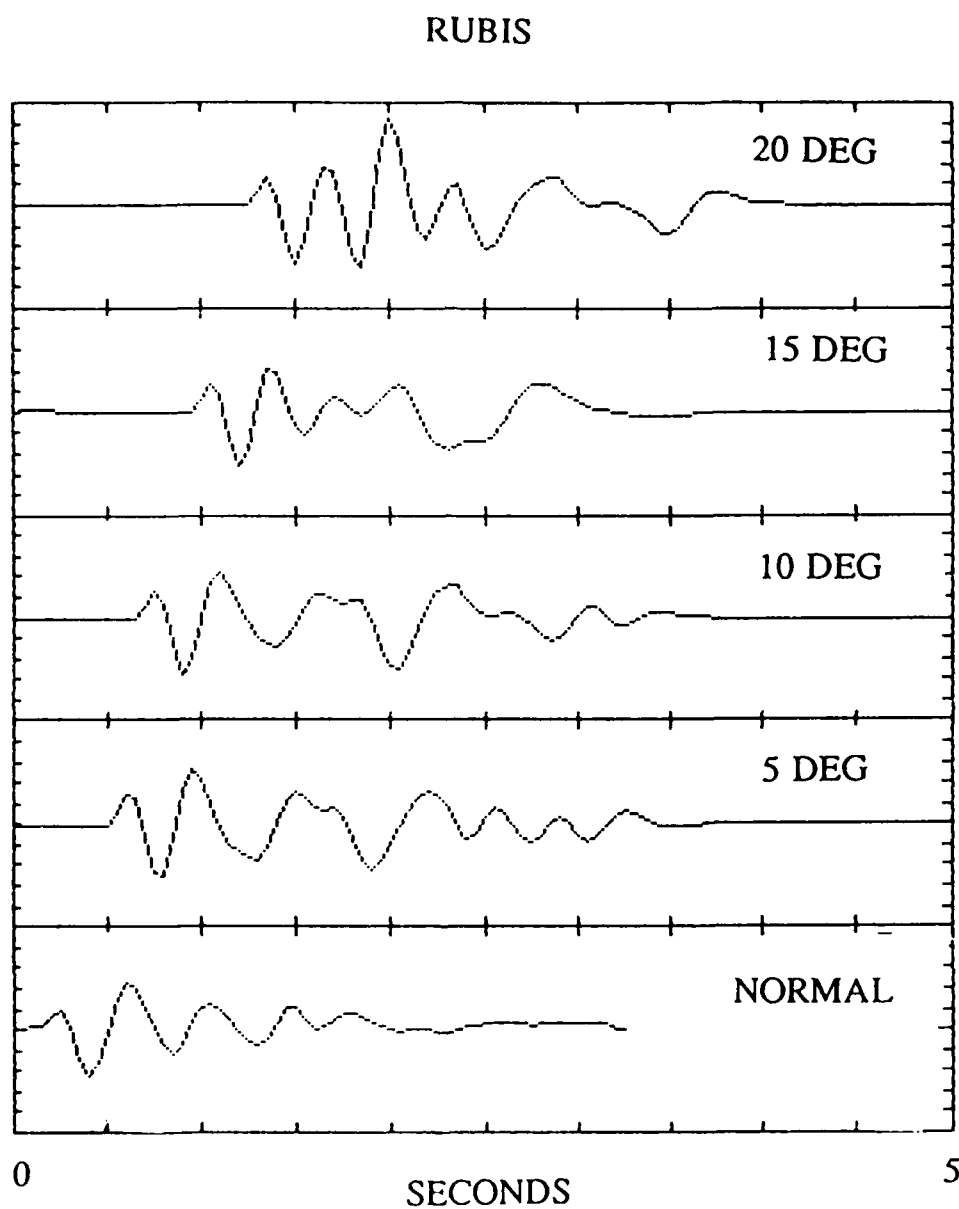


Figure 5B.

NOISE POWER SUBTRACTED FROM SIG  
S/N POWER THRESHOLD = 2.0 N

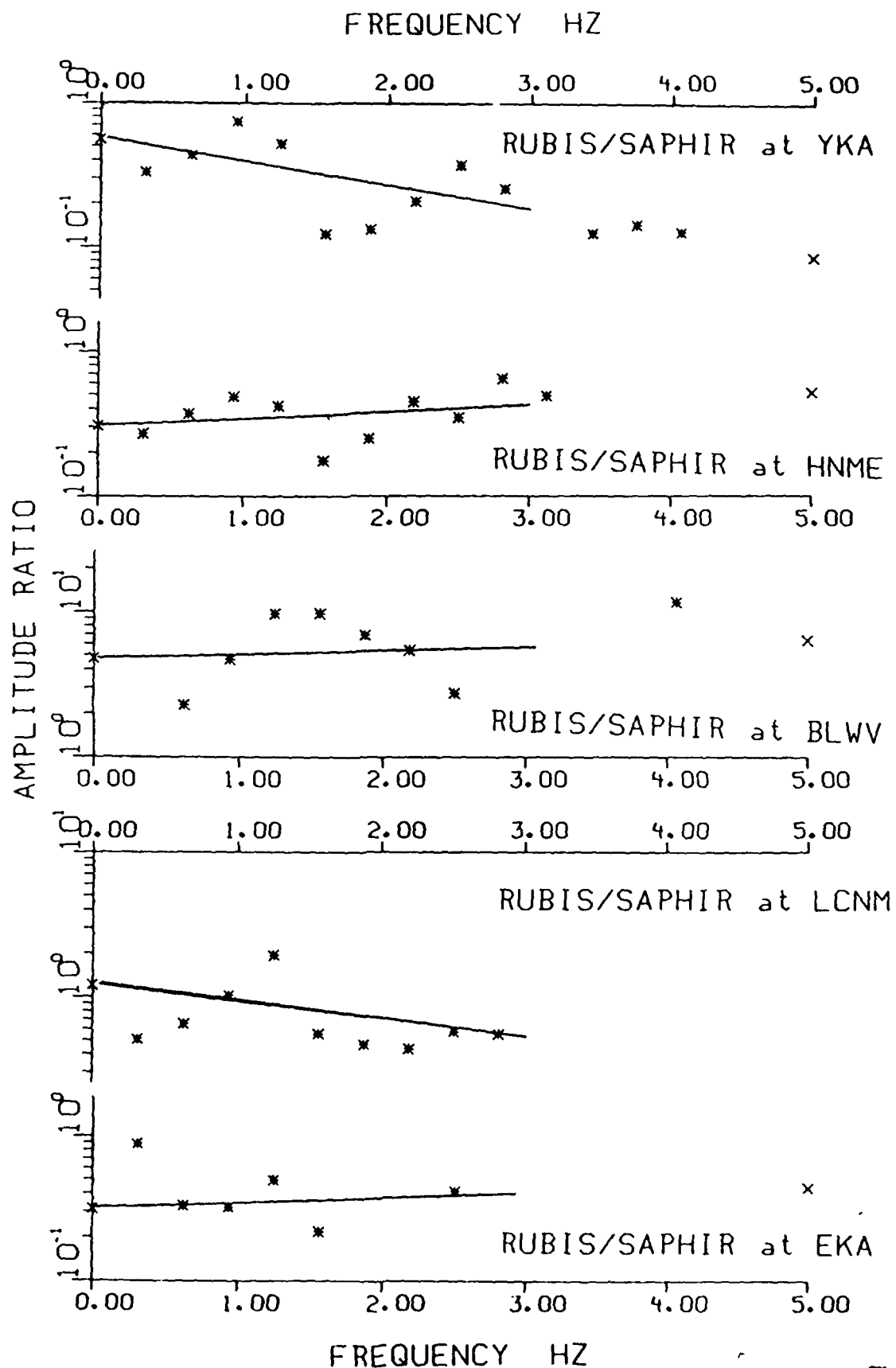


Figure 6.

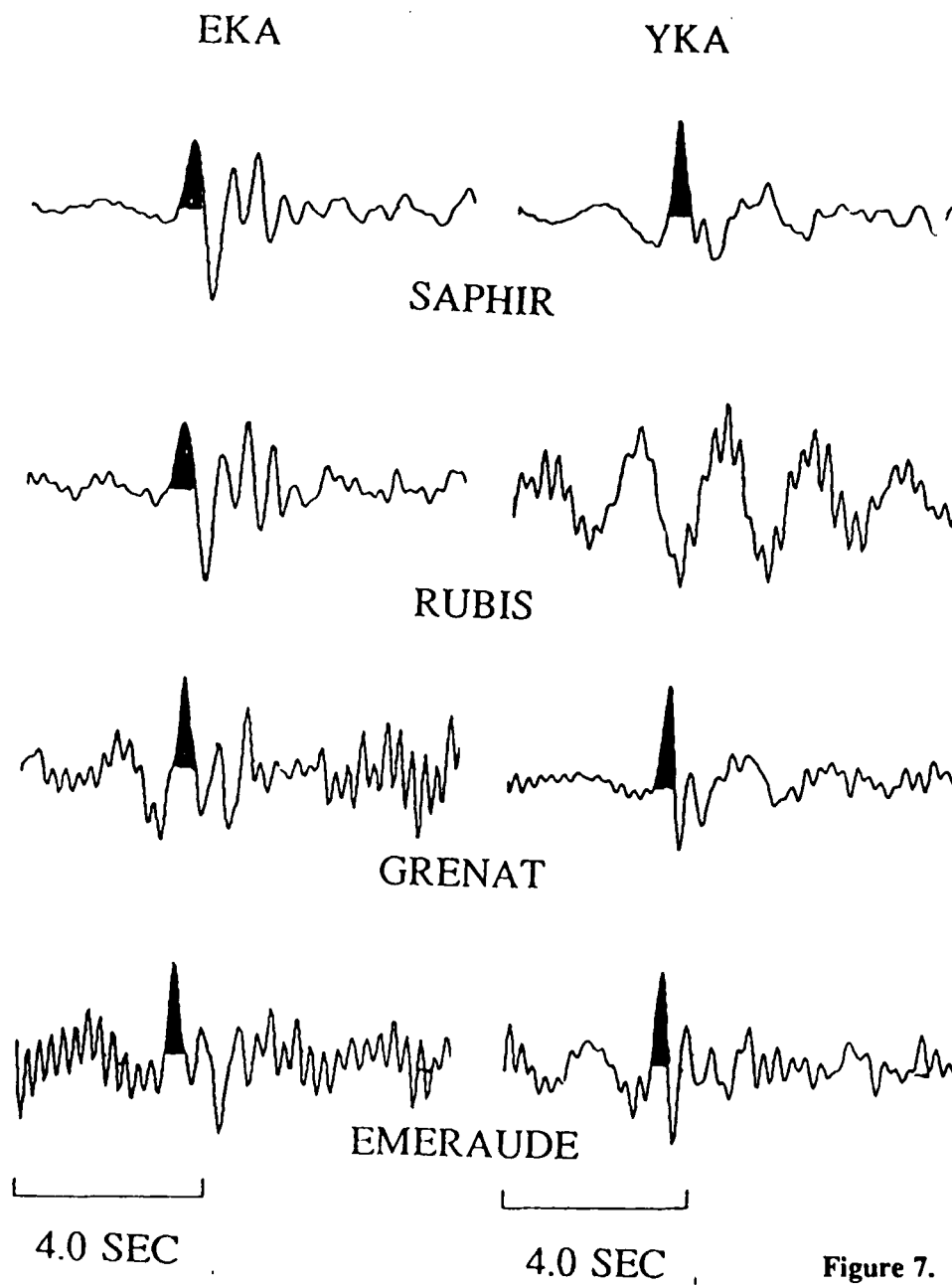


Figure 7.

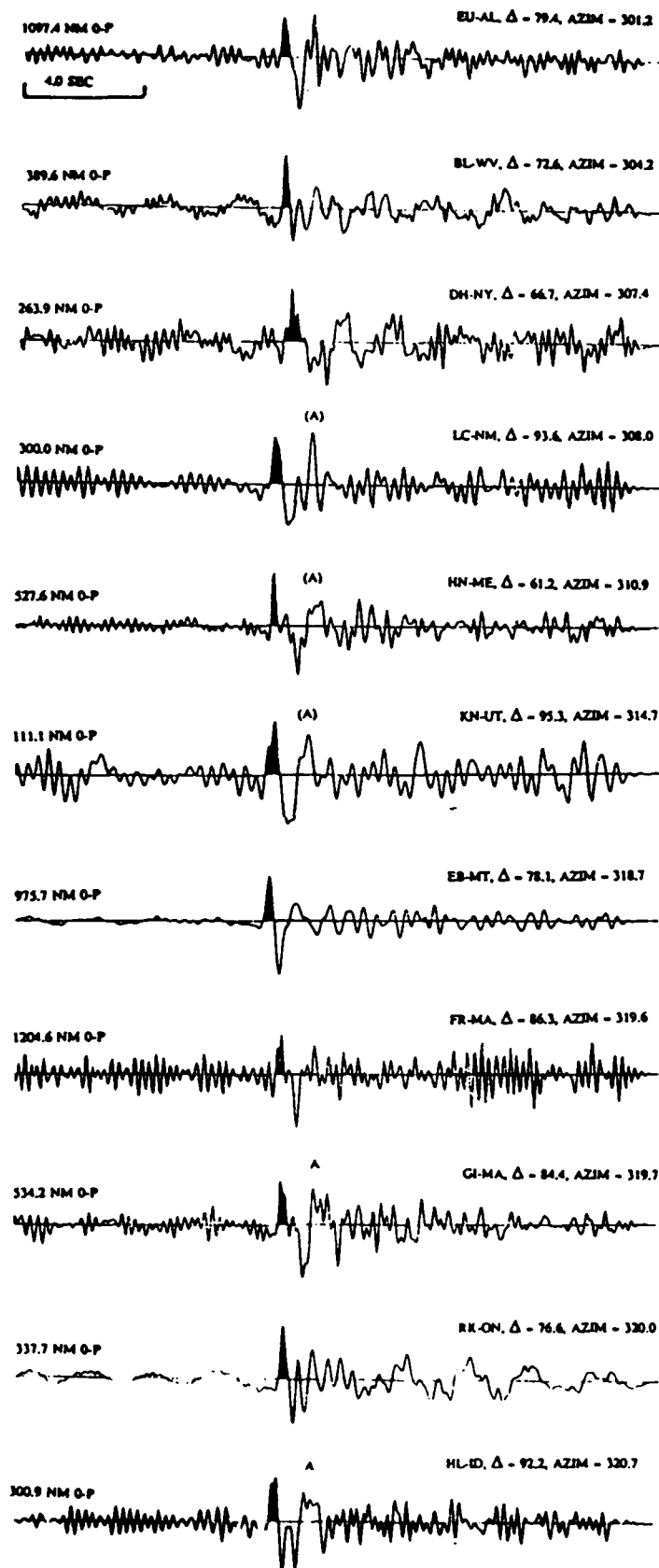


Figure 8A.

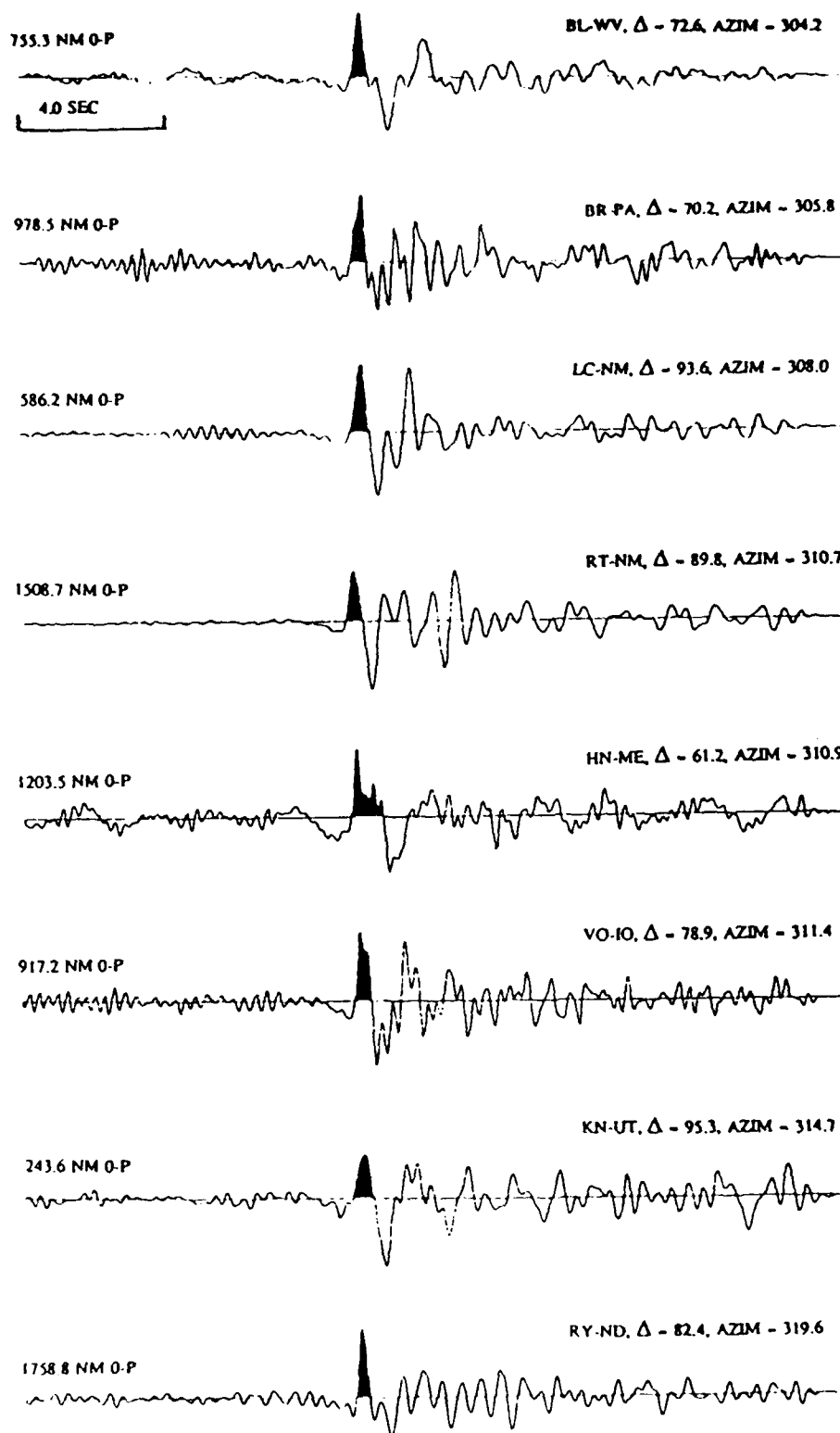


Figure 8B.

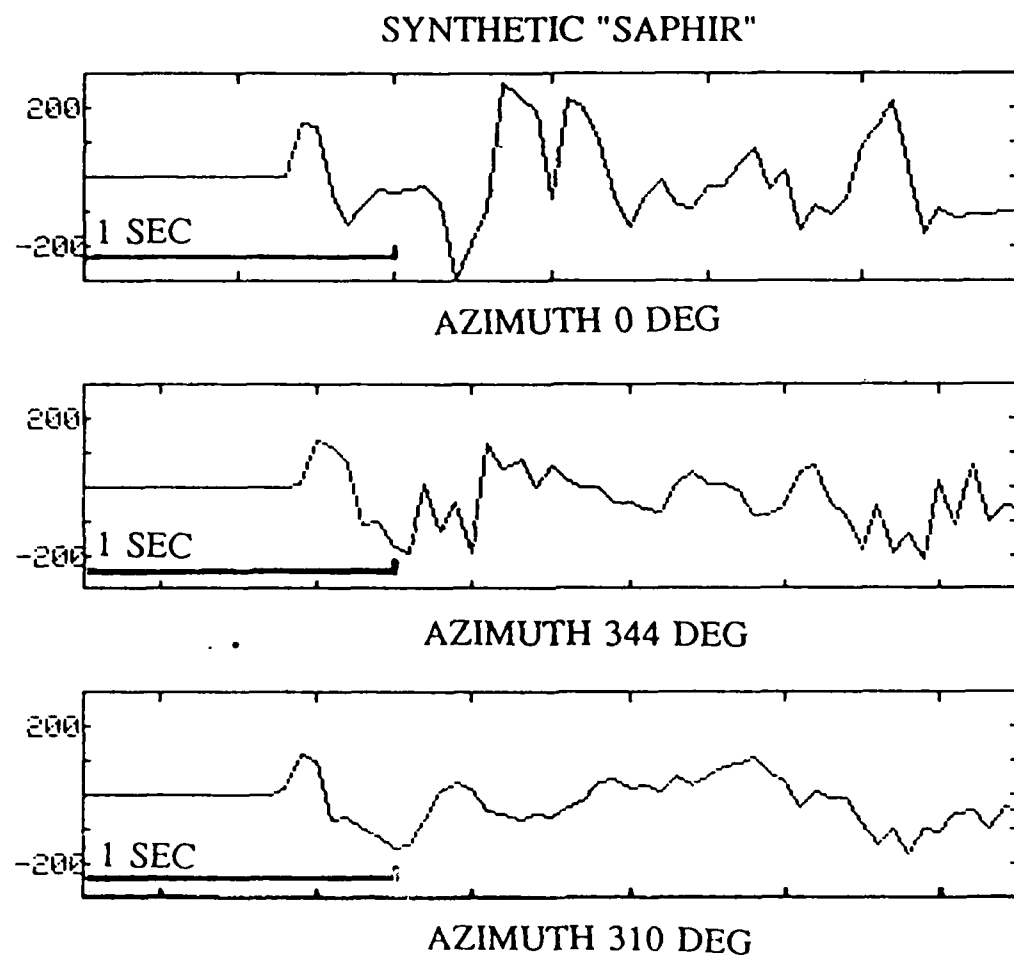


Figure 9A.



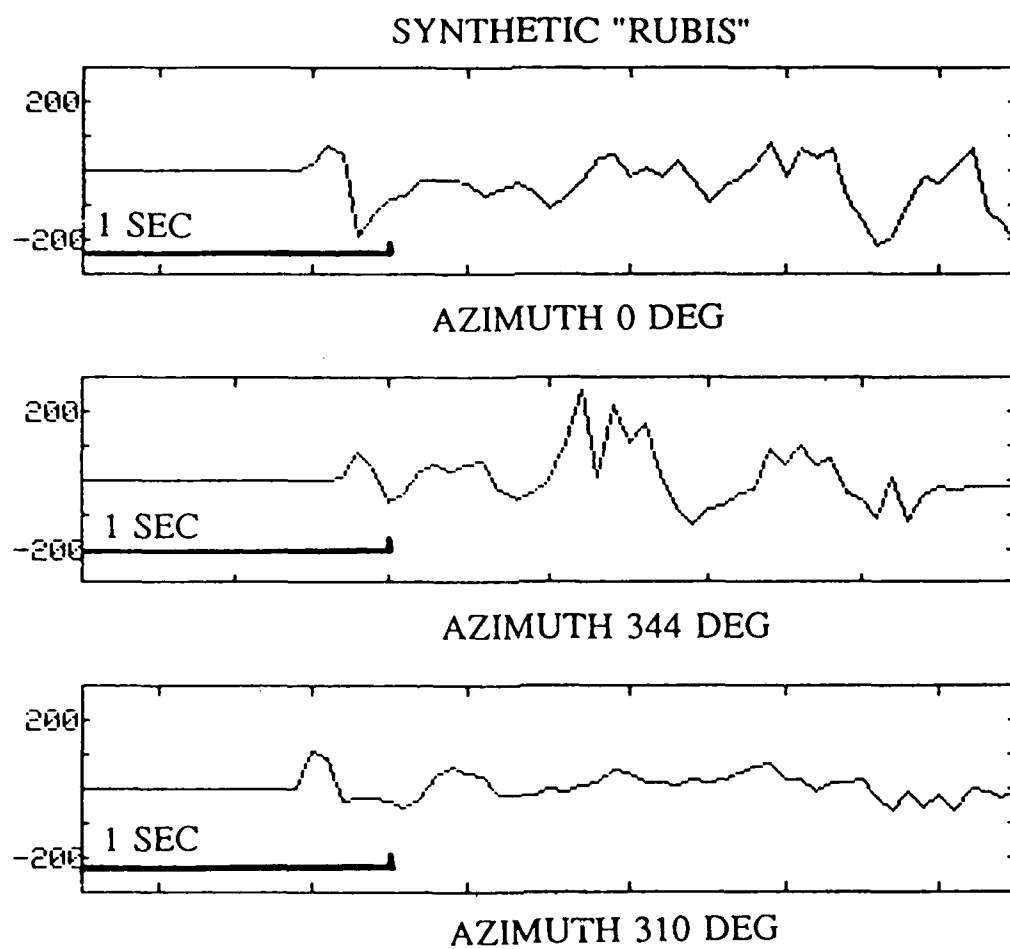


Figure 9B.

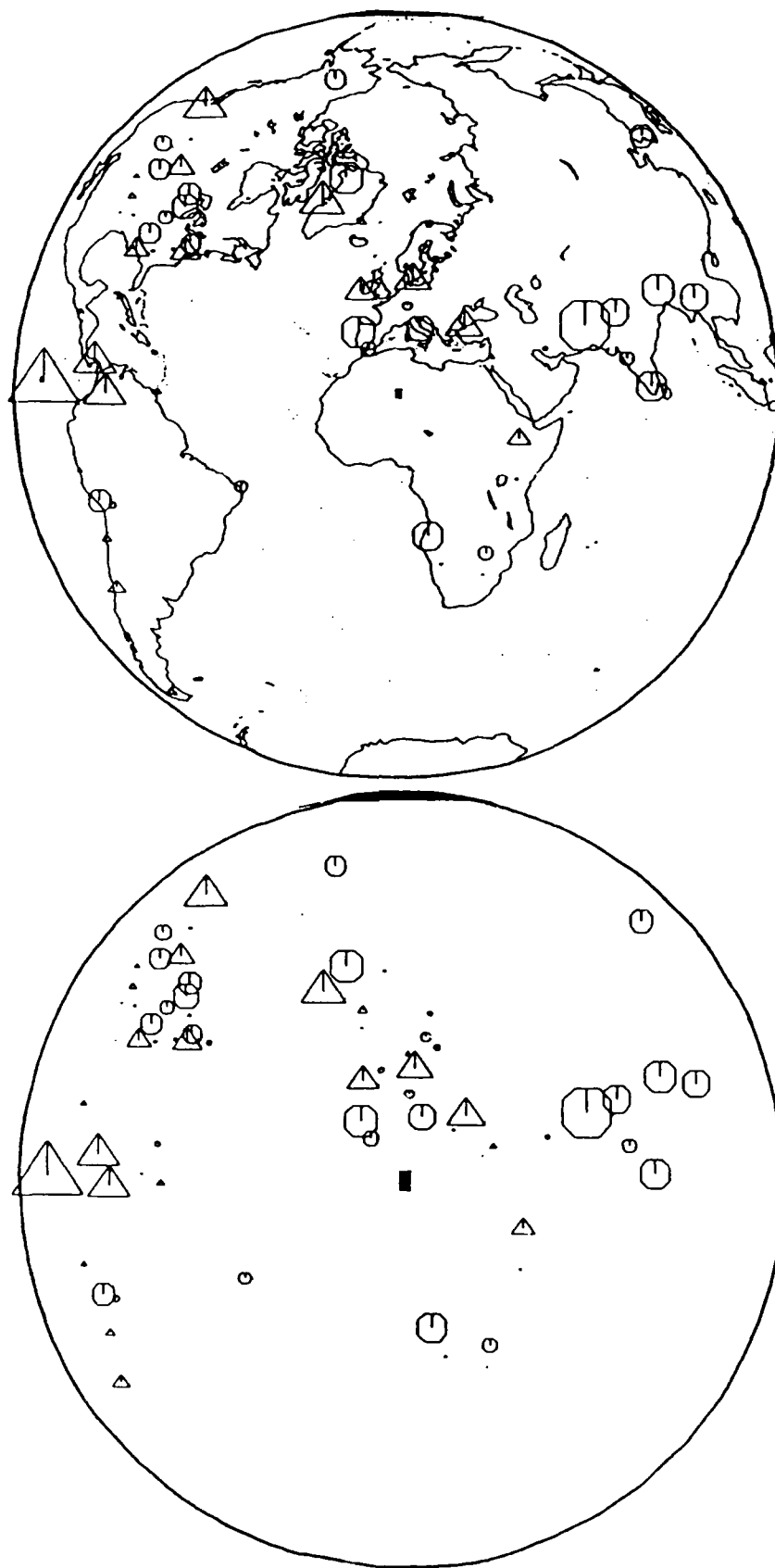


Figure 10

NO-A183 013

THE EFFECTS OF NEAR-SOURCE TOPOGRAPHY ON EXPLOSION  
WAVEFORMS. TELESEISMIC (U) TELEDYNE GEOTECH ALEXANDRIA  
VA ALEXANDRIA LABS K L MCLAUGHLIN ET AL JUL 86

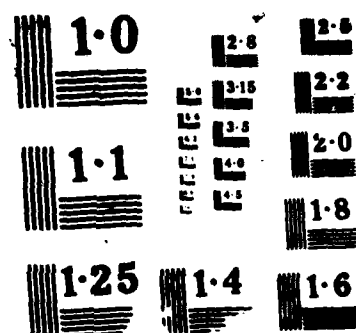
2/2

UNCLASSIFIED

TGAL-86-3 AFGL-TR-86-0159 F19228-85-C-0035 F/G 17/10

NL





## DISTRIBUTION LIST

Dr. Monem Abdel-Gawad  
Rockwell International Science Center  
1049 Camino Dos Rios  
Thousand Oaks, CA 91360

Professor Keiliti Aki  
Center for Earth Sciences  
University of Southern California  
University Park  
Los Angeles, CA 90089-0741

Professor Shelton S. Alexander  
Geosciences Department  
403 Deike Building  
The Pennsylvania State University  
University Park, PA 16802

Professor Charles B. Archambeau  
Cooperative Institute for Research in  
Environmental Sciences  
University of Colorado  
Boulder, CO 80309

Dr. Thomas C. Bache Jr.  
Science Applications Int'l Corp.  
10210 Campus Point Drive  
San Diego, CA 92121

Dr. James Bulau  
Rockwell International Science Center  
1049 Camino Dos Rios  
P.O. Box 1085  
Thousand Oaks, CA 91360

Dr. Douglas R. Baumgardt  
Signal Analysis and Systems Division  
ENSCO, Inc.  
5400 Port Royal Road  
Springfield, VA 22151-2388

Dr. S. Bratt  
Science Applications Int'l Corp.  
10210 Campus Point Drive  
San Diego, CA 92121

Professor John Ebel  
Department of Geology & Geophysics  
Boston College  
Chestnut Hill, MA 02167

Woodward-Clyde Consultants  
Attn: Dr. Lawrence J. Burdick  
Dr. Jeff Barker  
P.O. Box 93245  
Pasadena, CA 91109-3245 (2 copies)

Dr. Roy Burger  
1221 Serry Rd.  
Schenectady, NY 12309

Professor Robert W. Clayton  
Seismological Laboratory  
Division of Geological and Planetary  
Sciences  
California Institute of Technology  
Pasadena, CA 91125

Dr. Vernon F. Cormier  
Earth Resources Laboratory  
Department of Earth, Atmospheric and  
Planetary Sciences  
Massachusetts Institute of Technology  
42 Carleton Street  
Cambridge, MA 02142

Professor Anton M. Dainty  
Earth Resources Laboratory  
Department of Earth, Atmospheric and  
Planetary Sciences  
Massachusetts Institute of Technology  
42 Carleton Street  
Cambridge, MA 02142

Dr. Zoltan A. Der  
Teledyne Geotech  
314 Montgomery Street  
Alexandria, VA 22314

Prof. Adam Dzierwonski  
Hoffman Laboratory  
Harvard University  
20 Oxford St.  
Cambridge, MA 02138

Professor John Ferguson  
Center for Lithospheric Studies  
The University of Texas at Dallas  
P.O. Box 830688  
Richardson, TX 75083-0688

Dr. Jeffrey W. Given  
Sierra Geophysics  
11255 Kirkland Way  
Kirkland, WA 98033

Prof. Roy Greenfield  
Geosciences Department  
403 Deike Building  
The Pennsylvania State University  
University Park, PA 16802

Professor David G. Harkrider  
Seismological Laboratory  
Division of Geological and Planetary  
Sciences  
California Institute of Technology  
Pasadena, CA 91125

Professor Donald V. Helmberger  
Seismological Laboratory  
Division of Geological and Planetary  
Sciences  
California Institute of Technology  
Pasadena, CA 91125

Professor Eugene Herrin  
Institute for the Study of Earth & Man  
Geophysical Laboratory  
Southern Methodist University  
Dallas, TX 75275

Professor Robert B. Herrmann  
Department of Earth and Atmospheric  
Sciences  
Saint Louis University  
Saint Louis, MO 63156

Professor Lane R. Johnson  
Seismographic Station  
University of California  
Berkeley, CA 94720

Professor Thomas H. Jordan  
Department of Earth, Atmospheric and  
Planetary Sciences  
Massachusetts Institute of Technology  
Cambridge, MA 02139

Dr. Alan Kafka  
Department of Geology & Geophysics  
Boston College  
Chestnut Hill, MA 02167

Professor Charles A. Langston  
Geosciences Department  
403 Deike Building  
The Pennsylvania State University  
University Park, PA 16802

Professor Thorne Lay  
Department of Geological Sciences  
1006 C.C. Little Building  
University of Michigan  
Ann Arbor, MI 48109-1063

Dr. George R. Mellman  
Sierra Geophysics  
11255 Kirkland Way  
Kirkland, WA 98033

Professor Brian J. Mitchell  
Department of Earth and Atmospheric  
Sciences  
Saint Louis University  
Saint Louis, MO 63156

Professor Thomas V. McEvilly  
Seismographic Station  
University of California  
Berkeley, CA 94720

Dr. Keith L. McLaughlin  
Teledyne Geotech  
314 Montgomery Street  
Alexandria, VA 22314

Professor Otto W. Nuttli  
Department of Earth and Atmospheric  
Sciences  
Saint Louis University  
Saint Louis, MO 63156

Professor Paul G. Richards  
Lamont-Doherty Geological Observatory  
of Columbia University  
Palisades, NY 10964

Dr. Norton Rimer  
S-Cubed  
A Division of Maxwell Laboratory  
P.O. 1620  
La Jolla, CA 92038-1620

Professor Larry J. Ruff  
Department of Geological Sciences  
1006 C.C. Little Building  
University of Michigan  
Ann Arbor, MI 48109-1063

Professor Charles G. Sammis  
Center for Earth Sciences  
University of Southern California  
University Park  
Los Angeles, CA 90089-0741

Dr. David G. Simpson  
Lamont-Doherty Geological Observatory  
of Columbia University  
Palisades, NY 10964

Dr. Jeffrey L. Stevens  
S-CUBED,  
A Division of Maxwell Laboratory  
P.O. Box 1620  
La Jolla, CA 92038-1620

Professor Brian Stump  
Institute for the Study of Earth  
and Man  
Geophysical Laboratory  
Southern Methodist University  
Dallas, TX 75275

Professor Ta-liang Teng  
Center for Earth Sciences  
University of Southern California  
University Park  
Los Angeles, CA 90089-0741

Dr. R. B. Tittmann  
Rockwell International Science Center  
1049 Camino Dos Rios  
P.O. Box 1085  
Thousand Oaks, CA 91360

Professor M. Nafi Toksoz  
Earth Resources Laboratory  
Department of Earth, Atmospheric and  
Planetary Sciences  
Massachusetts Institute of Technology  
42 Carleton Street  
Cambridge, MA 02142

Professor Terry C. Wallace  
Department of Geosciences  
Building #11  
University of Arizona  
Tucson, AZ 85721

Prof. John H. Woodhouse  
Hoffman Laboratory  
Harvard University  
20 Oxford St.  
Cambridge, MA 02138

Dr. G. Blake  
US Dept of Energy/DP 331  
Forrestal Building  
1000 Independence Ave.  
Washington, D.C. 20585

Dr. Michel Bouchon  
Universite Scientifique et  
Medicale de Grenoble  
Laboratoire de Geophysique  
Interne et Tectonophysique  
I.R.I.G.M.-B.P. 68  
38402 St. Martin D'Herès  
Cedex FRANCE

Dr. Hilmar Bungum  
NTNF/NORSAR  
P.O. Box 51  
Norwegian Council of Science,  
Industry and Research, NORSAR  
N-2007 Kjeller, NORWAY

Dr. Alan Douglas  
Ministry of Defense  
Blacknest, Brimpton, Reading RG7-4RS  
UNITED KINGDOM

Professor Peter Harjes  
Institute for Geophysik  
Rhur University  
Bochum  
P.O. Box 102148  
4630 Bochum 1  
FEDERAL REPUBLIC OF GERMANY

Dr. James Hannon  
Lawrence Livermore National Laboratory  
P.O. Box 808  
Livermore, CA 94550

Dr. E. Husebye  
NTNF/NORSAR  
P.O. Box 51  
N-2007 Kjeller, NORWAY

Dr. Arthur Lerner-Lam  
Lamont-Doherty Geological Observatory  
of Columbia University  
Palisades, NY 10964

Mr. Peter Marshall  
Procurement Executive  
Ministry of Defense  
Blacknest, Brimpton, Reading RG7-4RS  
UNITED KINGDOM

Dr. B. Massinon  
Societe Radiomana  
27, Rue Claude Bernard  
75005, Paris, FRANCE

Dr. Pierre Mechler  
Societe Radiomana  
27, Rue Claude Bernard  
75005, Paris, FRANCE

Mr. Jack Murphy  
S-CUBED  
Reston Geophysics Office  
11800 Sunrise Valley Drive  
Suite 1212  
Reston, VA 22091

Dr. Svein Mykkeltveit  
NTNF/NORSAR  
P.O. Box 51  
N-2007 Kjeller, NORWAY

Dr. Carl Newton  
Los Alamos National Laboratory  
P.O. Box 1663  
Mail Stop C 335, Group ESS3  
Los Alamos, NM 87545

Dr. Peter Basham  
Earth Physics Branch  
Department of Energy and Mines  
1 Observatory Crescent  
Ottawa, Ontario  
CANADA K1A 0Y3

Professor J. A. Orcutt  
Geological Sciences Division  
Univ. of California at San Diego  
La Jolla, CA 92093

Dr. Frank F. Pilotte  
Director of Geophysics  
Headquarters Air Force Technical  
Applications Center  
Patrick AFB, Florida 32925-6001

Professor Keith Priestley  
University of Nevada  
Mackay School of Mines  
Reno, Nevada 89557

Mr. Jack Raclin  
USGS - Geology, Rm 3C136  
Mail Stop 928 National Center  
Reston, VA 22092

Dr. Frode Ringdal  
NTNF/NORSAR  
P.O. Box 51  
N-2007 Kjeller, NORWAY

Dr. George H. Rothe  
Chief, Research Division  
Geophysics Directorate  
Headquarters Air Force Technical  
Applications Center  
Patrick AFB, Florida 32925-6001

Dr. Alan S. Ryall, Jr.  
Center for Seismic Studies  
1300 North 17th Street  
Suite 1450  
Arlington, VA 22209-2308

Dr. Lawrence Turnbull  
OSWR/NED  
Central Intelligence Agency  
CIA, Room 5G48  
Washington, DC 20505

Professor Steven Grand  
Department of Geology  
245 Natural History Bldg  
1301 West Green Street  
Urbana, IL 61801



DARPA/PM  
1400 Wilson Boulevard  
Arlington, VA 22209

Defense Technical Information Center  
Cameron Station  
Alexandria, VA 22314 (12 copies)

Defense Intelligence Agency  
Directorate for Scientific and  
Technical Intelligence  
Washington, D.C. 20301

Defense Nuclear Agency  
Shock Physics Directorate/SS  
Washington, D.C. 20305

Defense Nuclear Agency/SPSS  
ATTN: Dr. Michael Shore  
6801 Telegraph Road  
Alexandria, VA 22310

AFOSR/NPG  
ATTN: Director  
Bldg 410, Room C222  
Bolling AFB, Washington, D.C. 20332

AFTAC/CA (STINFO)  
Patrick AFB, FL 32925-6001

AFWL/NTESC  
Kirtland AFB, NM 87171

U.S. Arms Control & Disarmament Agency  
ATTN: Mrs. M. Hoinkes  
Div. of Multilateral Affairs, Rm 5499  
Washington, D.C. 20451

U.S. Geological Survey  
ATTN: Dr. T. Hanks  
National Earthquake Research Center  
345 Middlefield Road  
Menlo Park, CA 94025

SRI International  
333 Ravensworth Avenue  
Menlo Park, CA 94025

Center for Seismic Studies  
ATTN: Dr. C. Romney  
1300 North 17th Street  
Suite 1450  
Arlington, VA 22209 (3 copies)

Dr. Robert Blandford  
DARPA/GSD  
1400 Wilson Boulevard  
Arlington, VA 22209-2308

Ms. Ann Kerr  
DARPA/GSD  
1400 Wilson Boulevard  
Arlington, VA 22209-2308

Dr. Ralph Alewine III  
DARPA/GSD  
1400 Wilson Boulevard  
Arlington, VA 22209-2308

Mr. Edward Giller  
Pacific Sierra Research Corp.  
1401 Wilson Boulevard  
Arlington, VA 22209

Science Horizons, Inc.  
Attn: Dr. Bernard Minster  
Dr. Theodore Cherry  
710 Encinitas Blvd., Suite 101  
Encinitas, CA 92024 (2 copies)

Dr. Jack Evernden  
USGS - Earthquake Studies  
345 Middlefield Road  
Menlo Park, CA 94025

Dr. Lawrence Braille  
Department of Geosciences  
Purdue University  
West Lafayette, IN 47907

Dr. G.A. Bollinger  
Department of Geological Sciences  
Virginia Polytechnical Institute  
21044 Derring Hall  
Blacksburg, VA 24061

Dr. L. Sykes  
Lamont Doherty Geological Observatory  
Columbia University  
Palisades, NY 10964

Dr. S.W. Smith  
Geophysics Program  
University of Washington  
Seattle, WA 98195

Dr. L. Timothy Long  
School of Geophysical Sciences  
Georgia Institute of Technology  
Atlanta, GA 30332

Dr. N. Biswas  
Geophysical Institute  
University of Alaska  
Fairbanks, AK 99701

Dr. Freeman Gilbert  
Institute of Geophysics &  
Planetary Physics  
Univ. of California at San Diego  
P.O. Box 109  
La Jolla, CA 92037

Dr. Pradeep Talwani  
Department of Geological Sciences  
University of South Carolina  
Columbia, SC 29208

University of Hawaii  
Institute of Geophysics  
Attn: Dr. Daniel Walker  
Honolulu, HI 96822

Dr. Donald Forsyth  
Department of Geological Sciences  
Brown University  
Providence, RI 02912

Dr. Jack Oliver  
Department of Geology  
Cornell University  
Ithaca, NY 14850

Dr. Muawia Barazangi  
Geological Sciences  
Cornell University  
Ithaca, NY 14853

Rondout Associates  
Attn: Dr. George Sutton  
Dr. Jerry Carter  
Dr. Paul Pomeroy  
P.O. Box 224  
Stone Ridge, NY 12484 (3 copies)

Dr. Bob Smith  
Department of Geophysics  
University of Utah  
1400 East 2nd South  
Salt Lake City, UT 84112

Dr. Anthony Gangi  
Texas A&M University  
Department of Geophysics  
College Station, TX 77843

Dr. Gregory B. Young  
ENSOO, Inc.  
5400 Port Royal Road  
Springfield, CA 22151

Dr. Ben Menaheim  
Weizman Institute of Science  
Rehovot, ISRAEL 951729

Weidlinger Associates  
Attn: Dr. Gregory Wojcik  
620 Hansen Way, Suite 100  
Palo Alto, CA 94304

Dr. Leon Knopoff  
University of California  
Institute of Geophysics & Planetary  
Physics  
Los Angeles, CA 90024

Dr. Kenneth H. Olsen  
Los Alamos Scientific Laboratory  
Post Office Box 1663  
Los Alamos, NM 87545

Prof. Jon F. Claerbout  
Prof. Amos Nur  
Dept. of Geophysics  
Stanford University  
Stanford, CA 94305 (2 copies)

Dr. Robert Burridge  
Schlumberger-Doll Research Ctr.  
Old Quarry Road  
Ridgefield, CT 06877

Dr. Eduard Berg  
Institute of Geophysics  
University of Hawaii  
Honolulu, HI 96822

Dr. Robert Phinney  
Dr. F.A. Dahlen  
Dept. of Geological & Geophysical Sci.  
Princeton University  
Princeton, NJ 08540 (2 copies)

Dr. Kin-Yip Chun  
Geophysics Division  
Physics Department  
University of Toronto  
Ontario, CANADA M5S 1A7

New England Research, Inc.  
Attn: Dr. Randolph Martin III  
P.O. Box 857  
Norwich, VT 05055

Sandia National Laboratory  
Attn: Dr. H.B. Durham  
Albuquerque, NM 87185

Dr. Gary McCartor  
Mission Research Corp.  
735 State Street  
P. O. Drawer 719  
Santa Barbara, CA 93102

Dr. W. H. K. Lee  
USGS  
Office of Earthquakes, Volcanoes,  
& Engineering  
Branch of Seismology  
345 Middlefield Rd  
Menlo Park, CA 94025

AFGL/XO  
Hanscom AFB, MA 01731-5000

AFGL/LW  
Hanscom AFB, MA 01731-5000

AFGL/SULL  
Research Library  
Hanscom AFB, MA 01731-5000 (2 copies)

Secretary of the Air Force (SAFRD)  
Washington, DC 20330

Office of the Secretary Defense  
DDR & E  
Washington, DC 20330

HQ DNA  
Attn: Technical Library  
Washington, DC 20305

Director, Technical Information  
DARPA  
1400 Wilson Blvd.  
Arlington, VA 22209

Los Alamos Scientific Laboratory  
Attn: Report Library  
Post Office Box 1663  
Los Alamos, NM 87544

Dr. Thomas Weaver  
Los Alamos Scientific Laboratory  
Los Alamos, NM 87544

Dr. Al Florence  
SRI International  
333 Ravenswood Avenue  
Menlo Park, CA 94025-3493

END

9-87

Dtic